Bachelor's Degree Final Project

Aerospace Vehicles Engineering

COMPUTATIONAL RESOLUTION OF THE NAVIER-STOKES EQUATIONS FOR LAMINAR AND TURBULENT FLOWS. IMPLEMENTATION OF THE SPALART-ALLMARAS TURBULENCE MODEL.

HEAT AND MASS TRANSFER CENTER (CTTC)

Report

Friday 3rd July, 2020

Author: Sergio Gutiérrez Sánchez

Director: Assensi Oliva Llena

Co-director: Carles David Pérez Segarra

Call: 2019/2020 QP

UNIVERSITAT POLITÈCNICA DE CATALUNYA
BARCELONATECH

Escola Superior d'Enginyeries Industrial,
Aeroespacial i Audiovisual de Terrassa

Acknowledgements

Me gustaría agradecer a diversas personas y organismos el apoyo y la ayuda recibidas durante el desarollo de este proyecto y durante el tiempo de estudio del grado en ingeniería en vehículos aeroespaciales.

- Mi agradecimiento al sistema universitario catalán y español por la oportunidad de estudiar esta carrera y por la formación académica y personal recibida durante este tiempo.
- A mi familia, quienes desde que tengo uso de razón me han motivado y ayudado incondicionalmente a cumplir mi sueño de llegar a ser ingeniero aeronaútico y dedicarme profesionalmente a ello sin importar cualquier circunstancia.
- Mi más sincero agradecimiento también para los profesores y doctores Assensi Oliva Llena y Carlos David Pérez Segarra por darme la increíble oportunidad de entrar en el CTTC para formarme como ingeniero de CFD. Así como a todos los miembros del centro, entre ellos el doctor Francesc Xavier Trias Miquel por su inestimable ayuda.
- En especial también me gustaría agradecer a Jesús Ruano, compañero del CTTC que desde el primer día me ha ayudado en todo lo que he necesitado y sin el cuál este proyecto, desde su base, habría sido completamente imposible de desarrollar.

Abstract

The present project consists on the computational study and resolution of the Navier-Stokes equations and the physical phenomena involved.

The main objective is the development of C++ programming codes to solve flow's governing equations using numerical methods. The project comprises the fluid dynamic and thermal study and analysis of both laminar and turbulent regimes. In addition to that, in case of turbulent flow, there has been selected to implement a RANS turbulence model called Spalart-Allmaras.

The computational codes developed will be used to simulate the study cases LID Driven Cavity, LID Differentially Heated and Square Cylinder for the laminar regime and a supersonic pipe in case of the turbulent part. Additionally, the results obtained will be extensively analysed and verified using scientific publications.

Declaration of honour

I declare that,

the work in this Degree Thesis is completely my own work,

no part of this Degree Thesis is taken from other people's work without giving them credit,

all references have been clearly cited,

I'm authorised to make use of the research group related information I'm providing in this document.

I understand that an infringement of this declaration leaves me subject to the foreseen disciplinary actions by The Universitat Politècnica de Catalunya - BarcelonaTECH.

Sergio Gutiérrez Sánchez		Friday 3rd July, 2020
Student name	Signature	Date

Title of the Thesis:

Study for the computational resolution of conservation equations of mass, momentum and energy. Possible application to different aeronautical and industrial engineering problems: Case 50B

Contents

List of Figures

List of Tables

Nomenclature

Table 1: Mathematical expressions nomenclature

Symbol	Definition
$\frac{D}{Dt}$	Total/material derivative
$\frac{\partial}{\partial x}$	Partial derivative with respect to x
$\frac{\partial}{\partial t}$	Temporal derivative
$\partial\phi$	ϕ Differential
$\nabla\cdot$	Divergence
∇	Gradient
∇^2	Laplacian operator
M:N	Frobenius inner product
$\sum$	Summation
n	Normal unit vector to the surface
$\iint$ dS	Surface integral
$\iiint dV$	Volumetric integral

Table 2: Fluid mechanics nomenclature

Symbol	Definition	Units (IS)
u	Velocity vector	$[m/s]$
u	Velocity horizontal/axial component	$[m/s]$
v	Velocity vertical/radial component	$[m/s]$
w	Velocity depth/azimuthal component	$[m/s]$
μ	Dynamic viscosity	$[Pa \cdot s]$
ν	Kinematic viscosity	$[m^2/s]$
λ/K	Conduction heat transfer	$[W/K \cdot m]$
C_v	Heat capacity at constant volume	$[J/Kg \cdot K]$
C_p	Heat capacity at constant pressure	$[J/Kg \cdot K]$
ρ	Density	$[Kg/m^3]$
q	Heat flux	$[W/m[2]$
T	Temperature	$[K]$
P	Pressure	$[Pa]$
f	Volumetric force	$[N/Kg]$
τ	Viscous stress tensor	$[N/m^2]$
g	Gravity acceleration	$[m/s^2]$
h	Specific enthalphy	$[J/Kg]$
e	Specific energy	$[J/Kg]$
u	Specific internal energy	$[J/Kg]$
α	Heat diffusivity	$[m^2/s]$
β	Thermal expansion coefficient	$[K^{-1}]$
c	Speed of sound	$[m/s]$
γ	Heat capacity ratio	-
R	Ideal gas constant	$[J/Kg \cdot K]$

Table 3: Numerical methods nomenclature

Symbol	Definition
ϕ	Generic variable
ϕ^n	Generic variable at present time step
ϕ^{n-1}	Generic variable at previous time step
ϕ^{n+1}	Generic variable at next time step
$\phi_f / \phi\|_f$	Generic variable value at control's volume surface
ϕ''	Generic variable fluctuation
$\widetilde{\phi}$	Density weighted averaged Generic variable
$\widehat{\phi}$	Generic variable non-dimensional value
$\overline{\phi}$	Generic variable mean value
ϕ	Generic variable surface normal component
ϕ_P / ϕ_K	Generic variable at present control volume
$\phi_{nb(f)}$	Generic variable of neighbour control volume
ΔX	Distance between two nodes on the mesh
X_i / Y_i	Spatial coordinate of the node i
NX	Total number of nodes in X direction
NY	Total number of nodes in Y direction
SF	Stretching factor of Hyperbolic Tangent nodal distribution
Δt	Time increase between steps
$F(\phi)$	Variable ϕ contribution
δ	Convergence criteria
Ω	Total volume of the control volume
ΔS / A_f	Area of the control volume f face
φ_f	Surface normal deviation from coordinate system axis
R_K	Radial coordinate of node K
β_{Time}	Temporal integration parameter
d_{PE}	Distance between nodes P and East

Table 4: Spalart-Allmaras model nomenclature

Symbol	Definition	Units (IS)
$\widetilde{\nu}$	Turbulent kinematic viscosity	$[m/s^2]$
d	Closest distance to any solid wall	$[m]$
K_{VK}	Von-Karman constant	-
w	Vorticity	$[\Gamma/m^2]$

Chapter 1

Introduction

The present project aims to the study and resolution of both laminar and turbulent regimes, therefore, the thesis structure proposed is the following.

First, in the Introduction chapter are presented the justification, scope and specifications to give a better insight of the framework and objectives of the project.

Then, in chapter 2 is presented a brief explanation of the history of Fluid Mechanics, alongside with an extensive description of the Navier-Stokes fluid governing equations and the physical phenomena involved. Additionally, in this chapter are exposed a necessary presentation of the importance of non-dimensional analysis and a short description of what is Computational Fluid Dynamics.

In chapter 3 is presented all the work developed for the study of laminar regime flow. First, a theoretical background of the fluid characteristics and physical phenomena involved is exposed. After that, all the numerical methods and techniques applied are extensively explained. Finally the results obtained for the simulation cases are shown alongside with a deep analysis and verification of them using scientific references.

The turbulent regime study is presented in chapter 4. It comprises a theoretical background of flow's characteristics and phenomena, alongside with a profoundly explanation of RANS turbulence modelling. In addition, all the numerical methods used in this part of the project are presented too. Lastly, the results obtained in the simulations and the verification are exposed too.

In chapter 5 is presented the study of the environmental impact of the project.

Finally, in chapter 6 are presented the final conclusions of the whole project and the planned future work.

1.1 Justification

Computational Fluid Dynamics is a field of knowledge that has been growing unstoppably since several decades ago. The enormous increase in computational power has allowed researchers and engineers to develop more complex studies and to expand the areas in which CFD is useful.

Nowadays, Computational Fluid Dynamics has spread on most of the engineering industries and has become a great tool for design, development and optimisation. It allows to carry out many different type of studies for the same design and cuts down all experimentation costs. Every year there are new numerical methods and algorithms that improve the previous simulations. However, the biggest aspect to remark of Computational Fluid Dynamics may be its unlimited possibilities in the future.

In this project, CFD is used in the study of both laminar and turbulent regimes. In case of the first one, it is of vital importance to have a good understanding in the numerical simulation of these kind of flows. They are the basis in which more complex CFD studies support. It is essential a good comprehension and experience in these type of simulations to be able to get into the turbulent regime area.

Nevertheless, the main justification of this project comes from the turbulent regime part of it. Most of the industrial and scientific applications of CFD are based on turbulent flows. Therefore, a great background in the simulation of these provides with enormous possibilities.

In this project is presented the study and simulation of a turbulent supersonic pipe. This helps in the understanding of the physical and numerical phenomena involved and provides a great basis for the future development of the programming codes. The long-term main objective is the development of a computational tool to simulate, analyse and optimise rocket nozzles. This would ease enormously the design and development of them. However, due to the extreme difficult of this aim, it is impossible to present that in this report. Nevertheless, the turbulent regime codes already developed are a great basis to continue working for this objective.

Another important aspect of the project is the development of C++ simulation codes instead of using already programmed commercial simulation software. It is true that, the use of this kind of tools reduce dramatically the difficulty of the whole project. However, they limit severely the possibilities in mid and long term since they are only simulation tools. On the other hand, in C++ it is possible to program and do everything the developer may want to. This allows, for instance of having a tool not only able to simulate turbulent flows in rocket nozzles, but also one capable of analyse and optimise them.

In conclusion, although the work presented in this project comprises a global view of fluid mechanics with the study of laminar and turbulent regime, it provides with a great basis for further development of computational codes for simulating, analysing and optimising rocket nozzles with endless possibilities.

1.2 Scope

The scope of this project is divided in two main sections.

Laminar regime.

- Study of the Navier-Stokes equations and the involved physical phenomena for the simulation of laminar flows' behaviour.
- Deduction and application of several hypothesis for the simulation of laminar incompressible regime flows.

- Numerical spatial discretization of the proposed cases geometries based on Finite Volume Method theoretical background and the hypothesis previously assumed.
- Resolution of the Navier-Stokes adapted equations with Fractional Step Method and other numerical techniques.
- Simulation of the proposed laminar regime cases LID Driven Cavity, LID Differentially Heated and Square Cylinder.
- Verification of the obtained results from the previous simulations based on trustworthy sources.

Turbulent regime.

- Study of the physical theoretical phenomena involved in turbulent regime flows.
- Study of the basis of turbulence modelling. Specially emphasising in RANS (Reynolds Averaged Navier-Stokes equations) turbulence modelling.
- Study of the theoretical basis of the Spalart-Allmaras RANS turbulence model.
- Application of several hypothesis for the simulation of turbulent compressible supersonic flows.
- Numerical spatial discretization of the proposed geometries based on Finite Volume Method.
- Resolution of the adapted Navier-Stokes equations for the simulation of compressible supersonic flows.
- Numerical implementation of the Spalart-Allmaras turbulence model.
- Simulation of the proposed turbulent regime study case.
- Verification of the obtained results from the previous simulations with scientific publications.

1.3 Specifications

The technical specifications for the development of this project are the following.

Programming specifications.

- No commercial simulation software can be used in any of the study cases.
- All the codes of the project must be developed entirely by the student. No other non-commercial code can be used, except for a matrix inverter C++ library.
- All the codes must be programmed in C++ language and they should be able to work in a Linux Ubuntu environment.
- The programming developed must be object-oriented.
- The codes developed for laminar and turbulent regime must be generic enough to at least being able to simulate all the different study cases proposed for each flow regime respectively.

Simulation specifications.

- Study cases geometries and equations resolution must be based on Finite Volume Method (FVM).
- Assumed simulation hypothesis of each flow regime must be presented at the beginning of their respective sections.
- For the turbulent regime study there will be necessary the implementation of a RANS turbulence model apart from the resolution of the Navier-Stokes equations.

Post-processing specifications.

- Paraview, Gnuplot and Inkscape free software can be used for post-processing and results visualization tasks.
- Each study case presented must be verified using trustworthy scientific publications.

Chapter 2

What is Fluid Mechanics

2.1 Introduction and history of the field.

Fluid mechanics, as the name already indicates, consists on the application of the laws of force and motion to fluids, liquids and plasma. There are two main branches inside of it.

First of them, the Fluid statics or Hydrostatics, which is based on the study of fluids at rest. The other one, in which this project focuses on, is the Fluid dynamics, related to fluid's motion.

Along the history, specially in 20th century, Fluid mechanics branch has grown in importance exponentially. Nowadays there are millions of modern engineering devices that depend partially or completely on it. Great inventions wouldn't exist without all the knowledge behind, all the discovered phenomena, all the experimentation, etc...

This field of knowledge has been studied from several millennia ago. In the ancient Greek, Archimedes (285-212 BC), formulated the laws of buoyancy, known as Archimedes Principle.

Leonardo Da Vinci (1452-1519) in the 15th century was able to derive the equation of conservation of mass in one-dimensional steady flow. Apart from that he wrote many notes about descriptions of waves, pumps and jets.

Figure 2.1: Da Vinci's sketch of free-surface turbulence behind obstacle. Extracted from [1]

Two centuries later, Isaac Newton (1642-1727) postulated the laws of motion and viscosity of linear fluids, which are now known as Newtonian Fluids.

Other important contributions to the field are the ones made by Daniel Bernoulli (1700-1782) in the relationship between fluid's pressure and speed based on energy conservation. In addition to remarkable discoveries made by Jean le Rond d'Alembert (1717-1783) and Leonhard Euler (1707-1783) in this century.

Nevertheless, it wasn't until 19th century that probably the most important contribution to fluid

mechanics was made. French engineer Claude-Louis Navier (1785-1836) and Irish mathematician George Gabriel Stokes (1819-1903) succeeded in creating governing equations for real fluid motion. This was an outstanding milestone due to the fact that it was the first time experimental and theoretical analysis on the field matched.

These equations are in which today's fluid dynamics studies are based on. However, most theoretical solutions for them remain undiscovered. They often include turbulence, which is still one of the greatest problems in physics and engineering nowadays.

In the early 20th century, Ludwig Prandtl (1875-1953) came up with the idea of boundary layer. Other contributions to the field were made by Theodore Von Kármán (1881–1963) and Paul Richard Blasius (1883–1970).

In this century, due to the difficult challenges that, specially aerodynamics represented, and the creation of computers, the fluid mechanics shifted from an analytical point of view to a numerical one. This new knowledge branch was called *Computational Fluid Dynamics*, which will be explained in a more detailed way in section 2.4.

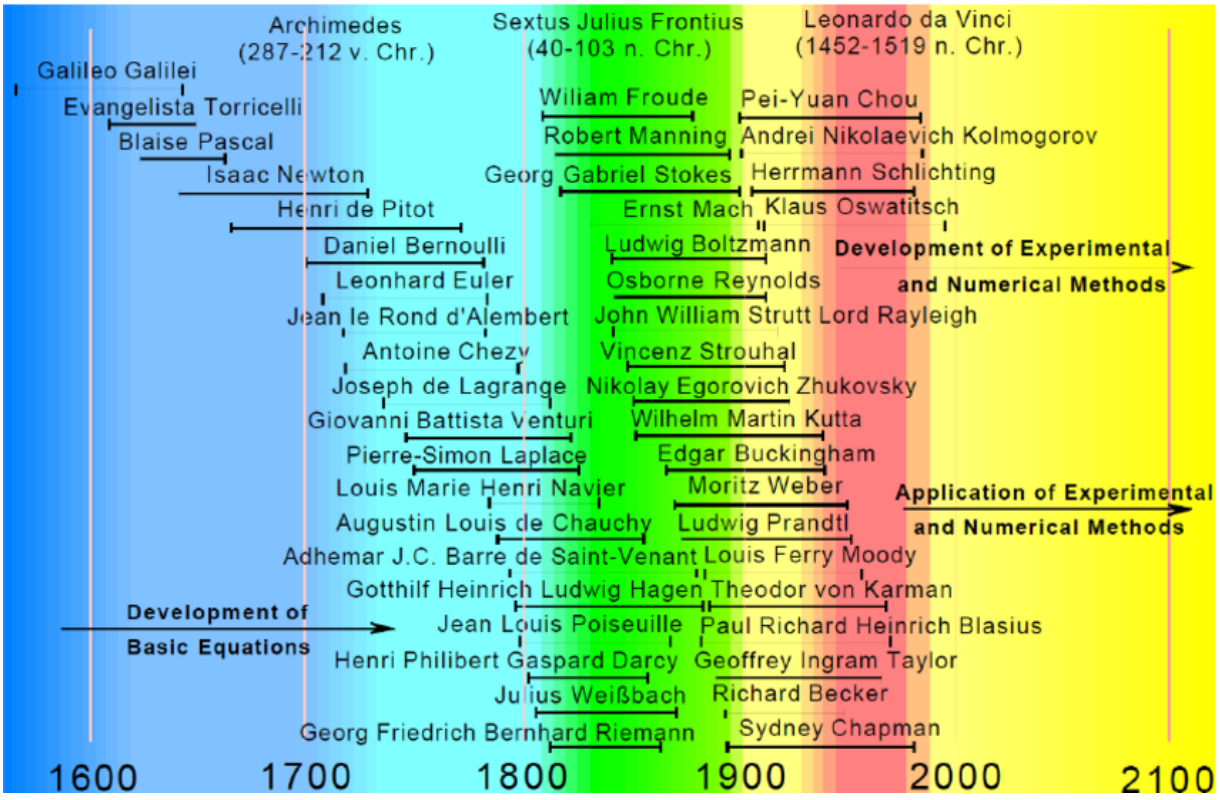

Figure 2.2: Historical timeline of fluid mechanics. Extracted from [1]

2.2 Governing equations of fluid mechanics.

As it has been exposed, the fluid mechanics theoretical basis rely on the equations presented by Claude-Louis Navier and George Gabriel Stokes. There are two types of approach for them.

- **Lagrangian description.**

  This is an approach based on the follow-up of the fluid particle and its properties evolution over time.

  In this case, a fluid particle, the tiniest, indivisible, element of fluid is identified by its initial position at a time t_o. Then, Navier-Stokes equations are used to determine its position inside the study domain at a certain time. Therefore, knowing its location, allows to calculate other associated characteristics such as velocity, pressure or density.

- **Eulerian description.**

  In contrast to the Lagrangian way, Eulerian approach is based on the monitoring of a fixed point in the domain, instead a moving element.

  Initially, it is specified the fluid properties (velocity, density, pressure...) in this fixed point at a chosen time. Then, solving Navier-Stokes equations gives the evolution of mentioned physical characteristics over time.

  This is the most common approach used in fluid mechanics in scientific and industrial studies. Mainly because, Eulerian way is much more cheaper than Lagrangian in computational costs.

For further information about the physical and mathematical differences between both approaches go to [13].

In this project, Eulerian approach is used in all studies and simulation carried out.

All the following equations are presented in its differential form and from an Eulerian approach.

2.2.1 The material derivative

One important aspect to understand properly the Navier-Stokes conservation equations is the concept of Material derivative.

It is defined as follows.

$$\frac{D\phi}{Dt} = \frac{\partial \phi}{\partial t} + \nabla \cdot (\phi \mathbf{u}) \tag{2.1}$$

Expanding the last term of the equation (2.1), it is possible to obtain the following expression.

$$\frac{D\phi}{Dt} = \frac{\partial \phi}{\partial t} + u\frac{\partial \phi}{\partial x} + v\frac{\partial \phi}{\partial y} + w\frac{\partial \phi}{\partial z} \tag{2.2}$$

And, finally, if the velocity variables (u, v and w) also vary with x, y, or z (as in most cases), it can be obtained the next equation.

$$\frac{D\phi}{Dt} = \frac{\partial \phi}{\partial t} + \frac{\partial \phi u}{\partial x} + \frac{\partial \phi v}{\partial y} + \frac{\partial \phi w}{\partial z} \tag{2.3}$$

2.2.2 Convection - Diffusion equation.

The convection - diffusion equation describes the phenomena in which physical properties of a material or fluid are transferred through a system due to convection (advection) and diffusion.

The convection process, also known as advection consists on the transport of physical properties such as temperature or density by the velocity of the particles.

On the other hand, diffusion phenomena comprises the transport of physical properties due to no-null gradients of these ones.

All Navier-Stokes equations can be written based on Convection - Diffusion equation.

$$\frac{D\rho\phi}{Dt} = \nabla \cdot (\Gamma_\phi \nabla \phi) + Source \tag{2.4}$$

$$\frac{\partial \rho\phi}{\partial t} + \frac{\partial \rho\phi u}{\partial x} + \frac{\partial \rho\phi v}{\partial y} + \frac{\partial \rho\phi w}{\partial z} = \nabla \cdot (\Gamma_\phi \nabla \phi) + Source \tag{2.5}$$

Table 2.1: Generic Convection - Diffusion equation parameters for Navier - Stokes equations.

Equation	ϕ	Γ_ϕ	**Source**
Mass Conservation	1	0	0
Momentum Conservation	**u**	μ	-∇P + ρf
Energy Conservation	T	$\frac{\lambda}{C_v}$	-$\frac{DP}{Dt}$ + Φ

As it can be seen, all Navier - Stokes equations are based on the convection or advection and diffusion phenomena, plus in each case its respective source.

2.2.3 Mass conservation equation.

First of them is the Mass conservation equation, also known as the Continuity equation. It relates the density and velocity of any material particle during motion.

$$\frac{D\rho}{Dt} = 0 \tag{2.6}$$

$$\frac{\partial \rho}{\partial t} + \nabla \cdot (\rho \mathbf{u}) = 0 \tag{2.7}$$

In a rough way, it can be described as the following statement.

"The rate of increase of mass in a control volume must equal the rate at which mass is flowing into the volume through its bounding surface per unit of time"

- **Density change rate ($\frac{\partial \rho}{\partial t}$).**

  It represents the rate at which the density is varying inside the control volume and so its mass.

- **Flow into the volume ($\nabla \cdot (\rho \mathbf{u})$).**

  It represents the rate at which the mass in flowing in or out the volume through its bounding surfaces. It is also known as the convective term of the Mass conservation equation.

This can be expressed in the Cartesian coordinate system as following.

$$\frac{\partial \rho}{\partial t} + \left(\frac{\partial \rho u}{\partial x} + \frac{\partial \rho v}{\partial y} + \frac{\partial \rho w}{\partial z} \right) = 0 \tag{2.8}$$

2.2.4 Momentum conservation equation.

This equation makes reference to Newton's second law (the rate of change of any body's momentum is proportional to the force applied).

The Momentum conservation equation it can be expressed in the following way.

The rate of change of momentum inside a control volume must be equal to the rate at which momentum is flowing through its bounding surfaces plus the forces applied on it.

$$\frac{D\rho \mathbf{u}}{Dt} = -\nabla p + \nabla \cdot \tau + \rho f \tag{2.9}$$

$$\frac{\partial \rho \mathbf{u}}{\partial t} + \nabla \cdot (\rho \mathbf{u}\mathbf{u}) = -\nabla p + \nabla \cdot \tau + \rho f \tag{2.10}$$

- **Momentum change rate ($\frac{\partial \rho \mathbf{u}}{\partial t}$).**

  This term represents the total rate of change of momentum $(\rho \mathbf{u})$ inside a control volume.

- **Flow into the volume ($\nabla \cdot (\rho \mathbf{u}\mathbf{u})$).**

  It represents the rate at which momentum is flowing through the bounding surfaces of the control volume. It is also known as the convective term of the Momentum Conservation equation.

- **Pressure gradient ($-\nabla p$).**

  It is the force applied to the control volume surfaces due to a pressure difference between its limits. As it can be seen, it is negative. This is due to the fact that the resulting force is always opposed to it. An increasing gradient in the positive direction results in a negative net force.

- **Viscous stress ($\nabla \cdot \tau$).**

  This term represents the force applied to control volume's bounding surfaces due to the viscosity of the fluid. This force is generated by the velocities gradients. The higher it is, the higher the shear stress produced and so the forces.

  It depends on the physical properties of the fluid. The behaviour may vary significantly from one type of fluid to another. This is the case for instance of viscous and non-viscous fluids.

- **Volumetric force (ρf).**

  This term represents the force applied in the control volume due to a determined gravitational acceleration or any other non-interaction forces (fundamental forces). In this project, only gravity will be set in this term.

The Momentum Conservation equation can be be expressed in the Cartesian coordinate system as following.

X axis.

$$\frac{\partial \rho u}{\partial t} + \nabla \cdot (\rho u u) = -\frac{\partial p}{\partial x} + \nabla \cdot \tau|_x + \rho g_x \tag{2.11}$$

Y axis.

$$\frac{\partial \rho v}{\partial t} + \nabla \cdot (\rho v v) = -\frac{\partial p}{\partial y} + \nabla \cdot \tau|_y + \rho g_y \tag{2.12}$$

Z axis.

$$\frac{\partial \rho w}{\partial t} + \nabla \cdot (\rho w w) = -\frac{\partial p}{\partial z} + \nabla \cdot \tau|_z + \rho g_z \tag{2.13}$$

2.2.5 Energy conservation equation.

The Energy conservation equation is based on the thermodynamics's law which states that the rate of change of energy in a fluid particle must be equal to the energy received by heat and work transfers.

There are many ways to express this equation depending on the energy variable selected. Specific energy or kinetic energy are other variables this equation can be expressed as a function of. In this case it is presented using the internal specific enthalpy.

$$\frac{D\rho h}{Dt} = -\frac{DP}{Dt} - \nabla q + \tau : \nabla \mathbf{u} \tag{2.14}$$

$$\frac{\partial \rho h}{\partial t} + \nabla \cdot (\rho h \mathbf{u}) = -\frac{DP}{Dt} - \nabla q + \tau : \nabla \mathbf{u} \tag{2.15}$$

The energy rate of change of a control volume must be equal to the energy flow through its bounding surfaces plus the heat transferred and the work applied to the control volume.

To introduce the concept of enthalpy, it is necessary first to present what is the specific energy.

The amount of energy per unit of mass can be expressed as follows.

$$e = u + \frac{1}{2} \cdot \mathbf{u}^2 + g \tag{2.16}$$

Being u the internal energy per mass of fluid, $(\frac{1}{2} \cdot \mathbf{u}^2)$ the kinetic energy per mass of fluid and g the gravitational potential energy per mass of fluid.

Then, the specific energy and enthalpy can be related in the following way.

$$h = e + \frac{P}{\rho} \tag{2.17}$$

- **Energy change rate ($\frac{\partial \rho h}{\partial t}$).**

  It represents the rate of change of energy (ρh) of a control volume.

- **Energy flow into the volume ($\nabla \cdot (\rho h \mathbf{u})$).**

  This term comprises the energy flowing through the bounding surfaces of the control volume in and out of it.

- **Pressure term ($-\frac{DP}{Dt}$).**

  It represents the rate of energy transfered due to variations of pressure. As it has been exposed before, the total energy of a fluid depends on its pressure (equation (2.17)). Therefore, a change on this variable produces a variation of it.

  Following the procedure shown in section 2.2.1, this term can be expanded as follows.

$$\frac{DP}{Dt} = \frac{\partial P}{\partial t} + \frac{\partial Pu}{\partial x} + \frac{\partial Pv}{\partial y} + \frac{\partial Pw}{\partial z} \tag{2.18}$$

- **Conduction heat transfer (∇q).**

  This term represents the heat transfer inside the fluid due to temperature gradients. It is based on Fourier's law, which states as following.

$$q_i = -K\frac{\partial T}{\partial x_i} \tag{2.19}$$

  It depends on fluid's thermal conductivity, K, and is also related to several heat transfer phenomena that will be explained in a more detailed way later in this thesis.

- **Energy viscous dissipation ($\tau : \nabla \mathbf{u}$).**

  It represents the energy transfer due to fluid's work against viscous forces. As it has been shown in section 2.2.4, velocity gradients generate viscous stress in the fluid. These create an energy transfer due to dissipation.

  The mathematical development of the term can be found in appendix G in Annex document of this project.

Finally, it is presented the Energy Conservation equation expanded.

$$\frac{\partial \rho h}{\partial t} + \nabla \cdot (\rho h \mathbf{u}) = \frac{\partial P}{\partial t} + \frac{\partial Pu}{\partial t} + \frac{\partial Pv}{\partial t} + \frac{\partial Pw}{\partial t} - \nabla q + \tau : \nabla \mathbf{u} \tag{2.20}$$

For further information about the Fluid Mechanics governing equations go to [14], [15] and [16].

2.3 Non-dimensionalization.

In all physical phenomena there are variables and parameters involved that govern its behaviour and its characteristics. However, it isn't necessary to know all of them to describe or to quantify this phenomena. For instance, in order to determine the flow around a cylinder it doesn't matter if the velocity is 1 m/s or 10 m/s.

What really matters is the relationship between the physical properties involved. This is called non-dimensionalization.

It consists on removing the physical dimensions from an equation or from a properties relationship. Imagine having a problem in which u_x represents the horizontal velocity of the flow. This magnitude dimensions is m/s, so, fixing a reference velocity U_{ref}, there can be obtained the dimensionless variable.

$$U_{Non-Dim} = \frac{u_x}{U_{ref}}$$

This is a common practice when the problem involves physical phenomena and partial differential equations. In fact, non-dimensionalization isn't at all necessary to solve or to simulate a problem. However, it gives a great advantage in terms of experimentation and analysis.

This is the case, for instance, of the simulation of flow inside a pipe. Imagine fixing its non-dimensional variables, for example, a dimensionless diameter. This allows to know the behaviour of the fluid for the fixed dimensional variables (diameter in this situation), but also for any other dimensional diameter with the same dimensionless value.

The physical or mathematical results are the same if these non-dimensional variables are equal in both cases.

Throughout fluid mechanics history, there have been discovered many physical phenomena involved in the behaviour of the fluids. In order to take these into account exploiting the potential of non-dimensional analysis scientist created different dimensionless numbers to describe and relate them.

- **Reynolds number (Re).**

  Perhaps, the most famous non-dimensional number in fluid mechanics. Established by Osborne Reynolds (1842 - 1912) in 1883 while studying the flow inside pipes with different diameters.

  It represents the ratio between the inertial forces to viscous forces. As it is explained after in this thesis, this number is used to differ the flow regime between laminar and turbulent.

$$Re = \frac{\rho U L_{ref}}{\mu} = \frac{U L_{ref}}{\nu} \tag{2.21}$$

- **Prandtl number (Pr).**

  Created by the German engineer Ludwig Prandtl (1875 - 1953). It represents the ratio between momentum diffusivity to thermal diffusivity.

$$Pr = \frac{\nu}{\alpha} = \frac{C_p \mu}{K} \tag{2.22}$$

- **Nusselt number (Nu).**

  Established by Wilhelm Nusselt (1882 - 1957). It is the relationship between the convective and conductive heat transfer at a boundary layer in a fluid.

$$Nu_x = \frac{\partial (T_w - T_x)}{\partial y} \cdot \frac{L_{ref}}{T_w - T_\infty} \tag{2.23}$$

- **Rayleigh number (Ra).**

  Set by the British scientist Lord Rayleigh (1842 - 1919). It is highly related to the Nusselt number as it represents the ratio between the convection and conduction heat transfer in the fluid.

  - **Natural convection.**

    Natural convection is characterised by a low heat transfer coefficient. This is because of the low fluid motion velocities, since its move occurs by natural means such as buoyancy [17].

  - **Forced convection.**

    In this case the heat transfer increases due to the rise in the velocities. The fluids are forced to move by ceiling fans, pumps, etc... [18].

  The frontier between natural and forced convection is determined by the Rayleigh number although this limit may differ from one problem to another. The bigger Rayleigh, the higher heat transfer.

$$Ra = \frac{\rho g \beta \Delta T L^3}{\alpha \mu} \tag{2.24}$$

- **Strouhal number (St).**

  Named after Vincent Strouhal (1850 - 1922). It is a dimensionless number that describes the oscillating flow mechanisms. In fluid dynamics it is related to vortex shedding (oscillating flow that generated vortexes when it goes through an object).

$$St = \frac{f \cdot L_{ref}}{U_{ref}} \tag{2.25}$$

- **Mach number (Ma).**

  This non-dimensional number is the rate between the velocity of the fluid and the speed of sound. It is commonly used in fluid mechanics, especially in aerodynamics. For instance, it is widely accepted the use of Mach number to determine if air flows can be considered compressible or not (above 0.3 is compressible).

$$Ma = \frac{U}{c} \tag{2.26}$$

2.4 Computational Fluid Dynamics.

Computational fluid dynamics (CFD) is the application of numerical methods and algorithms to solve the fluid flow equations. This allows to predict the behaviour of any fluid based on the resolution of the Navier-Stokes equations. These mathematical expressions govern the way a fluid flows under any boundary conditions, from water inside a pipe, to planetary atmospheres.

Since no one has ever provided a generic, analytic solution for the Navier - Stokes equations, scientists had to look for alternative ways or determined hypothesis to get reasonable results. This is the case for instance of inviscid fluid studies in the early 20th century.

After World War 2, fluid dynamics problems became a great challenge to scientists and engineers to keep solving them analytically, specially aircraft related problems. New inventions and discoveries increased significantly the difficulty and the complexity of studies and designs. This proved essentially to the development of the numerical methods applied to fluid mechanics and the so called Computational Fluid Dynamics.

In addition to that, the invention of the computer and the quick and exponential growth of its power, resulted in a huge expansion of the CFD branch of knowledge.

Apart from that, the main reason of this growth is that today's industry tendency aims to cut down all costs as much as possible. When designing a new product or system, it is much cheaper to simulate and optimise it computationally rather than building a prototype for every design modification proposal.

Applying the CFD basis to the design of a system has many advantages over the experimental way. First of all, it gives an enormous versatility in means of optimisation. For instance, it is easy to change design parameters without increasing too much the complexity of the problem, in contrast, it would be necessary to build another experimental prototype.

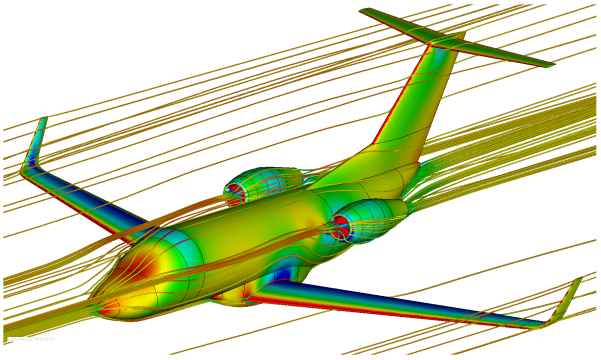

Figure 2.3: CFD simulation of an aircraft. Extracted from [2]

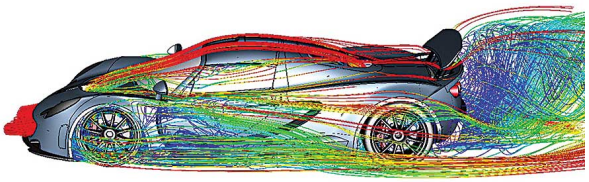

Figure 2.4: CFD simulation of racing car. Extracted from [3]

Secondly, although computers are necessary to carry out a simulation, these allow to develop many of them, which, in the long term, results to be incredibly cheaper than the other way.

Unfortunately, depending on the complexity of the simulation, it may take a great amount of computation time. However, this time has been continuously reduced over the decades thanks to several reasons. First of them, the computational power available has grown exponentially since the beginnings of this knowledge branch. In addition, many more efficient solving techniques have been implemented.

Nowadays, Computational Fluid Dynamics approaches are widely used in many sectors. From aircraft design or automotive industry to biomedical advancements.

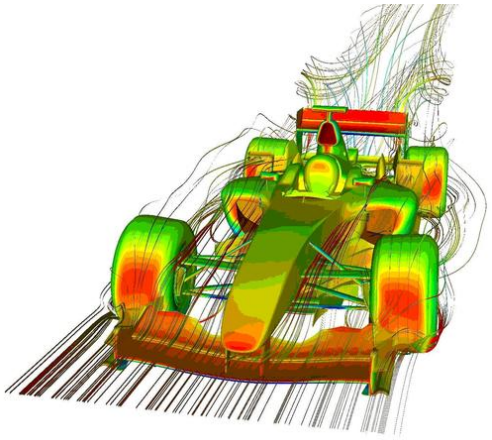

Figure 2.5: CFD simulation of F1 racing car. Extracted from [4]

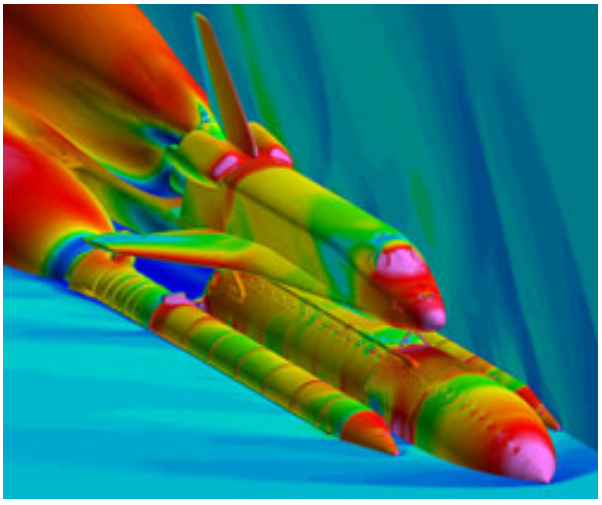

Figure 2.6: CFD simulation of Space Shuttle. Extracted from [5]

Although there are a great amount of different algorithms, methods and techniques applied to the field, all of them have a common structure.

Geometry.

Given a problem, it is necessary to identify its geometry. Define all its components, specify, if necessary, which hypothesis can be assumed on each of the studies. Determine which are the conditions of the problem, for instance, the walls temperature, the flow initial speed, etc.

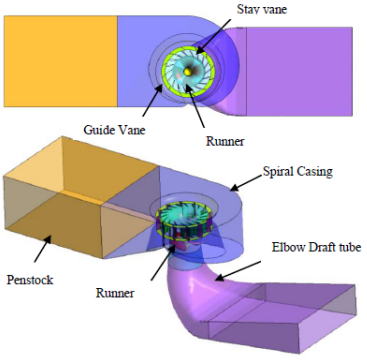

Figure 2.7: Vertical Kaplan Turbine geometry. Extracted from [6]

Meshing and resolution.

Then, in order to apply the numerical methods to solve the equations, it is needed to divide this geometry in a determined number of parts, this is known as spatial discretization. There are several numerical techniques to make this division, Finite Element Method (FEM), Finite Difference Method (FDM) and Final Volume Method (FVM).

All of them are very similar in terms of geometry discretization, with minor variations. However, the major differences comprise the way how equations are discretized and solved.

After that, it is necessary to discretize the fluid flow PDE (Partial Differential Equations) and apply them to the created elements of the geometry to solve them.

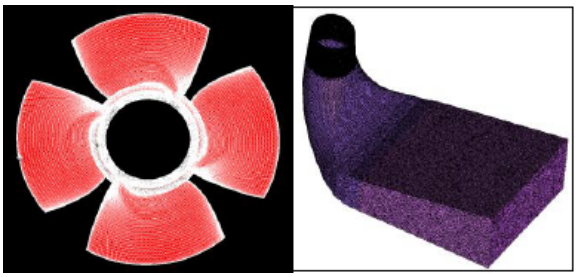

Figure 2.8: Meshing of different components of Kaplan Turbine. Extracted from [6]

Simulation and post-processing.

Finally, once the simulation has been carried out, it is time for post processing and analysis and validation of the obtained results.

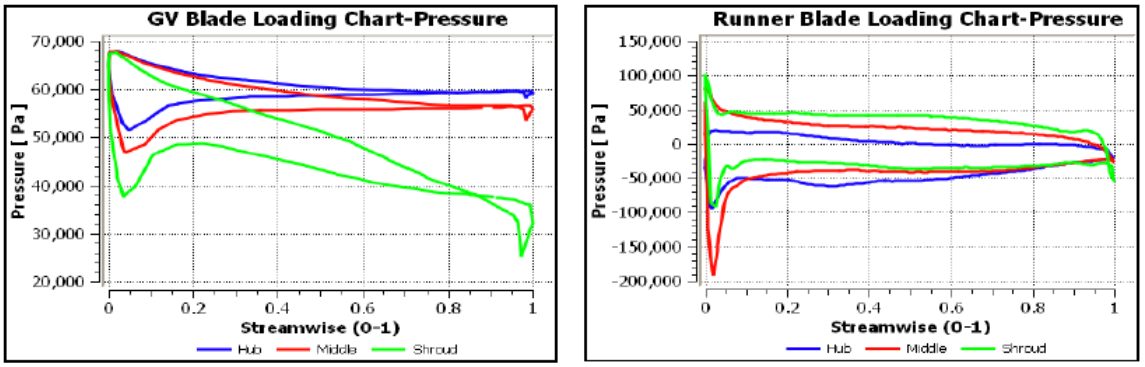

Figure 2.9: Analysis and post-processing of the results obtained. Extracted from [6]

Chapter 3

Laminar regime

3.1 Theoretical framework

In fluid mechanics, laminar flow or laminar regime takes place when a fluid flows in orderly and parallel layers with no disruption between them. There are no transverse flow or currents. In the case of a channel, all the fluid particles move parallel to its walls, as there can be seen in figure 3.1.

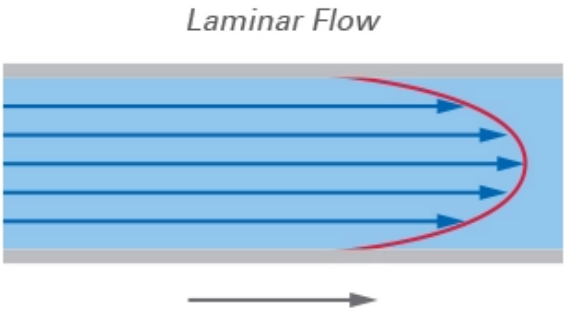

Figure 3.1: Laminar flow velocities profile through a channel. Extracted from [7]

This situation is mostly characterised by small velocities. Since these are relatively low, the flow is characterised by a high momentum diffusion in comparison to momentum convection (advection). This means that, in this kind of flows, it is more likely for physical properties to move through the fluid because of gradients rather than being moved by the flow.

There is virtually no mixing between layers. fluid particles moved on observable paths or streamlines and it is in this regime when viscosity plays a significant part.

For more information related to the physical phenomena involved in the laminar regime go to [19].

The main parameter that splits a problem between laminar and turbulent regime is the Reynolds number (section 2.3). This parameter quantifies how fast is the flow moving in comparison of how viscous it is. At low velocities, Reynolds number is relatively small. Increasing this means rising the flow rate of the fluid and making it less laminar, less orderly, until turbulent regime is achieved.

From the point of view of Computational Fluid Dynamics, laminar regime is characterised mainly by the required computational resources. Since the velocities are low, and so other phenomena like heat transfer doesn't play a significant part there is no need for a great com-

putational power. For instance, one aspect that increases enormously the required computing resources are variables' gradients. In this regime, these are relatively low.

In addition, there can be made several assumptions about the flow to decrease the power needed. In the following section will be presented the hypothesis made for the laminar flow characteristics in this project.

3.1.1 Hypothesis and simplifications made

In this project, there have been made several assumptions that modify the problems slightly and also cuts down the amount of computational resources necessary to carry out the simulations.

This modifications vary from fluid's physical properties to equation's simplifications.

Continuous flow distribution

Although the resolution is numeric instead of analytic, it is assumed that the flow has a big enough amount of molecules to consider it and its physical properties variation to be continuous in time and space.

Bi-dimensional flow.

This assumption has been made in order to cut down the computational power necessary to carry out the simulations. The problem, initially three-dimensional has been reduced to a bi-dimensional. The problem geometry has been considered as deep enough in Z dimension to only take into account flow variations in X-Y plane. This reduces the amount of equations that must be solved and so the time and resources needed.

Constant density

In this section of the project, laminar regime, the density of the fluid has been set to be constant in all the spatial and temporal domain. Considering it as incompressible isn't an assumption that may vary a lot the final results in case of not doing it.

If the fluid is a liquid, these suffer tiny density variations in comparison with gases. But also, if this the case, if flow speed is small enough ($M < 0.3$), the fluid can be considered as incompressible. This is the case of laminar regime, characterised by low velocities.

Constant fluid viscosity.

Kinematic and dynamic viscosity vary with fluid's physical properties such as temperature or pressure. However, these changes not only are almost negligible due to selected flow regime, but also their effects on the overall behaviour and simulation of the fluid don't play a significant part.

In addition, this change simplifies slightly the equations to solve and also reduces the necessary computing power.

Newtonian fluid

Depending on the fluid type there can be different modifications in the equations and in fluid's behaviour in the simulations. In this case there has been chosen to consider the fluid as Newtonian. This means that viscous stresses are linearly and directly proportional to the local rate of change and deformation of the flow field.

The viscous stresses have the following expression.

$$\tau = -\mu \cdot (\nabla \mathbf{u} + \nabla \mathbf{u}^{\mathbf{T}} - \frac{2}{3} \nabla \cdot \mathbf{u}) \tag{3.1}$$

In case of incompressible flow, its divergence ($\nabla \cdot \mathbf{u}$) is null in all cases. In addition to that, the hypothesis of constant fluid viscosity mentioned before leads to the following expression of the diffusion term in the Navier-Stokes Momentum Conservation equation.

$$\nabla \cdot \tau = \mu \nabla^2 \mathbf{u} \tag{3.2}$$

Boussinesq approximation.

In order to determine which is the effect that gravity and temperature is going to have on fluid's behaviour, it has been selected to use Boussinesq's theory.

This approximation is only valid when density changes are much smaller than fluid's density ($\Delta\rho \ll \rho_0$). Therefore, taking into account that the study cases are incompressible, it can be considered as a suitable hypothesis.

$$g \longrightarrow g \cdot (1 - \beta \cdot (T - T_0)) \tag{3.3}$$

This approximation has the same overall effect on the fluid as density changes would have. The hotter the fluid is (the smaller its density would be) the faster it ascends and the opposite for small temperature areas.

For further information about the Boussinesq approximation go to [20] and [21].

Constant thermal conductivity.

As in the previous case, thermal conductivity of a fluid varies with its physical properties, specially temperature. Nevertheless, this change can be assumed without major variations in the final results, and it also eases slightly the resolution of the equations.

Constant specific heat coefficient.

Repeatedly, specific heat coefficient of a fluid varies with its physical properties.

However, in order to ease the resolution of Energy conservation equation dramatically, it has been considered as constant. As it can be seen in section 2.2.5, the equation 2.20 has as heat variables specific enthalpy and temperature.

So, in order to simplify them into a unique work variable, considering the specific heat coefficient as constant is necessary. If so, enthalpy can be written as follows.

$$dh = C_p \cdot dT \tag{3.4}$$

Negligible energy pressure dissipation.

Although it is part of the Energy conservation equation (2.20), it doesn't play a significant part on fluid's behaviour. Pressure energy dissipation comes due to high rates of change on it. However, in laminar regime these variations are relatively small, and so the energy dissipation due to them.

Negligible viscous energy dissipation.

Again, this viscous dissipation term is part of the Energy conservation equation. Nevertheless, it is rarely important. It is taken into account only for simulations of high speed flows and narrow capillaries where viscous heating is not negligible.

In this flow regime, it doesn't play a big role on the Energy Conservation equation effects, and also removing it cuts down a lot the computing power and implementation time needed.

3.1.2 Laminar regime Navier - Stokes equations.

Next up the Navier - Stokes conservation equations (Mass, Momentum and Energy) with the hypothesis and modifications previously mentioned are presented.

- **Mass conservation equation.**

$$\nabla \cdot (\mathbf{u}) = 0 \tag{3.5}$$

$$\frac{\partial u}{\partial x} + \frac{\partial v}{\partial y} = 0 \tag{3.6}$$

- **Momentum conservation equation.**

$$\frac{\partial \mathbf{u}}{\partial t} + \nabla \cdot (\mathbf{u}\mathbf{u}) = -\frac{1}{\rho}\nabla p + \frac{\mu}{\rho}\nabla^2 \mathbf{u} + g \cdot (1 - \beta \cdot (T - T_0)) \tag{3.7}$$

X axis.

$$\frac{\partial u}{\partial t} + \nabla \cdot (\mathbf{u}u) = -\frac{1}{\rho}\frac{\partial p}{\partial x} + \frac{\mu}{\rho}\nabla^2 u + g_x \cdot (1 - \beta \cdot (T - T_0)) \tag{3.8}$$

Y axis.

$$\frac{\partial v}{\partial t} + \nabla \cdot (\mathbf{u}v) = -\frac{1}{\rho}\frac{\partial p}{\partial y} + \frac{\mu}{\rho}\nabla^2 v + g_y \cdot (1 - \beta \cdot (T - T_0)) \tag{3.9}$$

Since the flux has been considered as bi-dimensional in X-Y plane, there is no need for considering Z axis equations anymore.

- **Energy conservation equation.**

$$\frac{\partial T}{\partial t} + \nabla \cdot (\mathbf{u}T) = \frac{K}{\rho C_p} \nabla^2 T \tag{3.10}$$

These are the equations which will be used on this part of the project.

3.1.3 Laminar regime study cases.

To give a better insight of the simulation cases and their particularities, each of them will be presented in this section before showing obtained results in their respective sections later.

LID Driven Cavity.

The first of the 3 laminar simulated problems is one of the most known cases in CFD field, LID Driven Cavity.

It consists on a cavity opened only on the upper side, in which a fluid flows parallel to. In order to give a better insigh of this problem it is its presented the scheme in figure 3.2.

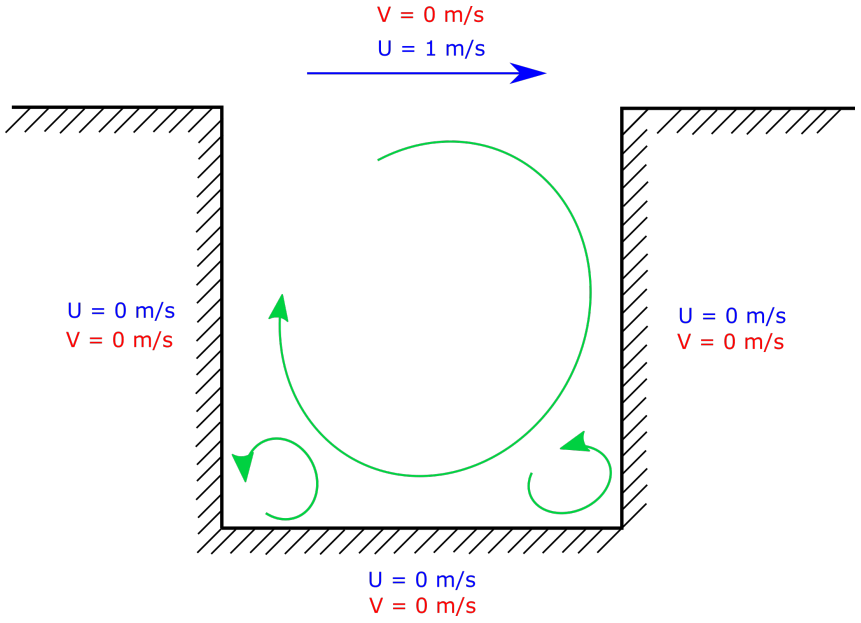

Figure 3.2: LID Driven Cavity case scheme

As it can be seen in the scheme, on the top of the cavity the fluid only has horizontal velocity, while vertical is null. On the rest of the walls, non-slip condition is imposed. This means that right on them (on its surface) all the velocities (U and V) remains null during all the simulation.

At low Reynolds numbers (high viscosity and low speeds), it is only possible to appreciate the large central vortex. However, the bigger the Reynolds is, the more easy to see little vortexes at

the corners of the cavity. This phenomena will be shown in a more detailed way in LID Driven Cavity results section (section 3.3).

LID Differentially Heated.

The second laminar regime study case is known as LID Differentially Heated or LID-Driven Differentially Heated. It consists on an enclosed cavity with the vertical walls at different temperatures, while the top and bottom are completely adiabatic (thermally isolated).

This simulation case has two main differences from the other laminar regime problems. First, it is the only one in which Energy Conservation equation must be solved. This process will be explained later. And secondly, it is the only one in which gravity is considered. Otherwise, since there is no velocity source (like in LID Driven Cavity case), the fluid wouldn't move no matter the walls' temperatures.

In the following figure 3.3 it is presented the problem scheme.

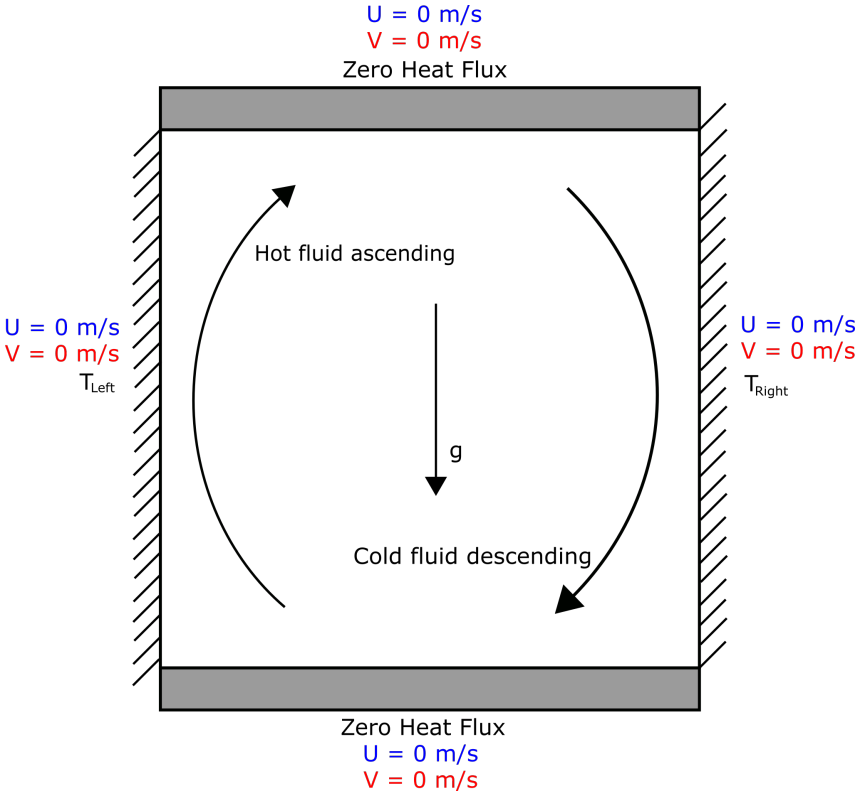

Figure 3.3: LID Differentially Heated case scheme

In the case of figure 3.3, left wall's temperature (T_{Left}) is considered to be higher than the right one (T_{Right} in the picture). Due to this fact, the fluid, when approaching first one, heats up and ascends, while when getting closer to the right wall, loses its heat and goes down. This creates an infinite loop that ends in a steady state.

Again, non-slip condition is imposed on every solid wall, turning all the horizontal and vertical velocities on them to zero.

Finally, it is important to mention that, in this case, the main parameter that governs the fluid behaviour (velocity and viscosity) is the Rayleigh number (see section 2.3). This happens due to the important role that heat transfer plays in this problem.

Square Cylinder.

Last case of simulation is known as Square Cylinder or Flow past a Square Cylinder. As its name already indicates, it consists on a square cylinder around which there is fluid flowing.

To have a better insight of the problem, it is presented its scheme in figure 3.4.

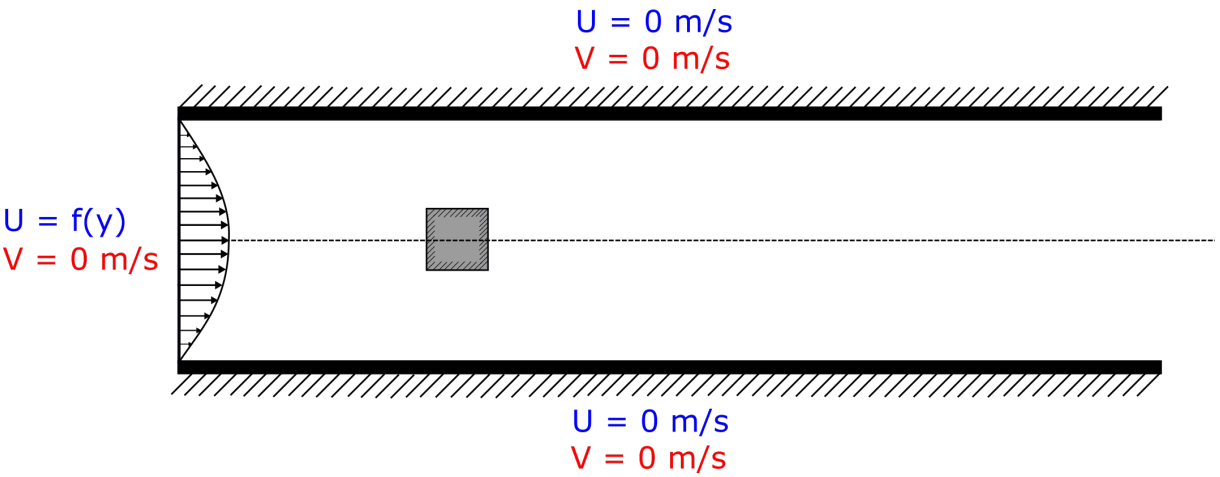

Figure 3.4: Square Cylinder case scheme

Again, non-slip condition is imposed on every solid wall (top and bottom walls). On the other hand, the inlet of the system (the fluid entrance) is characterised by a parabolic horizontal velocity profile. The outlet boundary condition is considered to be null gradients on both horizontal and vertical velocities.

Apart from being the most difficult to implement and the problem that requires the most computational resources, it has a special characteristic that differs it from the other two previously presented.

The main parameter that governs the flow is Reynolds number, as in LID Driven Cavity case. In this problem, rising this value made small lateral vortexes to be more appreciable, but they remained in an steady state.

However, in Square Cylinder, increasing Reynolds number above a called *Critical* Reynolds causes moving vortexes to appear behind the cylinder. These are known as $Von - Kárman$ *Vortexes*. To have a better understanding of this phenomena, see Square Cylinder results in section 3.5.

3.2 Numerical framework

As it has been previously mentioned, no one has ever been able to give a solution for generic Navier - Stokes equations, only a few times with highly restricted boundary conditions. However, the aim of this project comprises several study requirements and conditions that would be impossible to fulfil with an analytic approach. Therefore, numerical methods are indispensable to get the desired results.

In this project, Finite Volume Method (FVM) is used. This is a method for discretizing and solving partial differential equations in algebraic form.

This numerical method has several advantages. First, it is relatively easy to adapt the discretization to the selected geometry, it has a great flexibility. In addition, it imposes the conservation of the physical properties of the equations and gives a great insight and intuitive idea while discretizing them.

It consists on dividing the study domain in a determined number of non-overlapping fixed volumes. All of these have a node right on each of their centroids. In figure 3.5 these control volumes are presented as cubes (or squares in 2D). However, there are many other geometrical shapes these can be described with, such as tetrahedrons, pyramids, prisms or hexahedrons in 3D or in 2D, triangles, circular sections, etc...

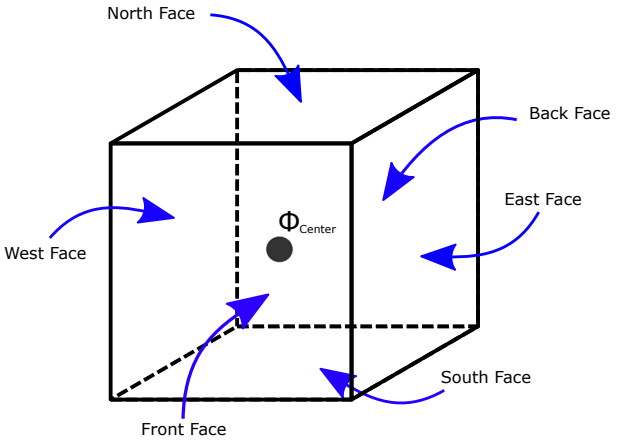

Figure 3.5: Finite Volume Method representation

FVM considers that, the value of any physical variable in the volume is its the mean value in all of the volume.

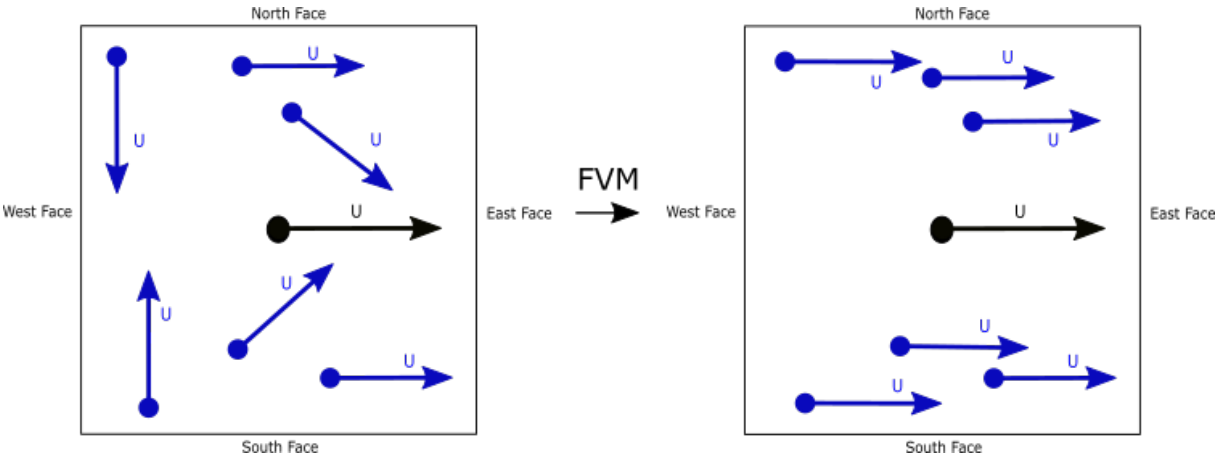

Figure 3.6: FVM discretization basis representation

Finally, this mean value is fixed to the central node of the volume (figure 3.5). Obviously, this isn't a perfect way to represent reality. Real World physics are continuous, while here it is tried to define them with discrete values. Nevertheless, these methods have a great accuracy when there are enough volumes representing the study domain.

3.2.1 Spatial discretization

In order to solve the fluid flow equations, it is necessary first to discretize the physical domain. To do that, this must be divided in a determined number of Control Volumes based on already exposed FVM basis.

A group of these volumes (or nodes) creates an structure of cells called "*Mesh*" or "*Grid*". There are different types of meshes and ways to discretize the geometry as a function of the problem complexity, computational resources available or fluid conditions.

Types of meshes.

- **Structured mesh.**

  This type of grids has a clear and structured order for nodes and volumes location. Each of them has a constant number of neighbours to which regular connectivity can be expressed as a two or three dimensional matrix. This simplifies a lot the process of meshing and discretizing the equations. Additionally, it provides the option to use solving algorithms that require less computational power than other types of meshes.

  Structured meshes can be splited in two groups.

  - **Orthogonal mesh.**

    In this case, all the control volumes have the same shape and structure. In addition, all the fluxes of physical variables like velocities or temperatures are normal to volume's faces. Depending on the dimensions of each control volume, these meshes can be uniform, if all of them have the same size, or non uniform, if they vary.

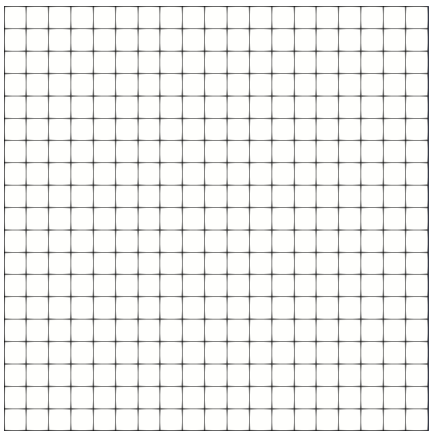

Figure 3.7: Structured Orthogonal Uniform mesh

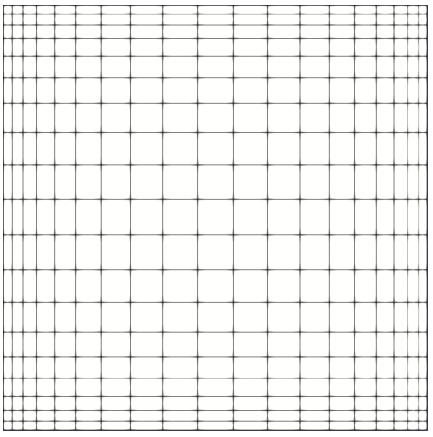

Figure 3.8: Structured Orthogonal Non-Uniform mesh

– **Non orthogonal mesh.**

These types of meshes are used to adapt the control volumes to the geometry boundaries of the problem. They allow to represent more complex geometries than orthogonal meshes. However, fluxes through the surfaces are no longer normal to them, so the implementation difficulty rises.

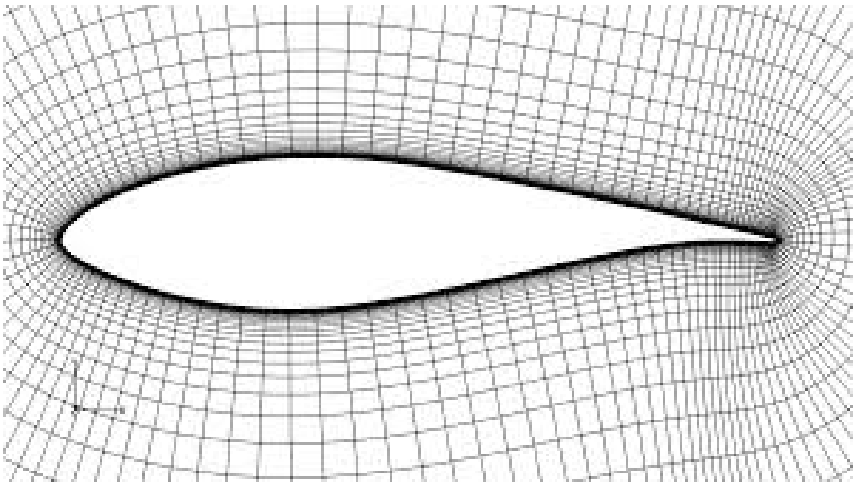

Figure 3.9: Non orthogonal mesh for airfoil simulation. Extracted from [8]

- **Unstructured mesh.**

Unlike structured meshes, these don't have a constant number of neighbours around them. This allows to discretize a great range of different and complex geometries in addition to setting many different and useful options to the grid. However, the difficulty of meshing and equation's solving process increases dramatically in front of a structured grid.

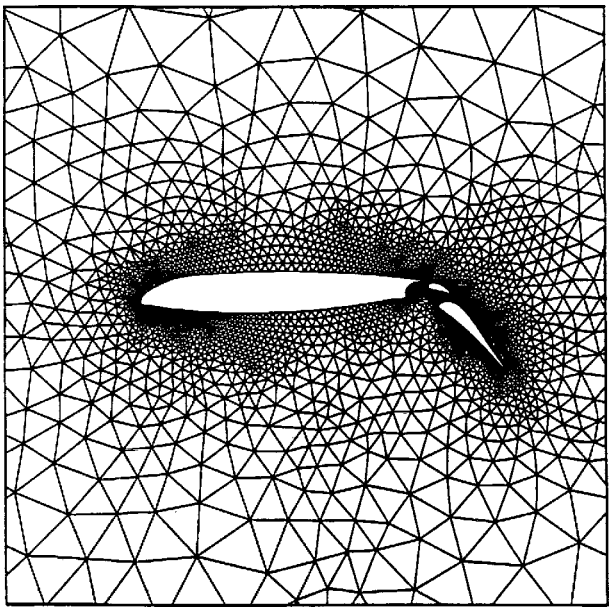

Figure 3.10: Unstructured mesh for airfoil simulation. Extracted from [9]

- **Hybrid mesh.**

  This type of mesh contains portions of structured and unstructured meshes. Regular and easy parts of the geometry are discretized using structured grids, while more complex ones (or where it is more useful) use an unstructured mesh.

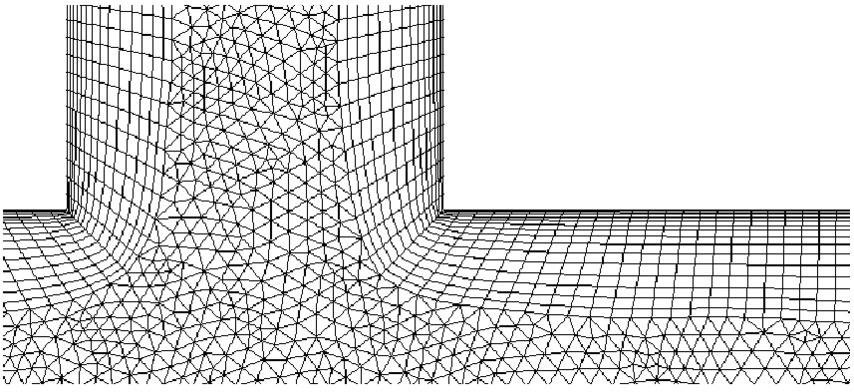

Figure 3.11: Hybrid mesh. Extracted from [10]

Apart from that, there are many meshing techniques beyond initial discretization. This is case for instance of adaptive meshes refinement, moving or rotating grids, etc..

In this project, structured orthogonal uniform and non-uniform meshes are used. Since selected geometries for the simulations are fixed and not highly complex, there is no need for implementing non-orthogonal or unstructured meshers.

Additionally, it is necessary to select one last characteristic of the grid. If it is going to be a *Collocated Mesh* or a *Staggered Mesh*.

In bi-dimensional, incompressible and cartesian-based CFD problems there are 3 main variables to which a mesh has to be created. Pressure and horizontal and vertical velocity, P, U and V respectively. In what comes to the temperature variable, this share mesh with the pressure.

Depending on the type of grid (Collocated or Staggered) there will be necessary to have 1 or 3 spatial grids.

- **Collocated mesh.**

  In this case, a node is located at the centroid of each control volume (as usual in FVM). All of aforementioned variables (P, U and V) of the control volume, have to be spatially set on this node. Only 1 mesh is necessary to discretize the domain.

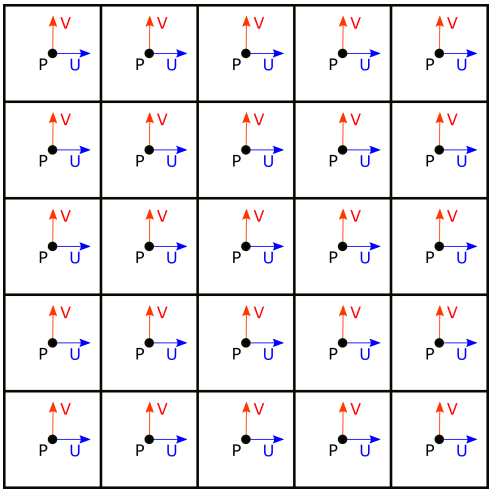

Figure 3.12: Structured Orthogonal Uniform Collocated mesh scheme

Although this may seem an easy and suitable way to discretize the domain for CFD beginers, it has a great disadvantage.

While solving velocities' field in Navier-Stokes equations, pressure must be obviously taken into account. However, this kind of discretization decouples the velocities and the pressure of each node. This numerical phenomena is known as *Checkerboard*.

To give a better insigth, it is presented the next problem. Imagine this is the pressure field of an arbitrary case (figure 3.13). It is necessary to determine the velocity U_2. To do that, pressure gradient of the node $N2$ must be determined among other parameters.

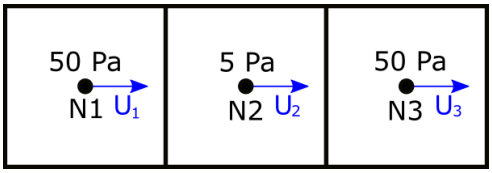

Figure 3.13: Checkerboard case representation

However, the pressure of this node $N2$ (5 Pa) isn't used to calculate it. In collocated meshes *West* and *East* neighbours' pressure are used.

$$\frac{\partial P}{\partial x} = \frac{50\ Pa - 50\ Pa}{\Delta X} = 0$$

The pressure and the velocities decouple. This generates numerical instabilities and oscillations of the results.

There are techniques to avoid this problem using a Collocated mesh. Nevertheless, in this project there has been chosen to use Staggered meshes for the laminar regime part.

- **Staggered mesh.**

  Unlike previous case, choosing a staggered mesh means creating 3 different grids. One for pressure, P, one for horizontal velocity, U, and last one, for vertical velocity, V.

  Pressure mesh remains equally in location to the previous Collocated mesh. However, U and V nodes are placed exactly at the surfaces of pressure's control volumes. Horizontal velocity located at the vertical walls (West and East) and vertical velocity at horizontal walls (South and North) (figure 3.5).

  Next up it is presented an structured orthogonal uniform staggered mesh (figure 3.14).

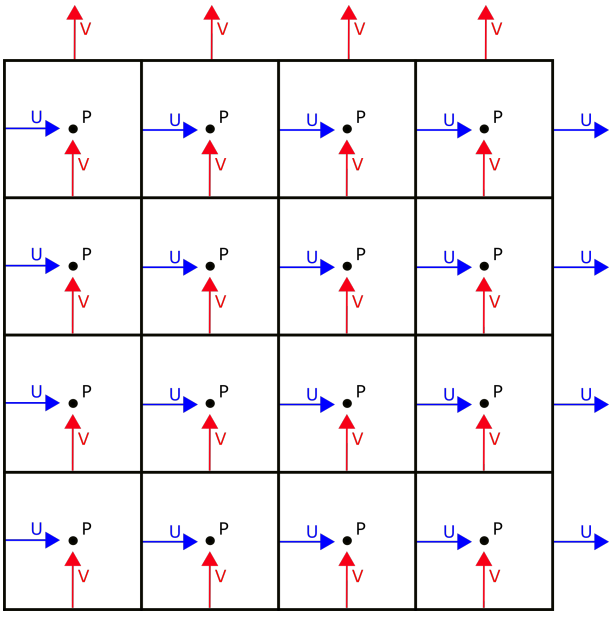

Figure 3.14: Structured Orthogonal Uniform Staggered mesh scheme

In this case, there is no Checkerboard-related problem. When calculating horizontal or vertical velocities (U or V respectively), there isn't a pressure node right on the same location. This allows to compute pressure gradients without the issue of decoupling.

In addition, this mesh configuration ease the implementation of the discretized equations in case of using FVM (as it has been done).

Having 3 different meshes each of them with a variable rises the implementation difficulty and the risk of making programming errors that may give wrong results. Nevertheless, this type of mesh gives great stability and avoid problems like mentioned Checkerboard.

As shown in figures 3.15, 3.16 and 3.17, the combination of these 3 meshes creates the grid on figure 3.14.

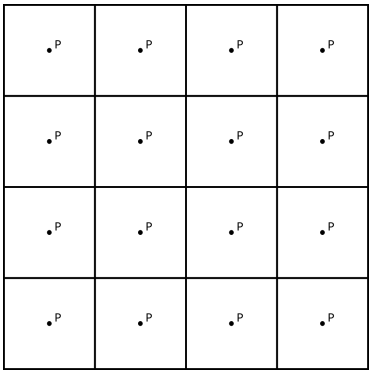

Figure 3.15: Pressure (P) mesh

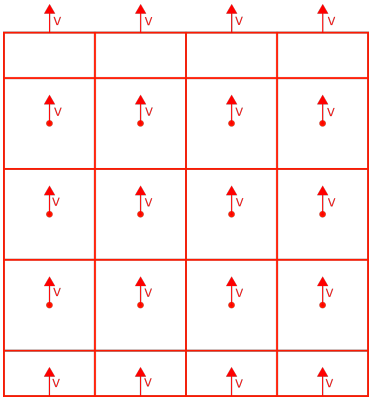

Figure 3.16: Vertical velocity (V) mesh

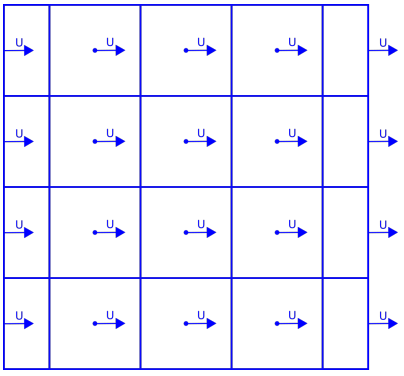

Figure 3.17: Horizontal velocity (U) mesh

Modifications for the Staggered mesh.

Additionally, although it is not considered part of the staggered mesh, it is necessary to locate nodes right on the solid walls.

As it can be seen in figure 3.14, there are horizontal velocity (U) nodes on the vertical walls and so V nodes in horizontal ones. However, to be able to impose boundary conditions to the simulation, it is also needed to locate U nodes on the horizontal walls and V ones in the verticals.

In conclusion, the final staggered mesh have the following shape (figure 3.18).

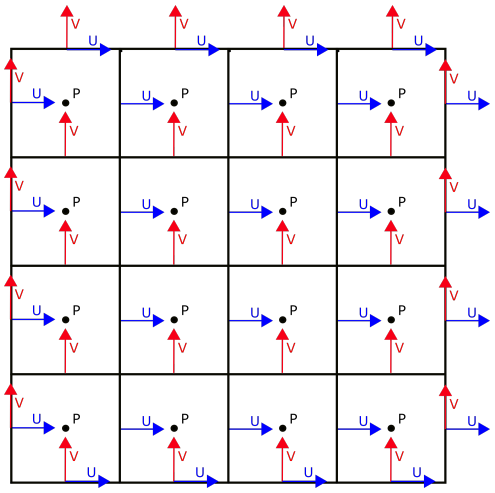

Figure 3.18: Structured Orthogonal Uniform modified Staggered mesh scheme

Meshing of the study cases.

Once all types of different meshes and grid characteristics have been presented, there will be exposed the chosen discretization options for each of the problem cases.

To solve correctly a CFD problem getting accurate results it is essential to choose the adequate meshing options. Is the grid going to be structured, unstructured, uniform... In this case, as it has been previously mentioned, all the meshes developed are structured and orthogonal.

First, it is so important to remark that, since CFD is based on discrete solutions of a continuous physical world, it is impossible to achieve a 100% accuracy. However, the higher the number of discrete points, the more precise results can be obtained.

Other important factor that affects dramatically the meshes is the problem's physical conditions. It isn't the same to simulate the flow around an aircraft travelling at 300 km/h than do it for an 800 km/h velocity. Reynolds number is higher, speeds and pressures gradient are much bigger, etc...

This kind of different conditions in the problems is what makes them to require one type of mesh or other. In this project, there will be different mesh requirements for each case of study and even in the same problem, for different Reynolds or Rayleigh numbers.

The higher this non-dimensional values, the higher the number of nodes on the domain required. Especially where the gradients are higher. This is the case of solid walls.

As it has been mentioned, all solid walls in all the problems have been set with the non-slip condition (velocities drop to zero on the surface). However, these are not null close to them. Therefore, velocity gradients are huge in this area when compared to the middle of the geometry.

This is the main reason why when increasing parameters like Reynolds or Rayleigh numbers it is necessary to locate many control volumes (nodes) near each wall. This is known as "*Mesh Densification*".

All meshes of the laminar regime part of the project are bi-dimensional. This means that they have a certain number of nodes in the horizontal direction and in the vertical (N_X and N_Y respectively).

In order to locate them, there are several mathematical expressions that are commonly used. Next up are presented the ones implemented for these cases.

- **Regular distribution.**

  As its name already indicates, this type of distribution places the nodes in a way all of them are equally separated from its neighbours. All the control volumes have the same size and dimensions.

$$\Delta X = \frac{X_{TOTAL}}{N_X} \qquad \Delta Y = \frac{Y_{TOTAL}}{N_Y} \tag{3.11}$$

  This type of distribution leads to an orthogonal uniform mesh (figure 3.7).

- **Hyperbolic tangent distribution.**

  This is one of the most used types of nodes distribution in CFD problems. As it has been said, one crucial aspect of the meshing process is the densification near the walls. This type of distribution covers this need. It can be observed in figure 3.20 the clear change in node's density near the edges.

This distribution not only locates enough nodes automatically near the walls, but also it reduces the total amount of these needed, cutting down the computational power and time required.

In addition, the grade of densification can be controlled by modiying one parameter. This is the *Stretching Factor* or *Densification Factor* (SF in equation (3.12)). The higher it is, the more nodes are located near the walls.

$$x_i = \frac{L}{2} \cdot \left[\frac{tanh(SF \cdot (\frac{2 \cdot i - NX}{NX}))}{tanh(SF)} + 1 \right] \tag{3.12}$$

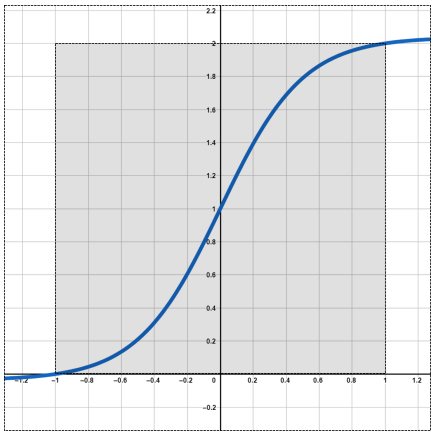

Figure 3.19: Hyperbolic tangent function (SF = 1.5)

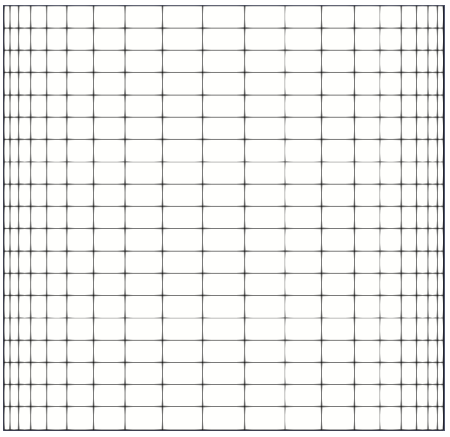

Figure 3.20: Structured Orthogonal Hyperbolic tangent horizontal distribution mesh (SF = 1.5)

It must be mentioned that this node's type of location (as it is shown in figure 3.20) isn't fixed. It can be modified just to take one half of the distribution and increasing the density only in one of the edges. Or, as it has been aforementioned, locating much more or less nodes on the walls.

- **Cosine distribution.**

  Although this type of distribution may seem the same as half hyperbolic tangent, they differ in one crucial aspect. Unfortunately, cosinoidal distribution can't modify nodal density near the walls (this is only possible by changing the total number of nodes in the direction).

  However, despite it is a bit hard to observe in figure 3.22, for the same number of nodes in the horizontal direction, cosinoidal distribution places the first node much closer to the wall than hyperbolic tangent one.

  This is really important for CFD simulations. As it has been mentioned, it is crucial to have enough nodes near the walls where large gradients take place. But, it is even more important the distance between the wall and the closest node. If this isn't small enough, the simulation may give wrong or nonsense results.

$$x_i = L \cdot \left(1 - cos(\frac{i}{NX} \cdot \frac{\pi}{2})\right) \tag{3.13}$$

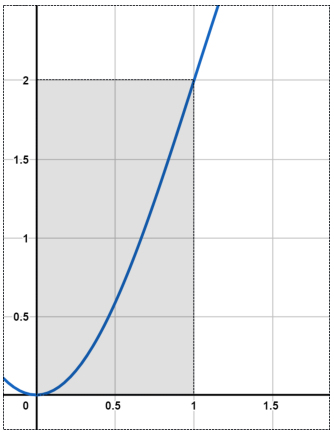

Figure 3.21: Cosine function

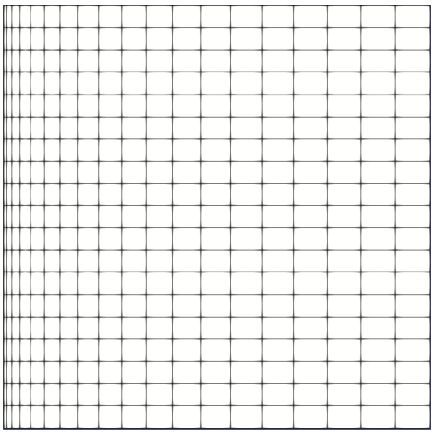

Figure 3.22: Structured Orthogonal Cosinoidal horizontal distribution mesh

Again, this type of distribution can be modified. For instance, changing in equation (3.14) $\frac{\pi}{2}$ for just π or other value, would modify the location of densified areas.

- **Sine distribution.**

  The last type of distribution implemented in the mesher of the laminar regime cases is based on sine expression. It is practically the same as the cosonoidal one. The only difference between them is the densification area. As it can be seen in figures 3.22 and 3.24, the cosinoidal increases the density at the beginning of the distribution while sinoidal does it at the end.

  As it has been said, this type of distribution can be modified to change the densified location. However, from the point of view of programming and meshing in a generic way, it is easier to have both, instead of changing the equations when needed.

$$x_i = L \cdot sin(\frac{\pi}{2} \cdot \frac{i}{NX}) \tag{3.14}$$

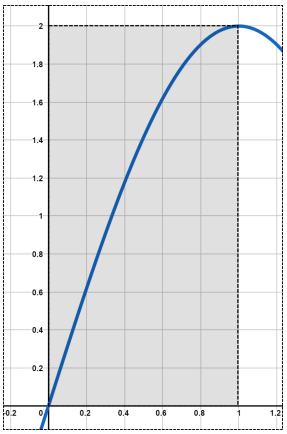

Figure 3.23: Sine function

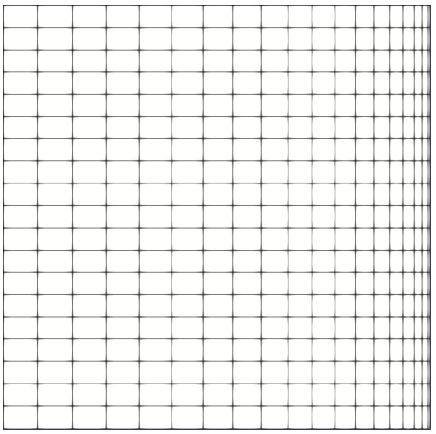

Figure 3.24: Structured Orthogonal Sinoidal horizontal distribution mesh

All of these nodal distributions types have been implemented to the code's mesher. However, not all of them have been used in the same problem case. Next up will be presented which are the nodal configurations that have been chosen to carry out the simulations.

LID Driven Cavity meshing.

In the first study case, LID Driven Cavity, while the Reynolds number of the simulation wasn't higher than 400 approximately, the mesh distributions used were both regular, resulting in a Uniform grid.

However, once this value was surpassed, there was decided to used a hyperbolic tangent distribution on the horizontal direction, and cosinoidal at the vertical. With them , it was possible to densify near the 3 walls of the cavity, while setting in the upper part enough nodes to have an acceptable resolution.

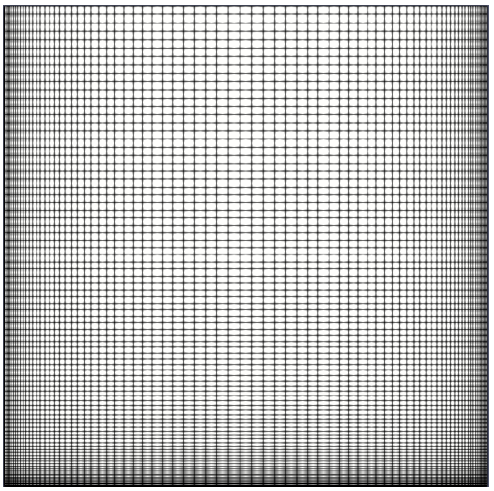

Figure 3.25: LID Driven Cavity mesh

LID Differentially Heated meshing.

For the second study case, LID Differentially Heated, the meshing selected is very similar to the previous problem.

The firsts simulations, with a relatively low Rayleigh number were done with a regular Uniform mesh. Once this parameter was above $1E4$ approximately, horizontal and vertical directions' distributions were changed to hyperbolic tangent, since this time there also a solid wall at the top of the geometry.

This final mesh is presented in figure 3.26.

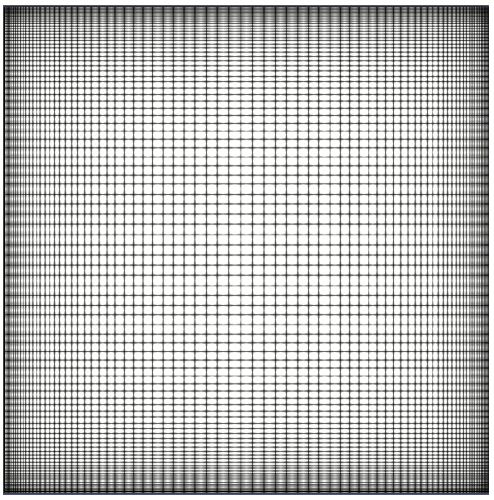

Figure 3.26: LID Differentially Heated mesh

Square Cylinder meshing.

Last case, Square Cylinder, is for sure the most complex problem for meshing in the laminar regime presented cases. This is because the geometry domain (figure 3.4) is divided into 9 different areas (figure 3.27).

Figure 3.27: Square Cylinder geometry division

Each of these zones have to have a different nodal distribution in order to reduce the computational power required but always having a good resolution and acceptable results

To do that, one of the crucial aspects was the meshing around the cylinder, and also the upper and lower walls. It is the critical part of the geometry. If there weren't enough nodes close to it, the simulation would not be possible to carry out or would give nonsense results.

In table 3.1 are presented the distributions selected for the simulations.

Table 3.1: Nodal distribution selected for Square Cylinder case

Zone	X distribution	Y distribution
1	Senoidal/Hyperbolic	Hyperbolic
2	Regular	Hyperbolic
3	Cosinoidal	Hyperbolic
4	Senoidal/Hyperbolic	Regular
5	Cosinoidal	Regular
6	Senoidal/Hyperbolic	Hyperbolic
7	Regular	Hyperbolic
8	Cosinoidal	Hyperbolic
9	Regular	Regular

It is so important to choose the correct distributions on the right areas not just because of all aforementioned about nodal densification, resolution, etc. All the 9 different meshes must match with their neighbours, if not, the codes couldn't even be executable due to meshing nonsenses.

Next up is shown in figure 3.28 the global grid with mentioned nodal distributions for Square Cylinder case.

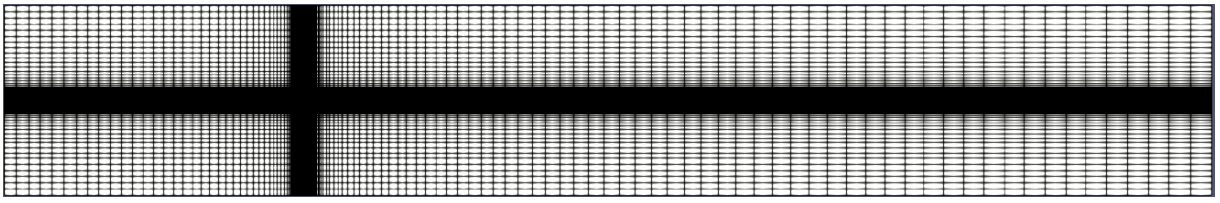

Figure 3.28: Square Cylinder mesh distributions used in the simulations

Additionally is presented a detailed view of the mesh in the cylinder area (figure 3.29).

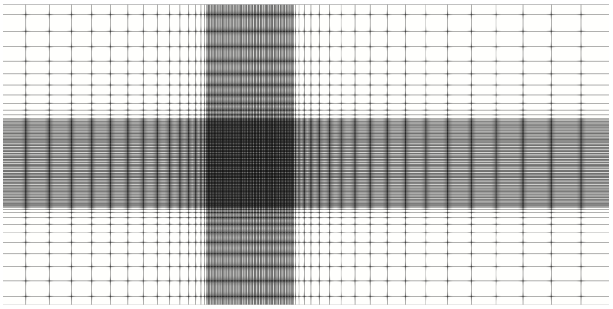

Figure 3.29: Local meshing around the cylinder in Square cylinder case

3.2.2 Resolution of the equations.

Once all the meshes are correctly and fully developed, it is necessary to choose a solving method for the incompressible Navier-Stokes equations.

Fractional Step Method.

To solve the fluid-flow equations, Fractional Step Method (FSM) is selected ([22] and [23]). It is one of the most commonly implemented methods to solve incompressible Navier-Stokes equations. It has several advantages over other numerical techniques.

First, it is easier to program than other ones. It stands out for its simplicity. In addition, it provides a better computational performance than other solving methods.

It is used to solve the Mass and Momentum Conservation equations. In case of the Energy one, it isn't necessary the application of this method but only a time integration technique.

Next up will be presented all the FSM algorithm and explained in a detailed way.

First of all, it is necessary to have the equations that are going to be solved. These are the ones presented in section 3.1.2 (they are already simplified with all hypothesis assumed, section 3.1.1).

Mass and Momentum Conservation equations resolution.

Since this is the resolution of an incompressible fluid problem, it is only necessary to determine pressure (p) and horizontal and vertical velocities (U and V respectively) from these two equations, (3.5) and (3.7).

The first step consist on splitting the Momentum equation (3.7) in three different terms.

$$\frac{\partial \mathbf{u}}{\partial t} = F(\mathbf{u}) + S(p) \tag{3.15}$$

Where:

$$F(\mathbf{u}) = -\nabla \cdot (\mathbf{u}\mathbf{u}) + \frac{\mu}{\rho}\nabla^2 \mathbf{u} + g \cdot (1 - \beta \cdot (T - T_0)) \tag{3.16}$$

$$S(p) = -\frac{1}{\rho}\nabla p \tag{3.17}$$

On the other side of the equation, it is necessary to write the velocity change rate in terms of time steps.

$$\frac{\partial \mathbf{u}}{\partial t} = \frac{\mathbf{u}^{n+1} - \mathbf{u}^n}{\Delta t} \tag{3.18}$$

Reorganising equation (3.15) with this last modification of equation (3.18) the following expression can be obtained.

$$\mathbf{u}^{n+1} = \mathbf{u}^n + \Delta t \cdot F(\mathbf{u}) + \Delta t \cdot S(p^{n+1}) \tag{3.19}$$

Then, a *Predictor* velocity ($\mathbf{u}^*$) must be defined. It is an approximate solution for the momentum equation.

$$\mathbf{u}^* = \mathbf{u}^n + \Delta t \cdot F(\mathbf{u}) \tag{3.20}$$

Combining last expression with equations (3.17) and (3.19), the following can be obtained.

$$\mathbf{u}^{n+1} = \mathbf{u}^{*} - \frac{\Delta t}{\rho}\nabla p^{n+1} \tag{3.21}$$

Here comes the crucial part of the Fractional Step Method. Applying Divergence operator at both sides of equation 3.21 leads to the next expression.

$$\nabla \cdot \mathbf{u}^{n+1} = \nabla \cdot \mathbf{u}^{*} - \frac{\Delta t}{\rho}\nabla \cdot (\nabla p^{n+1}) \tag{3.22}$$

Now, taking into account incompressible Mass Conservation equation (3.5), left term of expression (3.22) can be removed. Therefore the following can be obtained.

$$\frac{1}{\Delta t} \cdot \nabla \cdot \mathbf{u}^{*} = \frac{1}{\rho}\nabla^{2} p^{n+1} \tag{3.23}$$

This expression is known as Poisson's pressure equation. Since the predictor velocity can't satisfy the incompressibility hypothesis at the next time step, Poisson's equation determines the minimum perturbation on the flow that makes predictor to be incompressible [22].

From equation 3.23, it is possible to compute the pressure of the next time step (n+1). Once it has been calculated, U and V velocities can be calculated.

In order to do that, it is only needed to decompose equation (3.21) in Cartesian axis.

Horizontal velocity (u):

$$u^{n+1} = u^{*} - \frac{\Delta t}{\rho}\frac{\Delta p^{n+1}}{\Delta x} \tag{3.24}$$

Vertical velocity (v):

$$v^{n+1} = v^{*} - \frac{\Delta t}{\rho}\frac{\Delta p^{n+1}}{\Delta y} \tag{3.25}$$

Energy Conservation equation resolution.

Unlike previous Mass and Momentum equations, for Energy one there is no need for applying FSM to solve it.

In this case, only it is necessary to reorganise the equation's terms to develop a temporal integration (this last step will be explained in a more detailed way in section 3.2.3).

On the basis of equation (3.10), it is only needed to write it in the following way.

$$\frac{\partial T}{\partial t} = F(T) \tag{3.26}$$

Where:

$$F(\mathbf{T}) = -\nabla \cdot (\mathbf{u}T) + \frac{K}{\rho C_p}\nabla^2 T \tag{3.27}$$

Then, it is needed to write the temperature change rate in terms of time steps.

$$\frac{\partial T}{\partial t} = \frac{T^{n+1} - T^n}{\Delta t} \tag{3.28}$$

Finally, expressions (3.26) and (3.28) can be combined to obtained the following equation.

$$T^{n+1} = T^n + \Delta t \cdot F(T) \tag{3.29}$$

3.2.3 Time integration

To being able to solve the equations correctly during transient period until it achieves a steady state it is necessary to perform a temporal integration during all time steps of the simulation.

There are many different time integration methods, but these can be splited in two main groups.

- **Implicit methods.**

  This type of temporal schemes use the physical information of time step n+1 in order to determine another physical property of the same step. As an advantage over other integration methods, this can handle bigger time steps (Δt). However, since n+1 step variables are unknown, it is necessary to solve a set of equations on each of them. Because of it, these kind of methods are suitable for steady CFD problems.

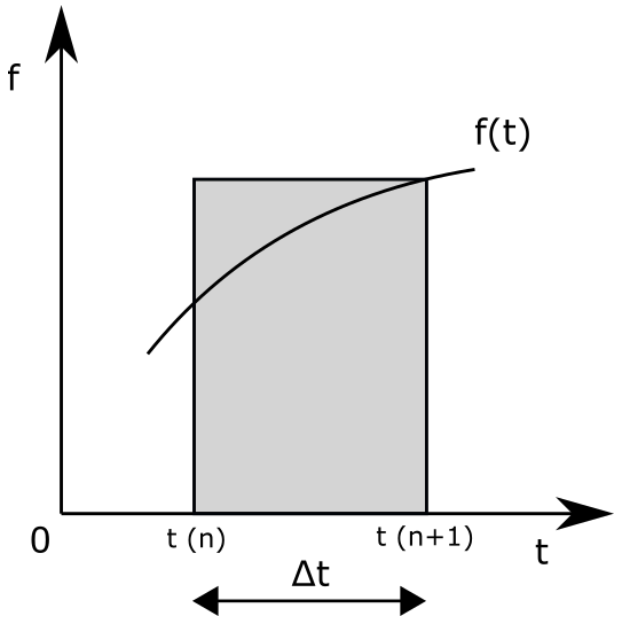

Figure 3.30: Implicit temporal method scheme

- **Explicit methods.**

  Unlike implicit methods, explicit schemes use the physical data information of present (n) or previous time steps (n-1, n-2, ...) to compute next's step one (n+1). On the one hand, these type of methods are computationally lighter. They do not require to solve a coupled system of equations. However, time steps' length (Δt) are relatively smaller than in case of implicit schemes. Nevertheless, these methods are commonly used for transient state simulations.

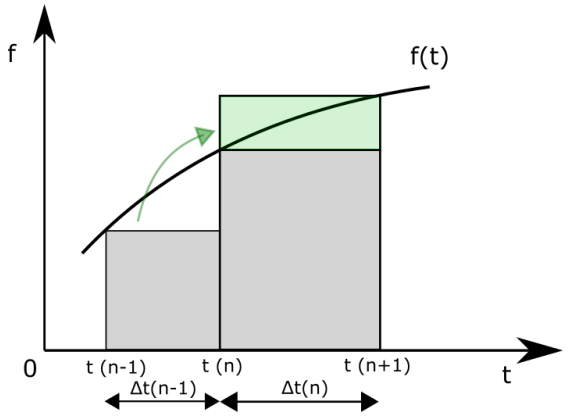

Figure 3.31: Explicit temporal method scheme

In this project, it has been selected to do temporal integration with an explicit scheme, more precisely, a second-order Adams-Bashforth scheme. Its basis consists on determining the property value of next time step by using present and former time steps information.

As it can be observed in section 3.2.2, in many of the final equations appears the term F(u), F(v) or F(T).

These are the terms in which Adams-Bashforth method is applied. They are computed by evaluating them on the present and former time steps and assigning each a certain coefficient.

$$F(u) = \frac{3}{2} \cdot F(u^n) - \frac{1}{2} \cdot F(u^{n-1}) \tag{3.30}$$

Applying this to equations (3.20) and (3.29) leads to the following expressions respectively.

$$\mathbf{u}^* = \mathbf{u}^n + \Delta t \cdot \left[\frac{3}{2} \cdot F(\mathbf{u}^n) - \frac{1}{2} \cdot F(\mathbf{u}^{n-1}) \right] \tag{3.31}$$

$$T^{n+1} = T^n + \Delta t \cdot \left[\frac{3}{2} \cdot F(T^n) - \frac{1}{2} \cdot F(T^{n-1}) \right] \tag{3.32}$$

There is still something in temporal integration process that hasn't been determined yet. To solve all exposed equations, as these has been presented, it is necessary to compute the time steps value (Δt). This is a crucial part of the simulation. If the time step is too small, the

execution of the code may last days until the flow achieves an steady state. However, if it is too large, the simulation may diverge and stop.

Courant–Friedrichs–Lewy condition.

To determine the correct value, Courant–Friedrichs–Lewy (CFL) condition is used. This isn't an exact solution for the calculation of time steps value. However, it is an approximation easy to implement which gives relatively good stability to the simulations. Unfortunately, the demonstration of Δt calculation without this method uses advanced mathematics which are far away from project's scope. More information about this can be found in [24].

CFL condition is based on the following expressions.

$$\Delta t_c = min\left(0.35\frac{\Delta x}{|u|}\ ,\ 0.35\frac{\Delta y}{|v|}\right) \tag{3.33}$$

$$\Delta t_d = min\left(0.20\frac{\rho\Delta x^2}{\mu}\ ,\ 0.20\frac{\rho\Delta y^2}{\mu}\right) \tag{3.34}$$

$$\Delta t_{dh} = min\left(0.20\frac{\rho C_p\Delta x^2}{K}\ ,\ 0.20\frac{\rho C_p\Delta y^2}{K}\right) \tag{3.35}$$

Every time step, it is necessary to compute the minimum of these 3 equations and look for the smallest one.

$$\Delta t = min\left(\Delta t_c, \Delta t_d, \Delta t_{dh}\right) \tag{3.36}$$

Each of these expressions takes into account different flow phenomena that influences simulation's process. Equation (3.33) is based on flow's convection. It is clear that time step value can't be higher than the time needed for the flow to travel from one node to its neighbour. The same is applied to expressions (3.34) and (3.35) for diffusion terms of the Momentum and Energy Conservation equations respectively.

In addition, there are different coefficients on these equations (0.35 in expression (3.33) and 0.20 in (3.34) and (3.35)). Since this method is an approximation, these expressions are set with coefficients smaller than 1 to ensure the stability of the simulations.

Nevertheless, they are not fixed. Along all the simulations carried out, these coefficients have been modified depending on the conditions. For instance, it is suitable to change 0.20 for 0.10 or 0.05 in time step calculation but on the other side, cut down dramatically the total number of nodes of the discretization. It is based on looking for an overall improvement of the simulation performance modifying the different options available.

3.2.4 Discretization of the equations.

Once the spatial and temporal discretizations have been exposed, it is necessary to present how are equations in section 3.2.2 going to be adapted to these.

Next up are exposed all the aforementioned equations to be discretized.

Divergence Theorem.

All the discretizations are based on the application of the Divergence Theorem.

$$(\nabla \cdot \Phi) = \frac{1}{\Omega} \iiint_{dV} \nabla \cdot \Phi \, dV = \frac{1}{\Omega} \iint_{dS} \Phi \cdot \mathbf{dS} \tag{3.37}$$

This theorem is one of the basis of Finite Volume Method. However equation (3.37) is still in continuous mathematics. It is necessary to transform it to discrete values.

$$\frac{1}{\Omega} \iint_{dS} \Phi \cdot \mathbf{dS} = \frac{1}{\Omega} \sum \Phi_f \cdot \mathbf{n} \cdot \Delta S \tag{3.38}$$

- **Poisson's pressure equation.**

$$\frac{1}{\Delta t} \cdot \nabla \mathbf{u}^* = \frac{1}{\rho} \nabla^2 p^{n+1} \tag{3.39}$$

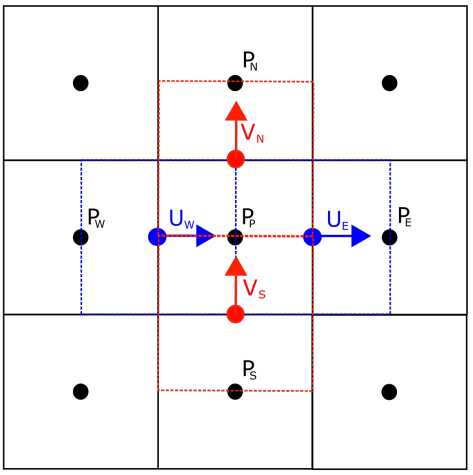

Figure 3.32: Pressure node P discretization scheme

First term:

$$\begin{aligned} \frac{1}{\Delta t} \nabla \cdot (\mathbf{u}^*) &= \frac{1}{\Delta t} \frac{1}{\Omega} \iiint_{dV} \nabla \cdot \mathbf{u}^* dV = \frac{1}{\Delta t} \frac{1}{\Omega} \iint_{dS} \mathbf{u}^* \mathbf{dS} = \sum \mathbf{u}_f^* \mathbf{n} \cdot \Delta S \\ &= \underbrace{\frac{1}{\Delta t} \frac{1}{\Omega} \left[u_e^* \Delta S_e - u_w^* \Delta S_w + v_n^* \Delta S_n - v_s^* \Delta S_s \right]}_{b_p} \end{aligned} \tag{3.40}$$

Next up only the discretization of Predictor's velocity u_P^* will be presented. To see all the other ones go to appendix A in Annex document of this project.

$$u_P^* = u_P + \Delta t \left[\frac{3}{2} \cdot F(u_P^n) - \frac{1}{2} \cdot F(u_P^{n-1}) \right] \tag{3.41}$$

$$F(u_P^n) = -\nabla \cdot (u_P \cdot u_P) + \frac{\mu}{\rho}\nabla^2 u_P + g(1 - \beta(T_P - T_0)) \tag{3.42}$$

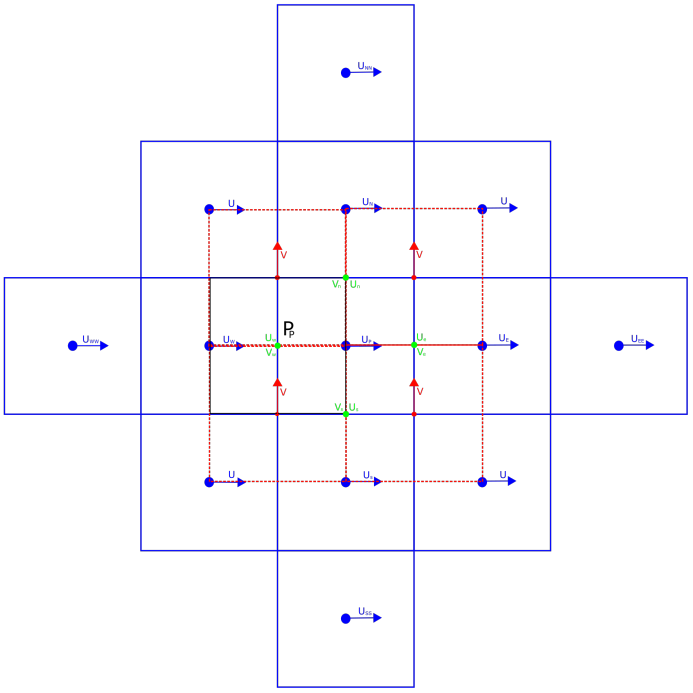

Figure 3.33: F(u) discretization scheme

Discretization of convective term.

$$\begin{aligned} \nabla \cdot (\mathbf{u}u) &= \frac{1}{\Omega}\iiint_{dV} \nabla \cdot (\mathbf{u}u)\, dV = \frac{1}{\Omega}\iint_{dS} \mathbf{u}u\, \mathbf{dS} = \frac{1}{\Omega}\sum u\mathbf{u_f} \cdot \mathbf{n}\Delta S \\ &= \frac{1}{\Omega}\left[u_e u_e \Delta S_e - u_w u_w \Delta S_w + u_n v_n \Delta S_n - u_s v_s \Delta S_s\right] \end{aligned} \tag{3.43}$$

As it can be seen in figure 3.33, these velocities (u_e, u_w, v_n, ...) of the convective term equation (3.43) are not assigned to any node.

Convective schemes.

Since the mathematical discretization locates these velocity terms at the walls of each control volume, it is necessary to compute them as accurately as possible. The aim of the convective or numeric schemes consists on calculating these values.

There are many types of convective schemes. Depending on problem's characteristics there are some that are more suitable or others that may make the simulation to diverge. In addition to that, numeric schemes can be of different orders.

The fact of being a first, second, third, etc.. order convective scheme is related with the accuracy of the simulation. The higher its order, the faster error decreases with more densified meshes.

This may provoke to think the higher order scheme implemented the better to the simulation. However, it becomes very difficult to program and very expensive computationally. In addition, there are many cases in which these cannot be applied to the problem due to different causes.

Next up are presented all the convective schemes implemented and used in the simulations.

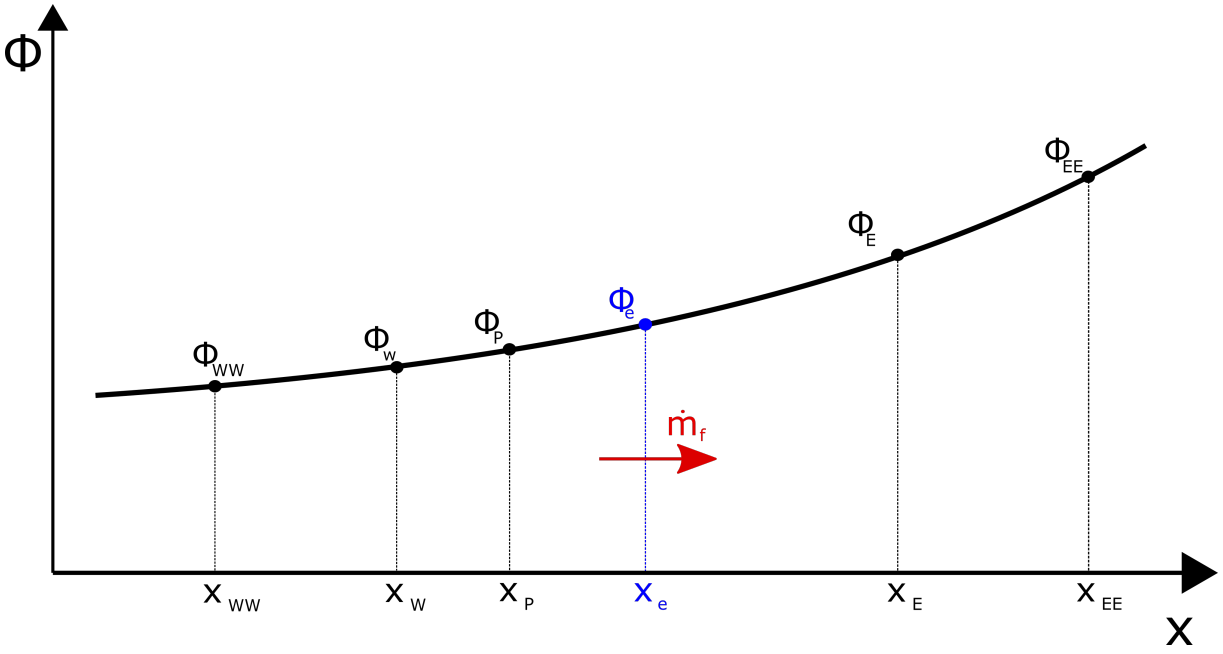

Figure 3.34: Convective scheme diagram

It is necessary first to define what's called "Upstream" (Φ_U), "Center"(Φ_C) and "Downstream" (Φ_D) nodes. The variable that determines these is the mass flow at the face ($\dot{m}_f$)

$\dot{m}_f > \mathbf{0}$		$\dot{m}_f < \mathbf{0}$	
$X_D = X_E$	$\Phi_D = \Phi_E$	$X_D = X_P$	$\Phi_D = \Phi_P$
$X_C = X_P$	$\Phi_C = \Phi_P$	$X_C = X_E$	$\Phi_C = \Phi_E$
$X_U = X_W$	$\Phi_U = \Phi_W$	$X_U = X_{EE}$	$\Phi_U = \Phi_{EE}$

Then, these variables must be normalized in the following way.

$$\widehat{\Phi_C} = \frac{\Phi_C - \Phi_U}{\Phi_D - \Phi_U} \qquad \widehat{x_C} = \frac{x_C - x_U}{x_D - x_U} \qquad \widehat{x_e} = \frac{x_e - x_U}{x_D - x_U} \tag{3.44}$$

Once the non-dimensional values have been determined, it is necessary to apply one of the following convective schemes.

– **Central Difference Scheme (CDS).**

  CDS is a second order convective scheme. It consist on a linear interpolation between the two nodes at the sides of the desired point.

The mathematical expression to determine this value is the following.

$$\widehat{\Phi_e} = \frac{\widehat{x_e} - \widehat{x_C}}{1 - \widehat{x_C}} + \frac{\widehat{x_e} - 1}{\widehat{x_C} - 1}\widehat{\Phi_C} \tag{3.45}$$

– **Upwind Difference Scheme (UDS).**

This first order convective scheme is mainly characterised by the great stability it has. However, its accuracy isn't as good as in case of other schemes. This happens because it generates too much diffusivity (numeric diffusivity).

It consists on setting the value to determine at the wall as the value upstream.

For instance, in case of figure 3.34, since the flow's upstream is x_P, Φ_P would be the property value at the desired point x_e.

The mathematical rule of the scheme is presented next up.

$$\widehat{\Phi_e} = \widehat{\Phi_C} \tag{3.46}$$

– **Second Order Upwind Difference Scheme (SUDS).**

SUDS scheme is based on the same mathematical rule as UDS one. However, as it can be seen in equation (3.47), it also takes into account points location and so the different characteristics of the mesh on that area.

Its mathematical expression is shown next up.

$$\widehat{\Phi_e} = \frac{\widehat{x_e}}{\widehat{x_C}}\widehat{\Phi_C} \tag{3.47}$$

– **Quadratic Upstream Interpolation for Convective Kinematics (QUICK).**

This third order convective scheme uses 2 nodes on the upstream and in the downstream. It has a better accuracy than other lower order schemes. However, one of the main problems it has is that, since it is not limited, it may give results that are not physically possible.

The mathematical equation of the numeric scheme is presented next up.

$$\widehat{\Phi_e} = \widehat{x_e} + \frac{\widehat{x_e}(\widehat{x_e} - 1)}{\widehat{x_C}(\widehat{x_C} - 1)}(\widehat{\Phi_C} - \widehat{x_C}) \tag{3.48}$$

Finally, to calculate the desired value, it is only needed to dimensionalise it from the changes done previously.

$$\Phi_e = \Phi_U + (\Phi_D - \Phi_U) \cdot \widehat{\Phi_e} \tag{3.49}$$

This process of defining the variables, applying the convective schemes, etc... must be done for each of the unknown wall velocities of the convective terms. Additionally, it

needs to be mentioned that, the way to determine these, the selected scheme, can vary hugely the simulation results.

Discretization of viscous stress (Diffusive term).

$$\begin{aligned}\frac{\mu}{\rho}\nabla^2 u &= \frac{1}{\Omega}\iiint_{dV}\frac{\mu}{\rho}\nabla\cdot(\nabla u)\,dV = \frac{\mu}{\rho\Omega}\iint_{dS}\nabla u\,\mathbf{dS} = \frac{\mu}{\rho\Omega}\sum\nabla u\mathbf{n}\Delta S \\ &= \frac{\mu}{\rho\Omega}\left[\frac{u_E-u_P}{\Delta x}\Delta S_e - \frac{u_P-u_W}{\Delta x}\Delta S_w + \frac{u_N-u_P}{\Delta y}\Delta S_n - \frac{u_P-u_S}{\Delta y}\Delta S_s\right]\end{aligned} \tag{3.50}$$

As it can be seen in equation (3.50), the velocity gradients are calculated at control volume's walls, right in the middle of the two nodes involved.

Discretization of the volumetric force term.

$$g(1-\beta(T_P-T_0)) = g_x(1-\beta(T_P-T_0)) \tag{3.51}$$

This term of the equation doesn't need a special discretization. It is only necessary to differ between g_x (horizontal gravity term, usually 0 m/s) for U, and g_y, set to Earth's gravity value (- 9.81 m/s). In addition to this, it must be mentioned that there is no need for temperature adaptation to the mesh since it shares the nodes with the pressure.

Combining all the discretizations above exposed leads to the following expression.

$$\begin{aligned}F(u_P^n) &= -\frac{1}{\Omega}\left[u_e^n u_e^n\Delta S_E - u_w^n u_w^n\Delta S_W + u_n^n v_n^n\Delta S_N - u_s^n v_s^n\Delta S_S\right] \\ &+\frac{\mu}{\rho\Omega}\left[\frac{u_E^n-u_P^n}{\Delta x}\Delta S_e - \frac{u_P^n-u_W^n}{\Delta x}\Delta S_w + \frac{u_N^n-u_P^n}{\Delta y}\Delta S_n - \frac{u_P^n-u_S^n}{\Delta y}\Delta S_s\right] \\ &+g_x(1-\beta(T_P^n-T_0))\end{aligned} \tag{3.52}$$

Second term:

$$\begin{aligned}\frac{1}{\rho}\nabla^2 p &= \frac{1}{\rho\Omega}\iiint_{dV}\nabla\cdot(\nabla p)\,dV = \frac{1}{\rho\Omega}\iint_{dS}\nabla p\,\mathbf{dS} = \frac{1}{\rho\Omega}\sum\nabla p\mathbf{n}\Delta S \\ &= \frac{1}{\rho\Omega}\left[\frac{P_E-P_P}{\Delta x}\Delta S_e - \frac{P_P-P_W}{\Delta x}\Delta S_w + \frac{P_N-P_P}{\Delta y}\Delta S_n - \frac{P_P-P_S}{\Delta y}\Delta S_s\right]\end{aligned} \tag{3.53}$$

This discretizated expression is divided into several "Pressure Coefficients".

$$a_E = \frac{1}{\rho\Omega}\frac{\Delta S_e}{\Delta x} \qquad a_W = \frac{1}{\rho\Omega}\frac{\Delta S_w}{\Delta x} \qquad a_N = \frac{1}{\rho\Omega}\frac{\Delta S_n}{\Delta y} \qquad a_S = \frac{1}{\rho\Omega}\frac{\Delta S_s}{\Delta y} \tag{3.54}$$

$$a_P = a_E + a_W + a_N + a_S \tag{3.55}$$

Finally, discretized first and second term (equations (3.40), (3.54) and (3.55)) of Poisson's pressure equations combined lead to the following expression.

$$a_P P_P^{n+1} = a_E P_E^{n+1} + a_W P_W^{n+1} + a_N P_N^{n+1} + a_S P_S^{n+1} + b_P \tag{3.56}$$

The obtained result of this set of equations previously presented is the pressure field of the step (n+1). The resolution is explained in the following section of this thesis (section 3.2.5).

- **Horizontal velocity equation.**

  Once the pressure values of the step (n+1) have been determined, it is necessary to calculate the velocities and temperature ones.

$$u^{n+1} = u^* - \frac{\Delta t}{\rho}\frac{\partial p^{n+1}}{\partial x} \tag{3.57}$$

  In this case, u^* has been already previously computed, so it is only necessary to determine the second term.

$$-\frac{\Delta t}{\rho}\frac{\partial p^{n+1}}{\partial x} = -\frac{\Delta t}{\rho}\frac{P_E^{n+1} - P_P^{n+1}}{\Delta x} \tag{3.58}$$

$$u_P^{n+1} = u_P^n + \Delta t\left[\frac{3}{2}\cdot F(u_P^n) - \frac{1}{2}\cdot F(u_P^{n-1})\right] - \frac{\Delta t}{\rho}\frac{P_E^{n+1} - P_P^{n+1}}{\Delta x} \tag{3.59}$$

- **Vertical velocity equation.**

  The procedure to determine the vertical velocity is the same as in case of horizontal one. The only difference is the pressure nodes used to compute it. Again, v^* term is already calculated.

$$v^{n+1} = v^* - \frac{\Delta t}{\rho}\frac{\partial p^{n+1}}{\partial y} \tag{3.60}$$

$$v_P^{n+1} = v_P^n + \Delta t\left[\frac{3}{2}\cdot F(v_P^n) - \frac{1}{2}\cdot F(v_P^{n-1})\right] - \frac{\Delta t}{\rho}\frac{P_N^{n+1} - P_P^{n+1}}{\Delta y} \tag{3.61}$$

- **Energy Conservation equation.**

  In case of Energy Conservation equation the discretization is very similar as the one already presented.

$$T^{n+1} = T^n + \Delta t\cdot\left[\frac{3}{2}\cdot F(T^n) - \frac{1}{2}\cdot F(T^{n-1})\right] \tag{3.62}$$

$$F(\mathbf{T}) = -\nabla\cdot(\mathbf{u}T) + \frac{K}{\rho C_p}\nabla^2 T \tag{3.63}$$

Discretization of the convective term.

As in case of Momentum Conservation equation, convective schemes must be used too. However, this time, velocities at the walls doesn't need to be determined. The discretization only require walls' normal velocities. And, as it can be seen in staggered mesh schemes presented (section 3.2.1), velocity grids are located exactly to be normal to pressure/temperature control volumes' walls.

It is only needed to apply explained convective schemes to the calculation of temperatures at the walls.

$$\begin{aligned}\nabla\cdot(\mathbf{u}T) &= \frac{1}{\Omega}\iiint_{dV}\nabla\cdot(\mathbf{u}T)dV = \frac{1}{\Omega}\iint_{dS}\mathbf{u}T\,\mathbf{dS} = \frac{1}{\Omega}\sum\mathbf{u}T_f\mathbf{n}\Delta S \\ &= \frac{1}{\Omega}\left[u_e T_e\Delta S_e - u_w T_w\Delta S_w + u_n T_n\Delta S_n - u_s T_s\Delta S_s\right]\end{aligned} \tag{3.64}$$

Discretization of the diffusive term.

As in previous case, the diffusive term of the conservation equation is discretized as follows.

$$\begin{aligned}\frac{K}{\rho C_p}\nabla^2 T &= \frac{1}{\Omega}\iiint_{dV}\frac{K}{\rho C_p}\nabla\cdot(\nabla T)dV = \frac{K}{\Omega\rho C_p}\iint_{dS}\nabla T\,\mathbf{dS} = \frac{K}{\Omega\rho C_p}\sum\nabla T\cdot\mathbf{n}\Delta S \\ &= \frac{K}{\Omega\rho C_p}\left[\frac{T_E - T_P}{\Delta x}\Delta S_e - \frac{T_P - T_W}{\Delta x}\Delta S_w + \frac{T_N - T_P}{\Delta y}\Delta S_n - \frac{T_P - T_S}{\Delta y}\Delta S_s\right]\end{aligned} \tag{3.65}$$

Combining these last expressions leads to the following equation.

$$\begin{aligned}F(T) &= -\frac{1}{\Omega}\left[u_e T_e\Delta S_e - u_w T_w\Delta S_w + u_n T_n\Delta S_n - u_s T_s\Delta S_s\right] \\ &\quad + \frac{K}{\Omega\rho C_p}\left[\frac{T_E - T_P}{\Delta x}\Delta S_e - \frac{T_P - T_W}{\Delta x}\Delta S_w + \frac{T_N - T_P}{\Delta y}\Delta S_n - \frac{T_P - T_S}{\Delta y}\Delta S_s\right]\end{aligned} \tag{3.66}$$

3.2.5 Solver implementation.

Since the time integration chosen is explicit, the only algebraic equations set that needs to be solved is Poisson's equation. This has been already presented and explained in a detailed way in section 3.2.2 (equation (3.23)).

Its discretization has also been exposed in the previous section. The mathematical expression is the following.

$$a_P P_P^{n+1} = a_E P_E^{n+1} + a_W P_W^{n+1} + a_N P_N^{n+1} + a_S P_S^{n+1} + b_P^n \tag{3.67}$$

This equation repeats consistently for every node of the discrete domain. In order to have a better insight of it, an easy example is presented next up in figure 3.35.

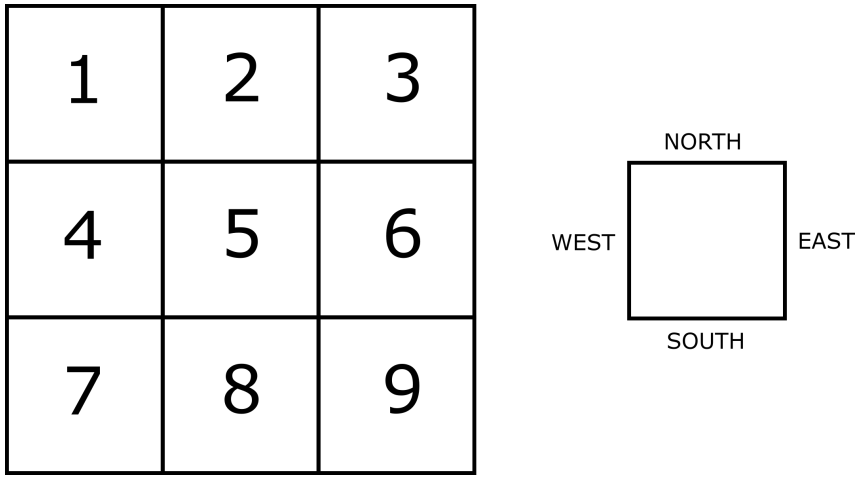

Figure 3.35: Poisson's equation scheme

All nodes' Poisson equations combined can be expressed as a set of equations in a matrix in the form $AX = B$. Imagine the spatial discretization presented in figure 3.35. The discrete domain created has a total of 9 nodes. This means there will be 9 different equations like (3.67) that need to be solved.

$$\overbrace{\begin{bmatrix} a_{P1} & a_{E1} & 0 & a_{S1} & 0 & 0 & 0 & 0 & 0 \\ a_{W2} & a_{P2} & a_{E2} & 0 & a_{S2} & 0 & 0 & 0 & 0 \\ 0 & a_{W3} & a_{P3} & 0 & 0 & a_{S3} & 0 & 0 & 0 \\ a_{N4} & 0 & 0 & a_{P4} & a_{E4} & 0 & a_{S4} & 0 & 0 \\ 0 & a_{N5} & 0 & a_{W5} & a_{P5} & a_{E4} & 0 & a_{S5} & 0 \\ 0 & 0 & a_{N6} & 0 & a_{W6} & a_{P6} & 0 & 0 & a_{S6} \\ 0 & 0 & 0 & a_{N7} & 0 & 0 & a_{P7} & a_{E7} & 0 \\ 0 & 0 & 0 & 0 & a_{N8} & 0 & a_{W8} & a_{P8} & a_{E8} \\ 0 & 0 & 0 & 0 & & a_{N9} & & a_{W9} & a_{P9} \end{bmatrix}}^{A} \cdot \overbrace{\begin{bmatrix} P_1 \\ P_2 \\ P_3 \\ P_4 \\ P_5 \\ P_6 \\ P_7 \\ P_8 \\ P_9 \end{bmatrix}}^{X} = \overbrace{\begin{bmatrix} b_{P1} \\ b_{P2} \\ b_{P3} \\ b_{P4} \\ b_{P5} \\ b_{P6} \\ b_{P7} \\ b_{P8} \\ b_{P9} \end{bmatrix}}^{B} \tag{3.68}$$

As it can be seen in the previous set of equations, the main objective to solve the system and to determine the pressure field (the pressure of each node) is to find the inverse matrix of A.

To do that, there have been implemented and tested, in the code, different linear iterative and non-iterative solvers. These will be shown next up in a more detailed way.

- **Gauss-Seidel.**

  Gauss-Seidel is an iterative solver. It is based on going through every node on the domain supposing its pressure value (or the physical variable to be solved). It is able to

solve every set of equations which matrix is diagonally dominant, symmetric or positive. Unfortunately, it is the slowest solver among all presented.

However, it has en enormous advantage over the rest. This solver method allows to use more than 1 CPU core to solve the entire problem. This is called High-Performance Computing. Using only 1 core with Gauss-Seidel is clearly slower than others, but not using a hundred or thousands of cores.

The solver iterates on every time step and compares the solution with the former one. If the absolute difference is less or equal than a certain value called *Convergence*, the system is known to have achieved an stationary state.

$$|\Phi^{n+1} - \Phi^n| \leq \delta \tag{3.69}$$

- **Tri-diagonal matrix algorithm (TDMA).**

  TDMA is a solver based on the Gaussian elimination. It is designed to solve one-dimensional sets of equations. However, it can be applied to bi-dimensional ones, as it is in this case.

  This method is based on going through every row and every column of the spatial discretization. In every time step it passes through all of them.

  As in previous solver, the set of equations that need to be solved is based on matrix system presented before. However, since TDMA is a one-dimensional solver, it needs to be adapted.

  When going through the rows.

$$a_P P_P^{n+1} = a_E P_E^{n+1} + a_W P_W^{n+1} + b'_P \tag{3.70}$$

$$b'_p = b_p + a_N P_N^{n+1} + a_S P_S^{n+1} \tag{3.71}$$

  And, once it has passed through all the rows, the modification for columns is quite similar.

$$a_P P_P^{n+1} = a_N P_N^{n+1} + a_S P_S^{n+1} + b''_P \tag{3.72}$$

$$b''_p = b_p + a_E P_E^{n+1} + a_W P_W^{n+1} \tag{3.73}$$

  Once the set of equations have been transformed to a linear system, TDMA solver is applied.

$$P_P^{n+1} = \frac{R_P \cdot P_E^{n+1} + Q_P}{a_P} \tag{3.74}$$

  Where R_P and Q_P have the following expression.

$$R_P = \frac{b'_P}{a_P - a_E P_E} \qquad Q_P = \frac{a_E Q_E}{a_P - a_E P_E} \tag{3.75}$$

On every row or column, the method begins the iteration process from last node (NX or NY) to the first one (i = 0, j = 0).

In case of being in these 4 special cases, the equations are modified slightly.

$$R_P = \frac{b'_P}{a_P} \qquad\qquad Q_P = 0 \tag{3.76}$$

Again, the iterative solver is based on comparing the physical property value calculated on present time step with the previous one.

$$|\Phi^{n+1} - \Phi^n| \leq \delta$$

If this condition is true for every node of the spatial discretization, again, the simulation has achieved an stationary state.

In terms of computational time, it needs to be mentioned that, in this project, since only one CPU core has been used, it is much more faster than Gauss-Seidel tests. It may require more calculations per iteration, but it needs less iterations to achieved desired state, which in the end, means a significant amount of time saved.

- **Matrix inverter.**

  Last solver method is based on inverting a matrix. As it can be observed in the set of matrixes (3.68), the pressure variable can be obtained by inverting A matrix and multiplying on the other side.

  This is just what SuiteSparse C++ library used does. Looking at section 3.2.4, there can be seen that Pressure Coefficients (a_P, a_W, a_E, a_N and a_S) are always constant (as the way they have been discretized). This allows to only need to invert A matrix once in all the simulation and then using it every time step. This saves an immense amount of time, and makes this non-iterative method the fastest of the ones presented.

  In this case, there is no need for checking if the results obtained for a certain time steps differ so much or not with the previous step ones. The multiplication of inverted and B matrix already gives the pressure of all nodes.

  Although this method may seem as the most efficient in all cases, it isn't. Inverting extremely large matrix requires a huge amount of RAM memory. In addition to that, when using only one CPU core for the simulation, this is clearly the best option. However, in parallel computation (several CPU cores used at the same time) it becomes really difficult to inverse matrix between different processors.

3.2.6 Simulation algorithm.

To give a better insight of the simulation process, next up will be presented the algorithm and its different steps briefly explained.

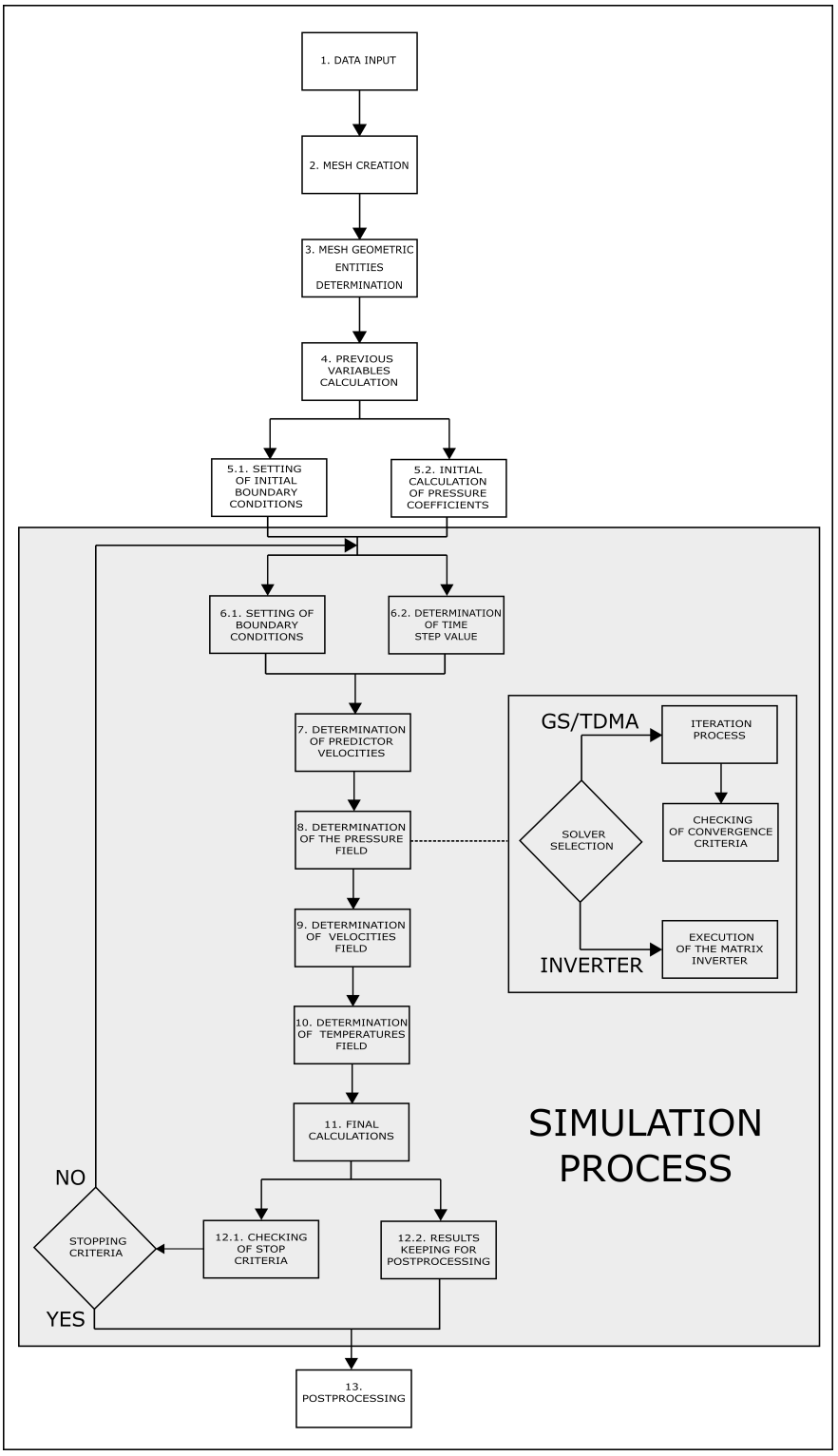

Figure 3.36: Laminar regime simulation algorithm flow scheme

- **1. Data Input.**

  At the beginning of each simulation, it is necessary to define which problem case is going to be solved and the characteristics of this, geometry, boundary conditions, Reynolds or Rayleigh, etc...

- **2. Mesh creation.**

  Once the problem and its geometry have been completely defined, the grid needs to be created, based on the meshing options also entered in the previous step.

- **3. Mesh geometric entities determination.**

  Selected discretization of the equations makes compulsory to determine several mesh parameter like control volumes volume, surfaces value, distance between nodes, etc...

- **4. Previous variables calculation.**

  In the simulation it is necessary to determine some physical data from the one that has been entered at the first step. This is the case for instance of C_p, whose value depends on Prandtl number selected.

- **5.1. Setting of initial boundary conditions**

  In the first steps it is necessary to define the boundary conditions the simulation will begin with.

- **5.2 Initial calculation of pressure coefficients.**

  As it has been previously explained, pressure coefficients (a_P, a_W, a_E, a_N and a_S) are constant, so computationally, it is a better option to determine them before the loop simulation process. In case of using the direct solver (matrix inverter), it is here when the inverted matrix is computed.

- **6.1 Setting of boundary conditions.**

  At the beginning of each step of the simulation is vital to set correctly all desired boundary conditions.

- **6.2 Determination of time step value.**

  As it has been exposed in previous sections, time step value is an essential parameter for the stability of the simulation and for the discretization of the equations.

- **7. Determination of predictor velocities.**

  In this step of the simulation it is necessary to determine the predictor velocities to be able to solve Poisson's pressure equation.

- **8. Determination of the pressure field.**

  As explained, to determine the pressure field it is needed to solve Poisson's pressure equation. To do that, it is necessary to select one of the mentioned solvers for it.

- **9. Determination of velocities field.**

  Once the pressure field has been completely calculated, velocities one can be computed accurately.

- **10. Determination of temperatures field.**

  In case of selecting LID Differentially Heated problem, in which Energy Conservation equation is solved, it is needed to determine the temperatures field following the process and discretization previously explained.

- **11. Final calculations.**

  Once all the physical variables fields have been completely determined, it may be necessary in some cases to calculate parameters like Nusselt number, aerodynamic coefficients, etc...

- **12.1. Checking of stop criteria.**

  In every time step it is needed to check if stopping criteria has been achieved or not.

- **12.1. Results keeping for postprocessing.**

  Depending on the postprocessing study type, it is necessary to save some data or parameters from the simulation.

- **13. Postprocessing.**

  Study and analysis of the obtained results during the simulation.

3.3 LID Driven Cavity

In this section are presented the obtained results in the simulation of the case LID Driven Cavity. Additionally, it is presented the verification and a detailed explanation of the phenomena involved in the studied problem.

The scheme of the case has already been presented in section 3.1.3. It consists on a square cavity with a parallel flow on its upper part. However, before showing all the obtained results, it is important to explain the influence of the simulation main parameter: the Reynolds number.

This has already been presented in section 2.3. It represents the ratio between the inertial and viscous forces.

$$Re = \frac{\rho U_{Ref} L_{Ref}}{\mu}$$

As there can be seen on its mathematical expression, at low Reynolds numbers (high viscosity in front of inertial forces), the viscosity effects dominate the flow behaviour. On the other hand, an increasing Reynolds makes the inertial forces to play a more significant role on the flow.

This physical phenomena will be perfectly observable in the simulation results as the Reynolds number increases.

Since the problem density (ρ), velocity (U_{Ref}) and reference length (L_{Ref}) are fixed parameters due to boundary or geometric conditions, the variable modification because of the Reynolds number is the dynamic viscosity (μ).

In addition, there is one important aspect that hasn't been mentioned yet about Reynolds number. It defines if the flow regime is laminar or turbulent. The limit between both differ from one problem to another depending mainly on its characteristics and boundary conditions. In this case, frontier between both regimes is approximately Reynolds 10000. All the simulations of LID Driven Cavity above this value belong to turbulent flow studies. Therefore, since the approach of this case is completely laminar, the maximum Reynolds number simulated has been 7500.

Since there have been carried out up to 6 different Reynolds number simulations, there is no need to present all their results and verification in this report, but only the most significant of them. However, the simulations not exposed in this document can be found in appendix B in Annex document of this project.

3.3.1 Obtained results and verification

First of all, it is necessary to present the simulation parameters for each of them carried out (table 3.2).

Table 3.2: LID Driven Cavity Simulation parameters

Reynolds	**100**	**7500**
L_{Ref} $[m]$	1.0	1.0
ρ $[Kg/m^3]$	1.0	1.0
X Direction Nodes	100	250
Y Direction Nodes	100	180
X Nodal Distribution	Regular	Hyp. Tang.
Y Nodal Distribution	Regular	Sine
Hyp. Tan. Stretching	-	1.5
Stop Criteria	1,0E-06	1,0E-06
Convective scheme	CDS	CDS

Verification.

Once a CFD simulation has been completed, one of the most important tasks to do is to verify the obtained results. This step must be done using trustworthy scientific sources. For this project, there has been chosen to compare obtained results with the ones presented in [25].

In this case, the verification has been done by comparing 3 different variables of the results for every simulation carried out. These are the horizontal velocity along the vertical line of cavity's centre U(y) (figure 3.37), the vertical velocity along the horizontal line at the centre V(x) (figure 3.37), and the distance between the centre of the cavity and the centre of the main flow vortex.

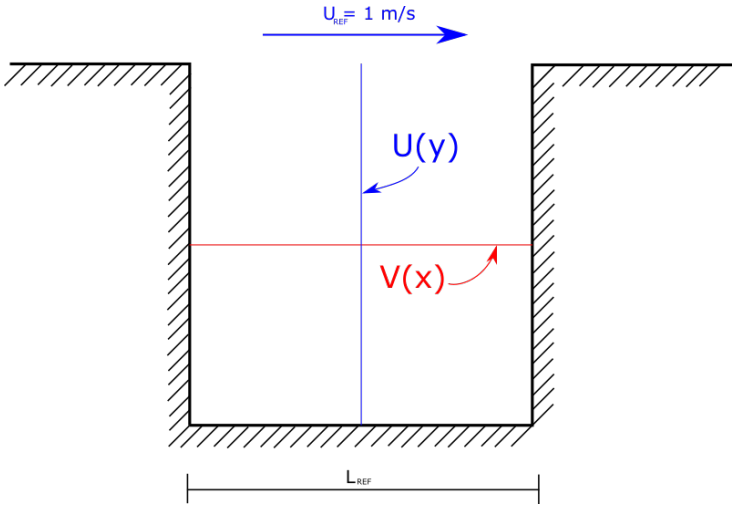

Figure 3.37: LID Driven Cavity velocity verification scheme

Next up are presented the velocities verification for Reynolds 100 and 7500.

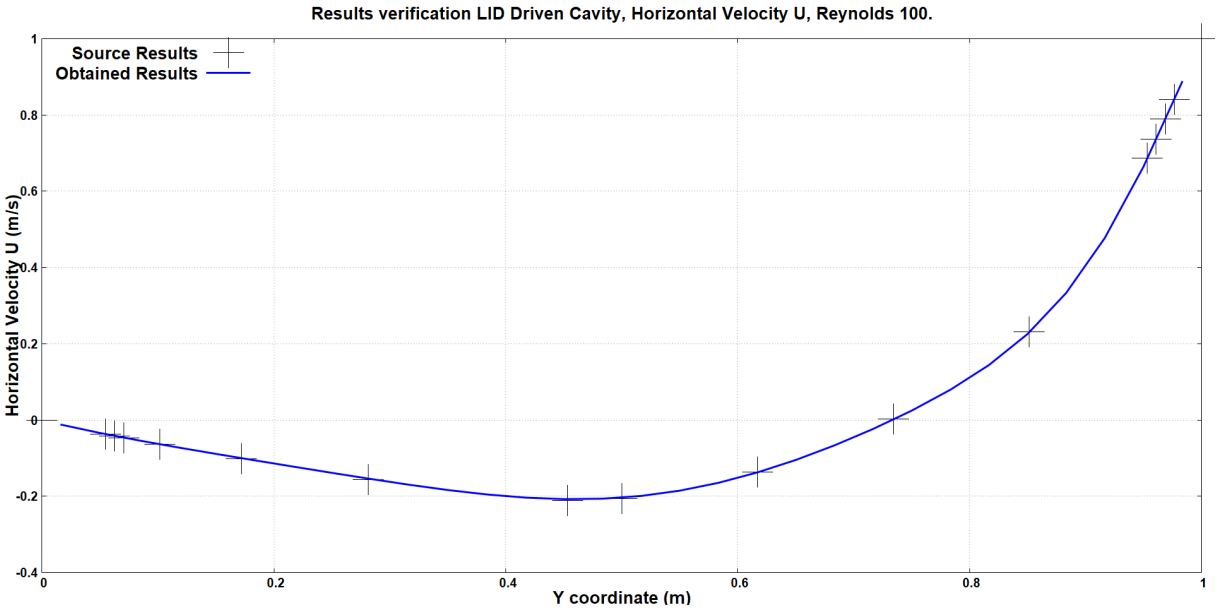

Figure 3.38: LID Driven Cavity Horizontal Velocity U(y) verification for Reynolds 100

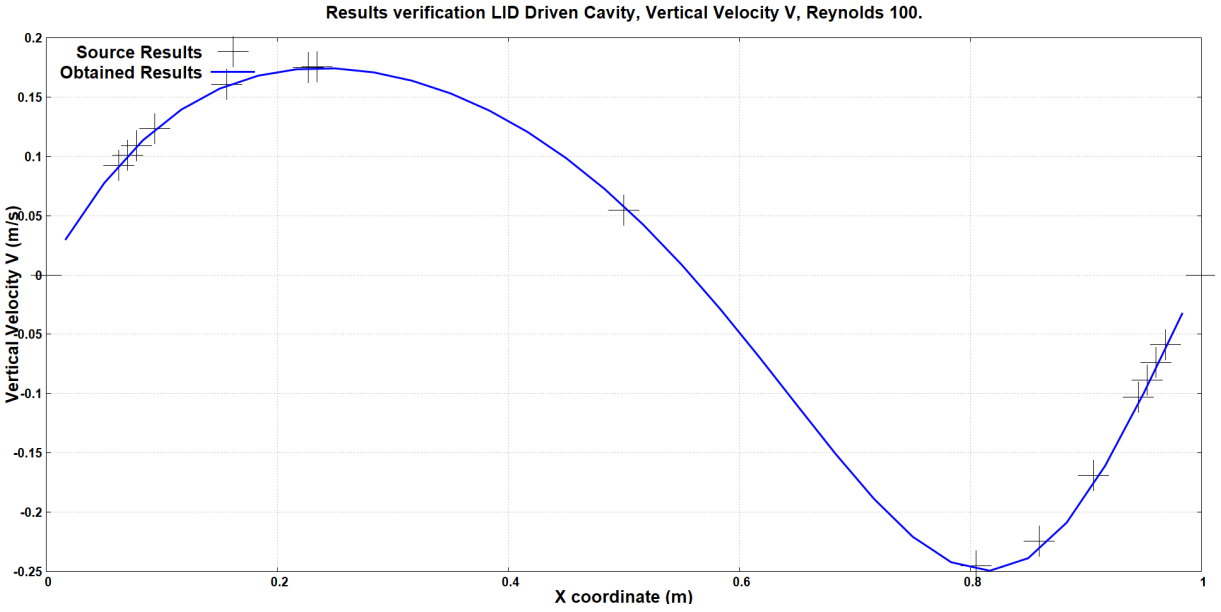

Figure 3.39: LID Driven Cavity Vertical Velocity V(x) verification for Reynolds 100

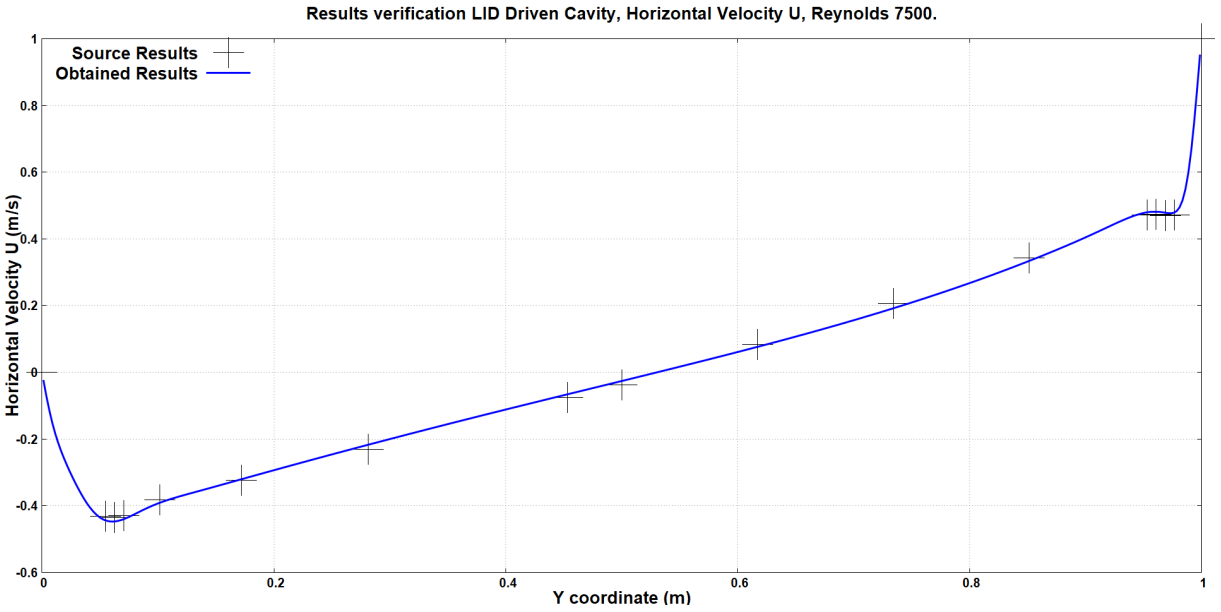

Figure 3.40: LID Driven Cavity Horizontal Velocity U(y) verification for Reynolds 7500

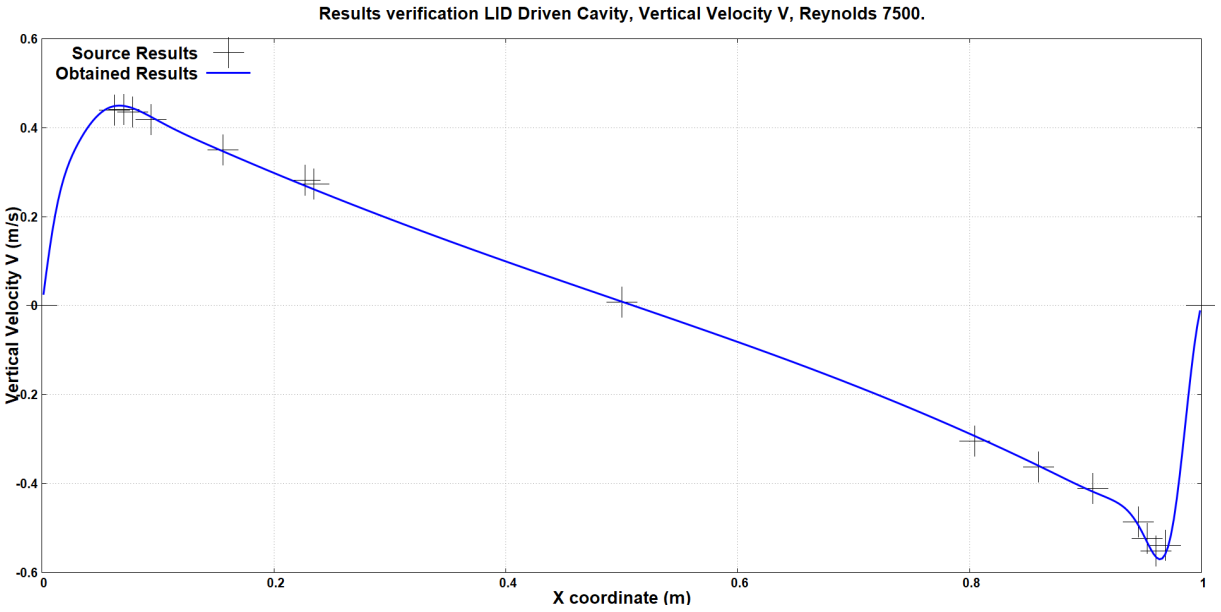

Figure 3.41: LID Driven Cavity Vertical Velocity V(x) verification for Reynolds 7500

As there can be seen in figures 3.38, 3.39, 3.40 and 3.41, the accuracy of the obtained results in comparison with the scientific source ones is more than acceptable. The nodal density, alongside with the numerical scheme chosen for both of the simulations have proven to be a great choice.

Not only they have been able to replicate almost perfectly the results from the scientific publication, but in case of the Reynolds 7500 simulation, the nodal distribution selected has allowed to complete the simulation in a relatively low computational time.

It also needs to be remarked that there are many different factors that make impossible to obtained the same mathematically results. The author may have been used a different numerical

scheme, nodal density or distribution, etc..

However, in what comes of velocities verification, it can be stated that the results for simulations between both Reynolds can be considered acceptable.

Finally, although it isn't essential to verify the results since velocities are already proven to be correct, it is also presented in table 3.3 the distance between centre of the cavity and centre of the main vortex.

Table 3.3: LID Driven Cavity main vortex distance from the centre of the cavity

Reynolds	Obtained Results (m)	Ghia, U. Results (m)	Relative Error (%)
100	0,2653	0,2621	1,3430
400	0,1208	0,1188	1,8519
1000	0,0724	0,0699	3,9342
3200	0,0442	0,0497	12,1730
5000	0,0385	0,0371	4,1509
7500	0,0347	0,0343	1,2828

Once again, the obtained results match almost perfectly with the ones from the scientific source. There are 2 or 3 different Reynolds simulations that may not be as accurate as the other ones (Reynolds 1000, 3200 and 5000). This happens because of several facts. First of them, it isn't easy to find the exact location of the main vortex centre. It is necessary to make several sweeps though many central control volumes to see which of them has exactly null or almost null speed on both axis. Therefore the results may vary slightly.

In addition to that, this scale of accuracy are severely affected by the simulation parameters on this project's codes and author's ones, alongside the spatial discretization chosen.

However, although every result presented in this verification section has a relative error, in CFD problems are considered as acceptable up to a 10% or 15% of it. Therefore, all LID Driven Cavity results exposed in this thesis are confirmed to be correct.

Results.

Once the obtained results have been verified and can be considered as correct, they can be deeply analysed and explained.

Velocity fields.

In figures 3.42 and 3.43 are presented the velocity fields for Reynolds 100 and 7500. There has been chosen to expose this two values to give a better insight of the flow behaviour dependence of this parameter. In order to see the whole evolution through the rest of the simulations done, go to appendix B in Annex document.

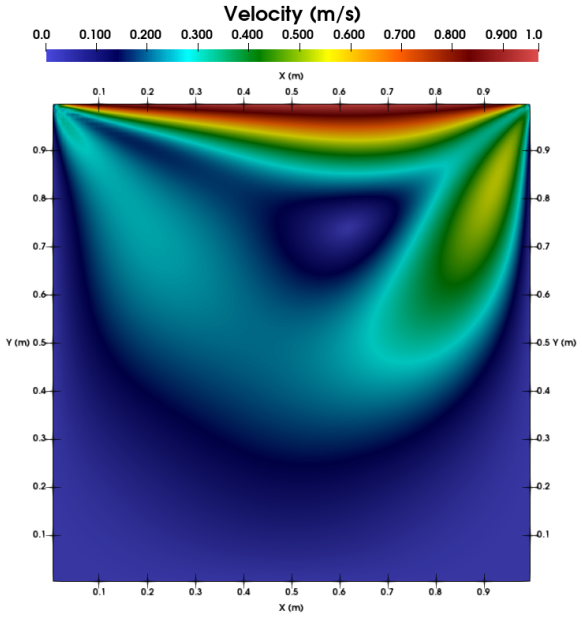

Figure 3.42: LID Driven Cavity Velocity Magnitude field Reynolds 100

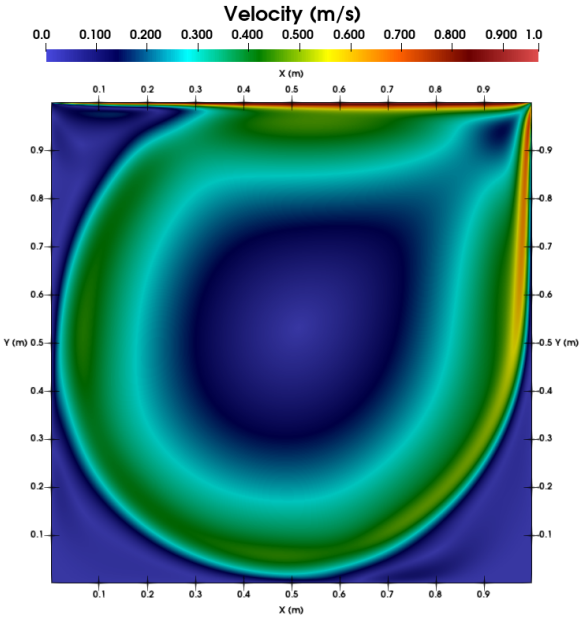

Figure 3.43: LID Driven Cavity Velocity Magnitude field Reynolds 7500

In what comes to velocity, the changes are pretty clear. In case of Reynolds 100, the viscosity effects dominate over the inertial forces, avoiding the flow to reach the lower parts of the cavity and reducing dramatically its velocity. This phenomena can be clearly appreciated looking at the right side of figures 3.42 and 3.43.

In both of them, the upper part velocity remains similar, the boundary condition imposes this. However, when approaching the right wall, it can be observed the severely reduction in flow velocity at Reynolds 100 in front of Reynolds 7500.

This happens because, the lower the Reynolds is, the higher the dynamic viscosity. This makes latter effects to play a more significant role on flow's speed when approaching a solid wall. Therefore, the fluid lost much of its velocity due to viscous effects and doesn't have enough speed to reach the lower parts of the cavity.

On the other hand, having a Reynolds 7500 means to have a much lower dynamic viscosity. The effect of this can be observed at the flow field. The fluid doesn't lose much of its velocity due to viscous dissipation effects. And so it is capable of not only reaching the lower parts of the cavity, but also approaching the left solid wall and not stopping there, like in the first case on the right wall.

This phenomena can also be appreciated in figures 3.38, 3.39, 3.40 and 3.41. For instance, in case of the horizontal velocity there can be clearly stated the huge difference on the velocity at the lower part of the cavity ($Y << L_{Ref}$). Both two simulations have non-slip condition at the wall (U = 0). However in Reynolds 7500 case, the flow is able to reach this part with a much higher speed. And so this happens similarly for the vertical velocity at the centre line.

This is the perfect example of the definition of the Reynolds number, the ratio between inertial forces and viscosity. The lower it is, the bigger role viscous effects play on the flow, slowing

it and dissipating most of its kinetic energy. Meanwhile, a higher Reynolds prove to reduce viscous dissipation effects in front of inertial forces, keeping the flow with most of its initial kinetic energy and so its velocity.

Streamlines fields.

Additionally, it is important to present the Streamlines fields for this two simulation cases.

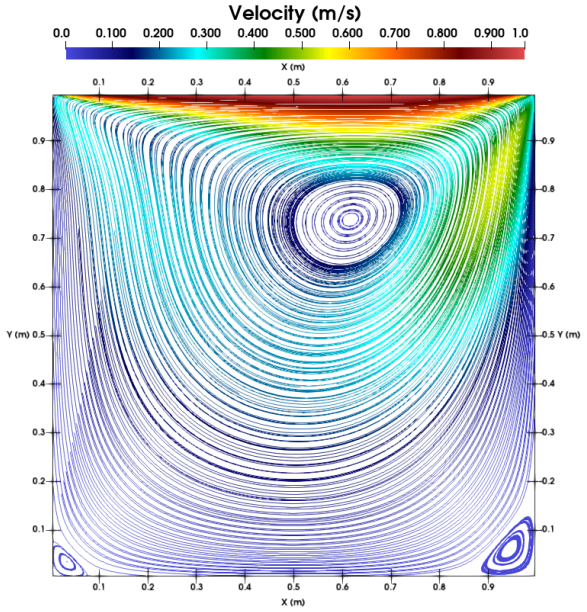

Figure 3.44: LID Driven Cavity Streamlines field for Reynolds 100

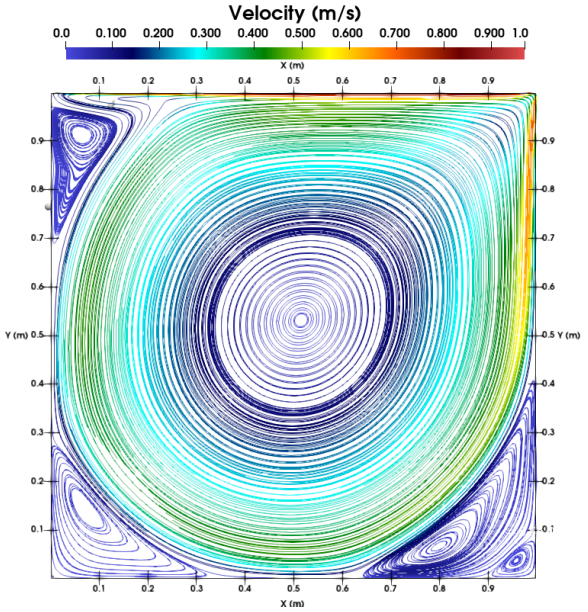

Figure 3.45: LID Driven Cavity Streamlines field for Reynolds 7500

As in the velocity fields case, here there can be seen again the enormous effect Reynolds number represent in flow's behaviour. There are two important aspects to mention in the streamlines comparison.

First of them is referred to the main vortex centre location. As can be seen in the verification section in table 3.3, the higher the Reynolds number is, the closer the vortex is from the centre of the cavity. This phenomena doesn't have any different explanation but the one aforementioned. A low Reynolds dissipates much more fluid's kinetic energy, avoiding the flow to reach lower parts of the cavity, and so the centre of the vortex is closer to the upper part (figure 3.44). Meanwhile, higher Reynolds number makes inertial forces to play a bigger role and the fluid reaches all parts of the cavity getting the vortex closer to the centre (figure 3.45).

The other important aspect is, as it can be observed in figures 3.44 and 3.45, the minor vortexes formation. The higher Reynolds, the higher number of minor vortexes and the bigger these are.

At low Reynolds, not only the fluid arrives to the corners with much less kinetic energy, but also it is dominated by the viscous effects, which immediately slow down the fluid avoiding vortexes generation.

On the other hand, the reduction of the viscosity role on the flow (higher Reynolds) allows the fluid to achieve corners of the cavity with enough energy to not only generate vortexes, but also sub-vortexes, like right lower corner in figure 3.45.

To see the evolution of the vortex generation through different Reynolds number, go to appendix B in Annex document of the project.

Pressure fields.

Finally, in this results section for the LID Driven Cavity, it is presented the relative pressure fields for the simulations of Reynolds 100 and 7500.

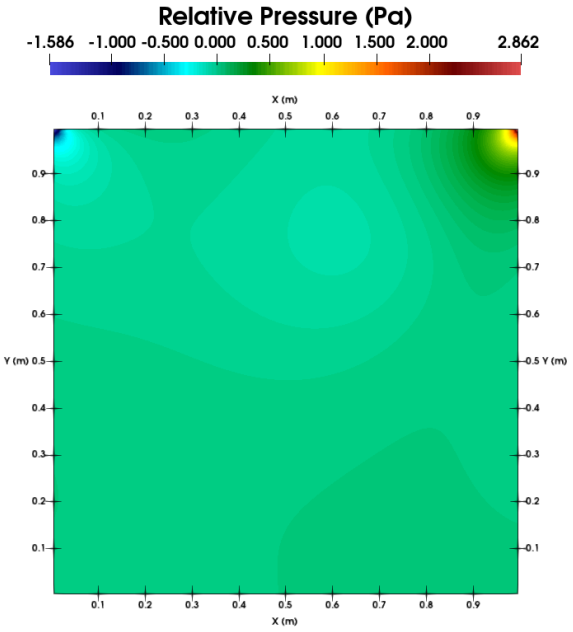

Figure 3.46: LID Driven Cavity Relative Pressure field Reynolds 100

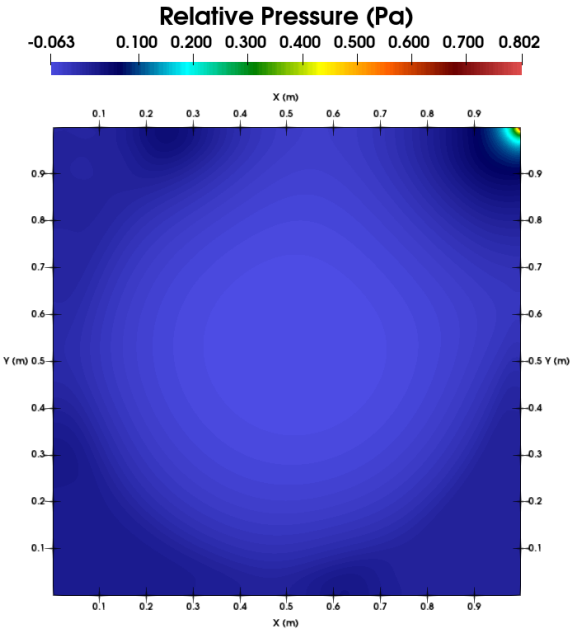

Figure 3.47: LID Driven Cavity Relative Pressure field Reynolds 7500

Before analysing the simulation pressure results, it is important to present Bernouilli's Principle.

In every fluid there is a inverse proportionality between its velocity and its pressure.

$$\frac{\mathbf{u}^2}{2} + gz + \frac{P}{\rho} = Constant \tag{3.77}$$

The equality shown in expression (3.77) can be applied on every flow. Assuming a constant gravity and height value "z" (potential energy), if the velocity goes down, the pressure increases and vice versa, but always keeping the relation in previous equation.

This phenomena can be clearly observed in figures 3.46 and 3.47. At Reynolds 100 (figure 3.46), the velocity modulo drops down at the upper part of the right wall. Then, applying Bernouilli's Principal, the pressure should increase, which is exactly what it does. Meanwhile, as there can be seen in Reynolds 7500 pressure field (figure 3.47), the pressure rise is much lower than on the other case (0.8 Pa and 2.9 Pa respectively).

This has no other explanation but the one provided while showing velocity results. Due to increasing Reynolds, flow's kinetic energy (speed) are not as dissipated as in Reynolds 100 case, so the pressure doesn't increase as in the first figure.

In addition, looking at the left corner of the upper part proves the same fact. At low Reynolds, the flow comes from below that part with not so much velocity. Then, when it arrives to it, the inlet flow from the upper part accelerates it dramatically, and so the pressure drops severely.

On the other hand, the higher Reynolds number is, the lower the velocity change is at that part of the cavity, and so the pressure drop due to the flow acceleration.

3.4 LID Differentially Heated

In this section the results obtained in the simulations of the LID Differentially Heated case are presented. Alongside with these, there will also be presented the verification and a deeply explanation of the physical phenomena of the problem.

LID Differentially Heated theoretical basis and scheme have already been presented in section 3.1.3. It consists on a closed square cavity with 2 adiabatic walls and the other ones with different temperatures.

When the fluid approaches to the heated wall, it heats up and due to buoyancy (Boussinesq approximation hypothesis, section 3.1.1) goes up until it looses that energy while getting closer to the cold wall. This phenomena is clearly observable in figure 3.3 in section 3.1.3.

There are many different configurations for this case depending on the distribution of the boundary conditions. For this project, there has been chosen to set as adiabatic the upper and lower walls. And so the left and right ones with a temperature difference between them. Being higher left side's one.

However, choosing the same adiabatic configuration and setting right wall's temperature higher would give the same numeric results but mirrored physical properties fields. Another option is to make left and right walls adiabatic and the upper one to have a higher temperature than the lower side.

In this 3 mentioned configurations, the system is able to reach a steady state after enough time (if the Rayleigh is still in the laminar regime). Nevertheless, setting as adiabatic walls left and right ones and having a higher temperature the lower part than the upper one, the fluid would be continuously changing.

In this case, it is impossible to arrive to an steady state. The fluid near the ground heats up and goes up until it looses too much energy and then falls down. This process is repeated again and again, and the system is continuously oscillating in what is called as a Periodic state.

However, this study case is far away from this project's scope for laminar regime. Only the first case of the 4 mentioned has been simulated.

LID Differentially Heated problem has two great differences with the other 2 cases developed in laminar regime part of this project.

First of them is related with the equations resolution. It is the only case in which temperature plays a role. This means that, unlike in the other two, in this problem it is necessary to solve the Navier-Stokes Energy Conservation equation (apart from the other ones). Its numerical discretization for the case can be found in section 3.2.4.

The other main difference is related to non-dimensional numbers. In LID Driven Cavity and Square Cylinder cases, the parameter controlling flow's behaviour is the Reynolds number. However, in this problem there are two different variables to do that, Prandtl and Rayleigh numbers.

Their theoretical basis is already explained in section 2.3. Nevertheless, there are some aspects that still needs to be define.

The Rayleigh number definition allows to calculate the dynamics viscosity of the problem (μ). The rest of the variables are already defined by the problem boundary conditions or by its geometry.

$$Ra = \frac{\rho g \beta \Delta T L_{Ref}^3}{\alpha \mu}$$

Additionally, in the simulations, it is considered that the fluid inside the cavity is air. Due to this, Prandtl number has to be set to 0.71 compulsory. It is exactly the relationship that exists between its variables for air at ambient temperature.

$$Pr = \frac{C_p \mu}{K} = 0.71$$

Additionally, the C_P is set to 1000.0 J/KgK, to simulate air at ambient conditions.

This parameter setting allows to fix the thermal conductivity (K) to simulate exactly the behaviour of air in these conditions.

There is no reason for talking about Prandtl number as a frontier between the laminar and turbulent flow regime. This is controlled by the Rayleigh.

For the chosen boundary conditions and geometry, the limit is approximately 1.0E6 for Ra. Above this value, the system is unable to achieve a steady state because of the turbulence generated.

Due to this fact, all simulations shown are below or equal to this limit.

In this report, there are presented the cases of Rayleigh 1E3 and 1E6. These are the lowest and higher Rayleigh numbers simulated, in order to give a better insight of the variation and changes this parameter makes on the flow. To see the whole evolution and the rest of the simulations carried out, go to appendix C in Annex document of this project.

3.4.1 Obtained results and verification

Next up, in table 3.4, are presented the simulation parameters for LID Differentially Heated cases presented in the report.

Table 3.4: LID Differentially Heated simulation parameters

Rayleigh	**1.0E3**	**1.0E6**
L_{Ref} $[m]$	1.0	1.0
ρ $[Kg/m^3]$	1.0	1.0
g $[m/s^2]$	-9.81	-9.81
T_{Left} $[K]$	1.0	1.0
T_{Right} $[K]$	0.0	0.0
X Direction Nodes	100	180
Y Direction Nodes	100	180
X Nodal Distribution	Regular	Hyp. Tang.
Y Nodal Distribution	Regular	Hyp. Tang.
Hyp. Tan. Stretching	-	1.4
Stop Criteria	1.0E-6	1.0E-6
Convective scheme	CDS	CDS

Verification.

For the verification of the LID Diferentially Heated obtained results, there has been chosen to use as trustworthy scientific source [26]. In the publication, the authors, N.C. Markatos and K. A. Pericleous, use another scientific source as well [27], written by G. de Vahl Davis.

The variables compared in the verification process are the minimum, mean and maximum Nusselt number on the left wall. And the maximum horizontal and vertical velocities in the central vertical and horizontal lines respectively. Additionally, the vertical or horizontal coordinate of these variables is also verified.

Nusselt number has already been presented in section 2.3. It is a non-dimensional variable that quantifies the heat transfer from the heated all to the fluid, right in flow's boundary layer.

$$Nu_Y = \frac{\partial T}{\partial x}|_{x=0} \cdot \frac{L_{ref}}{T_w - T_\infty} \tag{3.78}$$

Since there has been selected in the boundary conditions that the heated wall is the left one, all Nusselt number calculations have been done at this.

In order to apply previous mathematical expression to the discrete values in the domain, it is necessary to transform it into the following equation.

$$Nu_Y = \frac{T_{Left} - T_{i=1}}{\Delta X_{i=1}} \cdot \frac{L_{Ref}}{T_{Left} - T_{Right}} \tag{3.79}$$

As there can be seen in previous expression, in order to compute the temperature gradient at the left wall, it is necessary to take the value of the first node in the horizontal direction ($T_{i=1}$).

Additionally, to make the resulting number non-dimensional, it is needed to multiply the mentioned gradient by the second term of the equation (3.79).

Then, the only step after these is to compute the mean Nusselt ($\overline{Nu}$) and find the maximum and the minimum of them and their respective location at the left wall.

These results are presented next up, in tables 3.5 and 3.6, alongside with the results from the chosen scientific source.

Table 3.5: LID Differentially Heated Rayleigh 1.0E3 Simulation Nusselt results

Parameters	Obtained Results	M. and P. Results	Vahl Davis Results
$\overline{Nu}$	1.103	1.108	1.118
Nu_{max}	1.470	1.496	1.505
Y Coord. (Nu_{max}) **(m)**	0.095	0.083	0.092
Nu_{min}	0.699	0.720	0.692
Y Coord. (Nu_{min}) **(m)**	0.995	0.993	1.000

Table 3.6: LID Differentially Heated Rayleigh 1.0E6 Simulation Nusselt results

Parameters	Obtained Results	M. and P. Results	Vahl Davis Results
$\overline{Nu}$	8.924	8.754	8.799
Nu_{max}	18.321	17,872	17.925
Y Coord. (Nu_{max}) **(m)**	0.035	0.0375	0.0378
Nu_{min}	0.973	1.232	0.989
Y Coord. (Nu_{min}) **(m)**	0.995	0.9925	1.000

As there can be clearly observed in tables 3.5 and 3.6, the higher the Rayleigh, the higher the Nusselt. Latter depends on the temperature gradient right at the heated wall, where the fluid gets its temperature from.

A higher gradient means more heat transfer between the wall and the fluid. Which is exactly what an increase in Rayleigh number represents. It is completely bonded with the total amount of heat that is being transfered from a solid to a fluid.

Both simulations presented are in the laminar convection range. Nevertheless, there can be observed the severely change in heat transfer between them by just looking at the mean Nusselts obtained.

In what comes to the accuracy of the results there are several aspects that need to be mentioned.

First of them is that, these Nusselt values depend enormously on the nodal density and resolution near the walls. This is why there was chosen to use a Hyperbolic Tangent distribution. And, as there can be seen, obtained results match almost perfectly with the ones from the reference authors. Even in some cases being between both of authors' results, which gives even more credit to the accuracy.

Secondly, there must be pointed out that, the coordinates values are totally dependant on the mesh distribution and may differ from the reference. However, as there can be clearly seen, obtained coordinates for the maximum and minimum Nusselt numbers have a more than acceptable accuracy when comparing them with the authors' results.

The other parameters analysed to complete the LID Differentailly Heated verification are the maximum velocities at the centre lines of the cavity. More precisely, these are the maximum horizontal speed (U_{max}) at the vertical centre line and the maximum vertical velocity (V_{max}) at the horizontal centre line.

These results are presented next up in tables 3.7 and 3.8, alongside with the results obtained from the reference authors selected.

Table 3.7: LID Differentially Heated Rayleigh 1.0E6 Simulation Velocities results

Parameters	Obtained Results	M. and P. Results	Vahl Davis Results
U_{max}	3.691	3.544	3.649
Y Coord. (U_{max}) (m)	0.815	0.832	0.813
V_{max}	3.731	3.593	3.697
X Coord. (V_{max}) (m)	0.175	0.168	0.178

Table 3.8: LID Differentially Heated Rayleigh 1.0E6 Simulation Velocities results

Parameters	Obtained Results	M. and P. Results	Vahl Davis Results
U_{max}	65.151	68.810	64.630
Y Coord. (U_{max}) (m)	0.855	0.872	0.850
V_{max}	220.952	221.800	217.360
X Coord. (V_{max}) (m)	0.035	0.0375	0.0379

First of all it is important to mention that, the shown values for the velocities in previous tables are not exactly in velocity units. Therefore, in Rayleigh 1.0E6, there would be impossible to consider the fluid as incompressible, since that speed values are way beyond established limit (Mach = 0.3).

These velocities values have been obtained using the following transformation.

$$U' = U \cdot \frac{L_{Ref}}{K} \tag{3.80}$$

In this project, this expression has been only applied to obtain results that can be compared with the ones from the verification source. However, the author uses them to link these velocity values with the dimensions of the geometry and non-dimensional numbers controlling flow's behaviour.

Again, as there can be clearly observed looking at tables 3.7 and 3.8, obtained results match in a great way. Even in some cases, being this project results between both authors' values. The same can be applied for the coordinates obtained for every maximum or minimum velocity.

With these and the former Nusselt parameter verification, it can be firmly stated that the obtained results for the LID Differentially Heated case simulations can be considered as correct.

Next up will be presented the obtained results of velocity, streamlines and temperature fields for the simulations of Rayleigh 1.0E3 and 1.0E6. These are the lowest and the highest Rayleigh simulated, in order to give a better view of the changes this parameter produces in flow's behaviour. To see the flow evolution between these two values, go to appendix C in Annex document of this project.

Results.

Temperature fields.

In figures 3.48 and 3.49 are presented the temperatures fields obtained in the simulations of Rayleigh 1.0E3 and 1.0E6.

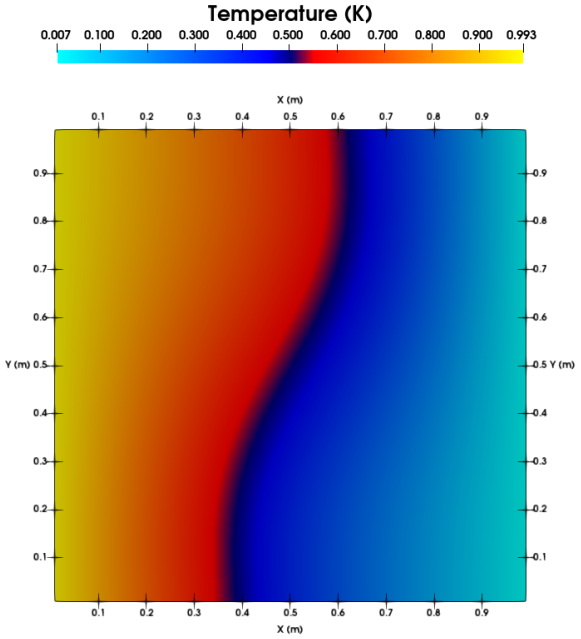

Figure 3.48: LID Differentially Heated Temperatures field Rayleigh 1.0E3

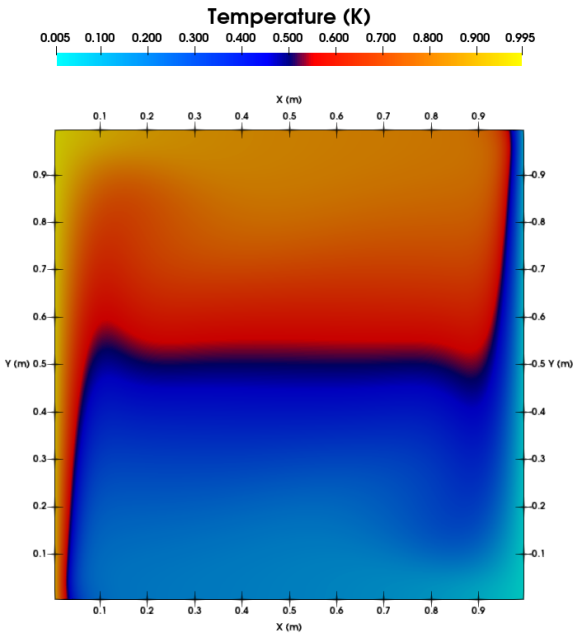

Figure 3.49: LID Differentially Heated Temperatures field Rayleigh 1.0E6

LID Differentially Heated is the only laminar case of this project in which the temperatures field is significantly relevant. Due to the presence of the buoyancy term (Boussinesq approximation), the fluid's temperature plays a huge role on its behaviour in the flow. That's why this is the only case in which temperatures field is presented.

In what comes to the obtained results for the temperature, there are several aspects that need to be mention.

First of them, as it was clearly expected, the higher temperatures takes place near the heated wall. The cold fluid approaches it from the lower part, heats up due to convection and conduction transfer and then it is capable of overcome the gravity effect. When it is located at the top

of the cavity, it approaches the cold wall, where looses most of its temperature, going back to the beginning of the loop.

Looking at both images, there can be clearly observed the influence the Rayleigh number has on the flow. In the first case (figure 3.48), the fluid heat transfer takes place at a much slower rate. It takes the flow on the lower part almost half of the cavity distance to heat up from 20% to 80% of left wall's temperature. Here it can be observed the great impact Rayleigh has on fluid conduction heat transfer.

On the other hand, looking at figure 3.49, it is appreciated an incredible increasing in convective and conduction heat transfer. In this case, the fluid is able to heat up in a tiny distance from the wall. As there can be seen, it changes its temperature from about 20% to 80 or 90% of left wall's temperature in just a tiny distance near the wall. In addition to that, the flow is able to maintain this temperature during much more time while approaching the right cold wall.

There is such difference between both conduction heat transfer values that, in the first case (figure 3.48), the flow reaches an steady state more or less with the same temperatures field as the walls temperature distribution. Meanwhile, at Rayleigh 1.0E6 (figure 3.49), the flow reaches an steady state in which there are only two thin boundary layers at the walls and a very differentiated temperatures areas at the lower and upper part of the cavity.

Velocity fields.

Next up in figures 3.50 and 3.51 are presented the velocity fields obtained in the simulations of Rayleigh 1.0E3 and 1.0E6.

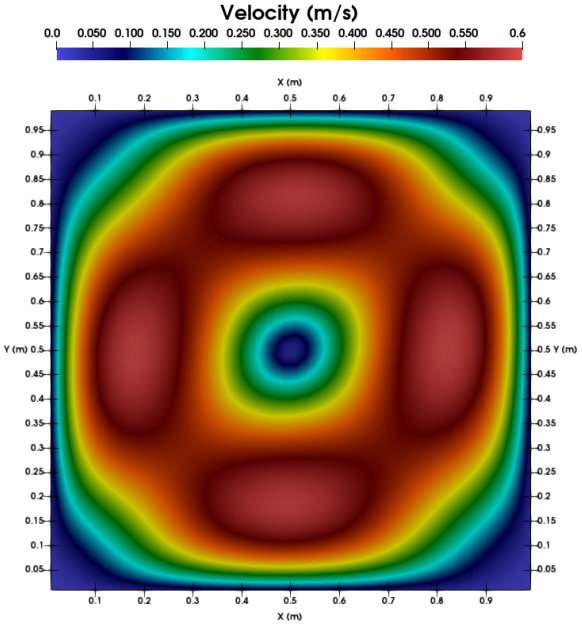

Figure 3.50: LID Differentially Heated Velocity Magnitude field Rayleigh 1.0E3

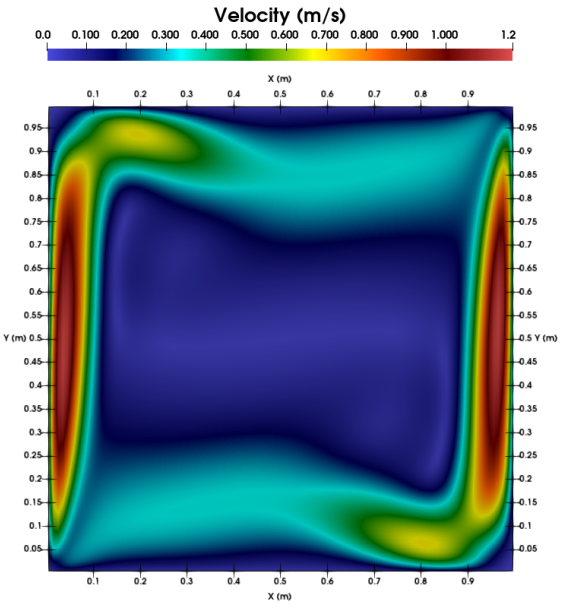

Figure 3.51: LID Differentially Heated Velocity Magnitude field Rayleigh 1.0E6

The velocity fields for every Rayleigh simulated is a consequence of the previous temperatures fields.

In the first case (figure 3.50), the heat transfer doesn't play a big role in the overall contribution to fluid's velocity. However, thanks to the buoyancy term, the flow travels the movement described before. When approaching the heated wall, the buoyancy term begins to overcome the gravity effects. Then, when it reaches the top, due to boundary conditions, goes towards the right wall and looses its heat and so gravity play a bigger role than buoyancy and falls down.

On the other case (figure 3.51), the heat transfer at the left wall takes places at a so tiny distance and time that the buoyancy term rapidly overcome gravity increasing its speed in the vertical direction. This allows to the generation of a boundary layer at both walls. In case of right one, it happens when the fluid looses so quickly all its temperature and falls down.

However, there are two areas in the cavity in which although the fluid is in the heated area, it falls down, and vice versa for the cold one. This happens due to the fast heat transfer that takes place at that areas. These zones are right in the middle between both temperature regions and so it is constantly heating up and then cooling down.

Streamlines fields.

Finally, in figures 3.52 and 3.53 are presented the Streamlines fields for the Rayleigh 1.0E3 and 1.0E6 simulations carried out.

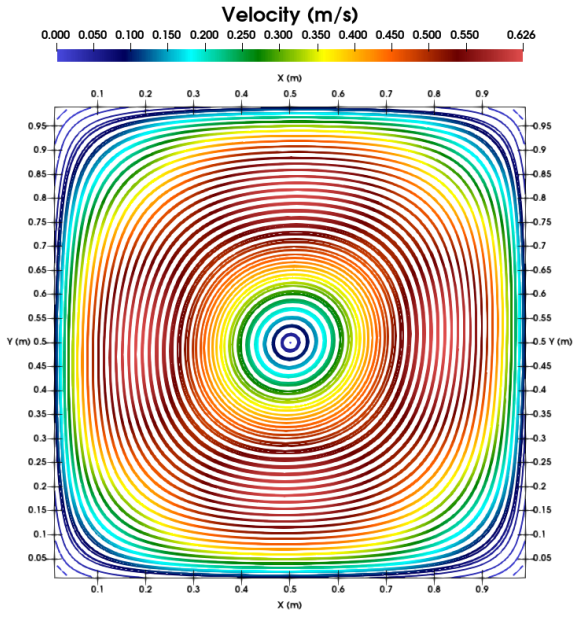

Figure 3.52: LID Differentially Heated Streamlines field Rayleigh 1.0E3

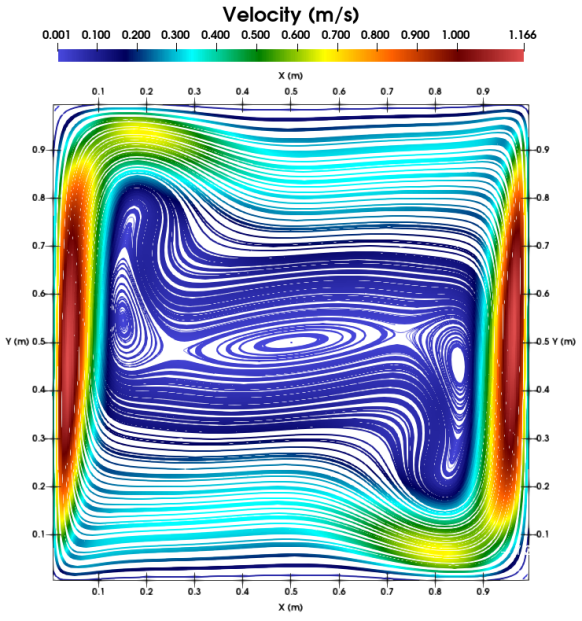

Figure 3.53: LID Differentially Heated Streamlines field Rayleigh 1.0E6

In the streamlines fields in figures 3.52 and 3.53 there can be seen what has been already mentioned in velocities ones.

In the first case (figure 3.52), a huge vortex in the middle of the cavity is observed. This has been generated due to the loop process on the fluid's travel through the cavity going up and down at the left and right walls respectively.

However, at Rayleigh 1.0E6 (figure 3.53), the phenomena described for the velocities field can

be much clearly observed. The fluid's heat transfer takes place so fast and in a so tiny area that it is capable of generating little steady vortexes due to this movement.

As there can be noticed, in LID Differentially Heated case the pressure fields obtained in the simulationshaven't been presented. Due to the importance of the temperature and heat transfer in the problem, there has been chosen not to expose the pressure results. These are considered to be not enough relevant in flow's behaviour to add them to the report. Markatos and Pericleous and Vahl Davis don't even include pressure results to compare with.

As in the other two cases for the laminar regime, the rest of simulations properties fields that haven't been shown here can be found in appendix C of Annex Document of this project.

3.5 Square Cylinder

In this section are presented the results obtained in the simulations of flow past a square cylinder. As in the previous LID Driven Cavity and LID Differentially Heated cases, here will also be presented the verification and explanation of the physical phenomena involving the problem.

The Square Cylinder theoretical background has already been exposed in section 3.1.3. It consists on a channel with a parabolic profile inlet in which there is a square cylinder.

As in LID Driven Cavity case, the main parameter that controls the behaviour of the fluid is the Reynolds number. However, there are some slightly modifications around this variable in this problem.

$$Re = \frac{\rho U_{Ref} L_{Ref}}{\mu}$$

In section 3.3, there can be seen for instance that, the reference length for the non-dimensional number (L_{Ref}) corresponds to the cavity length/height. Nevertheless, in this case, the reference is the length/height of the interior square, not the channel (figure 3.54).

Moreover, in LID Driven Cavity problem, the reference velocity was pretty clear to be exactly the inlet speed. However, Square Cylinder boundary conditions imposes a parabolic inlet profile (figure 3.54). This means there are different options as a reference velocity. In this project, there has been chosen to set as reference velocity the mean value of the inlet.

$$\overline{U} = \frac{U_{max}}{\sqrt{2.0}}$$

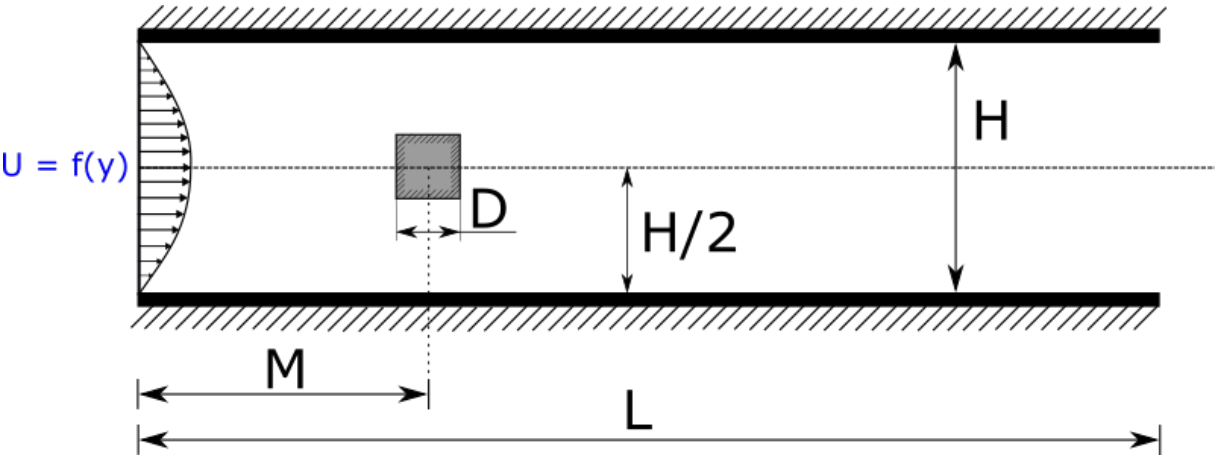

Figure 3.54: Square Cylinder geometry parameters definition

Therefore, the Reynolds number for the Square Cylinder study case can be expressed as following.

$$Re = \frac{\rho U_{max} D}{\mu \sqrt{2.0}} \tag{3.81}$$

The following geometry parameters (table 3.9) have been selected for all the simulations done.

Table 3.9: Square Cylinder geometry parameters selected for the simulations

Parameter	Value (m)
D	1.0
M	12.5
L	50.0
H	8.0

Again, as in the LID Driven Cavity problem, the modified parameter depending on the Reynolds is the dynamics viscosity.

However, the biggest change from that case, or even LID Differentially Heated, to this one has already been slightly mentioned while presenting the case in section 3.1.3.

LID Driven Cavity and LID Differentially Heated cases simulations always arrive to an steady state in which the variables values remain constant. This situation may happen sooner or later depending on the simulation condition, Reynolds or Rayleigh numbers, etc...

However, in Square Cylinder problem, once a certain *Critical* Reynolds number has been exceeded, the system begins to oscillate by generating vortexes behind the cylinder. These are also known as $Von-Kárman\ Vortexes$.

Due to these, the system is unable to achieve an steady state. Nevertheless, once the oscillations have stabilised around a certain value, it is called as ”Periodic State”.

Normally, in a non-oscillatory system, the cylinder would experiment a constant drag horizontal force because of the flow. But, due to the oscillations, this isn’t a fixed value, it begins to swing around a certain value. Moreover, a lift oscillating force appears too.

As there has been proven in the simulation, alongside with the scientific sources, the mentioned Critical Reynolds number is approximate to 70. In this report will be only presented and explained the results for Reynolds 5 and Reynolds 200 (the lowest and highest Reynolds simulations done). In order to see the results from all the other simulation carried out go to appendix D in Annex document of this project.

3.5.1 Obtained results and verification

As in previous LID Driven Cavity and Differentially Heated cases, main simulation parameters are presented.

Table 3.10: Square Cylinder Simulation parameters

Reynolds	**5**	**200**
ρ $[Kg/m^3]$	1.0	1.0
U_{max} $[m/s]$	1.0	1.0
X Direction Nodes	243	450
Y Direction Nodes	178	236
Stop Criteria	1,0E-06	-
Convective scheme	QUICK	QUICK

In order to give a better insight and an easier explanation of the verification parameters, these are presented alongside the obtained results for the case.

Verification and results.

Velocity fields.

In figures 3.55 and 3.56 are presented the velocity fields obtained in the simulations of Reynolds 5 and 200. These two have been selected in order to ease the understanding of the oscillation phenomena involving the case.

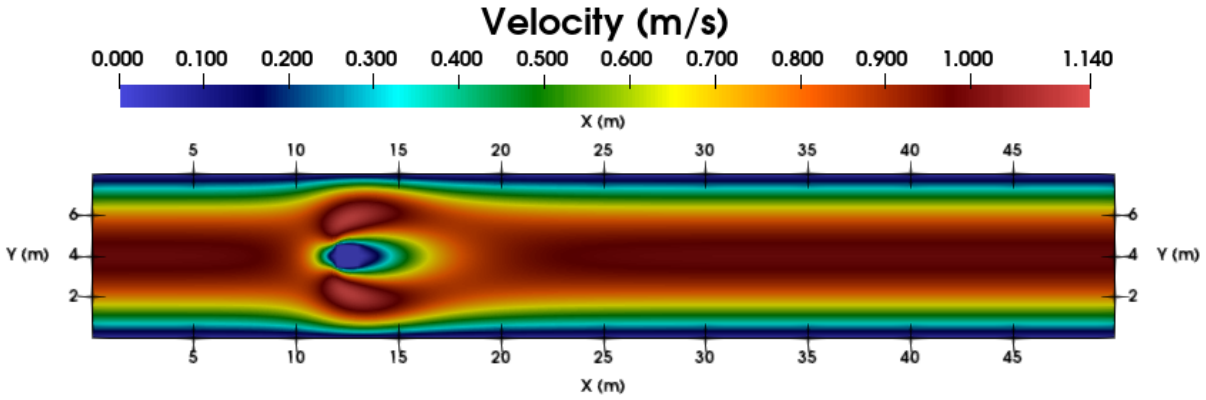

Figure 3.55: Square Cylinder Velocity Magnitude field Reynolds 5

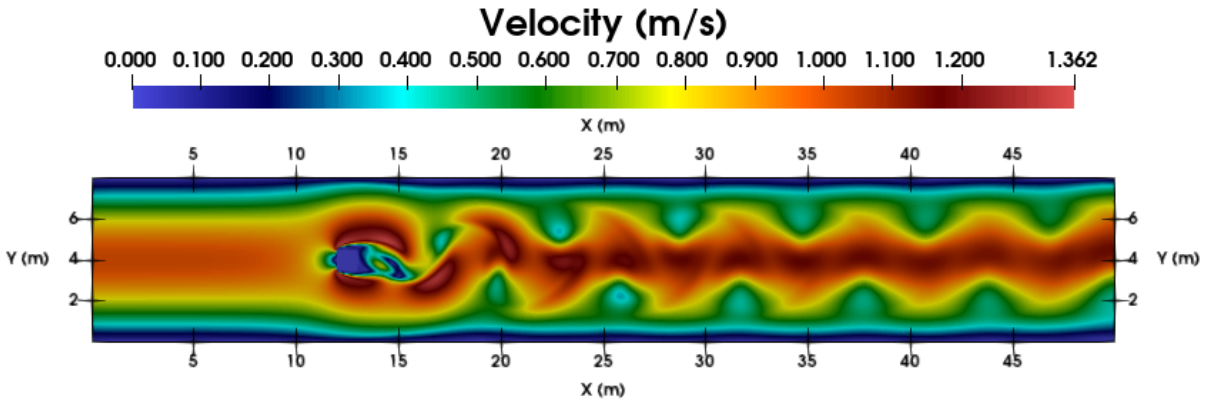

Figure 3.56: Square Cylinder Velocity Magnitude field Reynolds 200

As there can be seen in figure 3.55, the flow remains in an steady state through all the channel. There are only little perturbations due to the presence of the cylinder. Due to the reduced cross section, and fluid's incompressibility, the flow has to increase its velocity in this part. However, as there can be seen in the scale, it is a slightly change in comparison to flow's cross section average speed.

On the other hand, in Reynolds 200 simulation, there can be seen perfectly the oscillation phenomena described previously. Above Critical Reynolds (70 approximately), the flow begins to generate Von-Karman Vortexes behind the cylinder due to its presence.

Finally, it must be at least mentioned the boundary layer generated at the upper and lower walls of the cylinder. This can be observed in a more detailed way in figure 3.56.

As in the case for instance of aerodynamic airfoils, the higher the Reynolds, the larger the boundary layer is, and so in this case.

In addition to the figures exposed, next up are presented the Streamlines fields for the same simulations to give a deeper view of the results.

Streamlines fields.

In figures 3.57 and 3.58 are presented the Streamlines fields for the simulations of Reynolds 5 and 200.

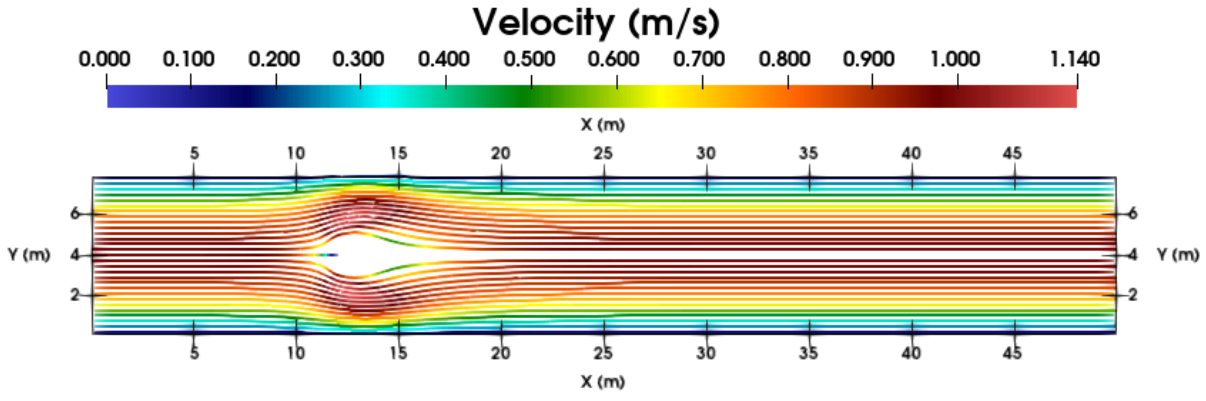

Figure 3.57: Square Cylinder Strealines field Reynolds 5

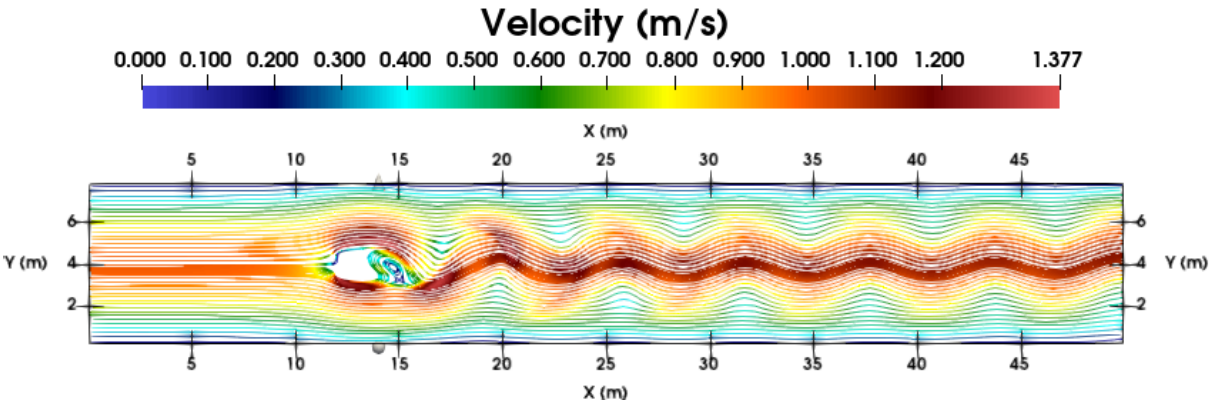

Figure 3.58: Square Cylinder Streamlines field Reynolds 200

There are some conclusions related also to the velocity fields that can be extracted from the previous images.

First, in figure 3.57, there can be seen a steady flow with no mayor perturbations apart from the cylinder. In addition to that, there can be firmly stated that this image is a perfect definition of what a laminar flow is.

As it is already explained at the beginning of section 3.1, laminar regime is characterised by ordered and parallel layers of flow with no transverse velocity. This definition can be clearly extrapolated to figure 3.57.

All its streamlines are perfectly ordered and there is almost no transverse speed apart from the one generated by the presence of the cylinder.

Meanwhile, in Reynolds 200 streamlines field, there can be observed what has already been mentioned. Due to the presence of the cylinder the flow begins to generate Von-Karman Vortexes.

Nevertheless, as there can be observed, the farther these are, the more they are dissipated. It can only be slightly noticed with the scale. However, in a long enough channel, the vortexes generated right behind the cylinder wouldn't be able to reach the outlet of the channel due to its dissipation on the flow.

This loss in kinetic energy takes place due to the viscosity of the fluid. Therefore, the higher the Reynolds is, the longer it takes to dissipate all the energy of the vortexes.

Pressure fields.

To give a final view of the Square Cylinder results, there are presented the relative pressure fields of the simulations of Reynolds 5 and 200 in figures 3.59 and 3.60 respectively.

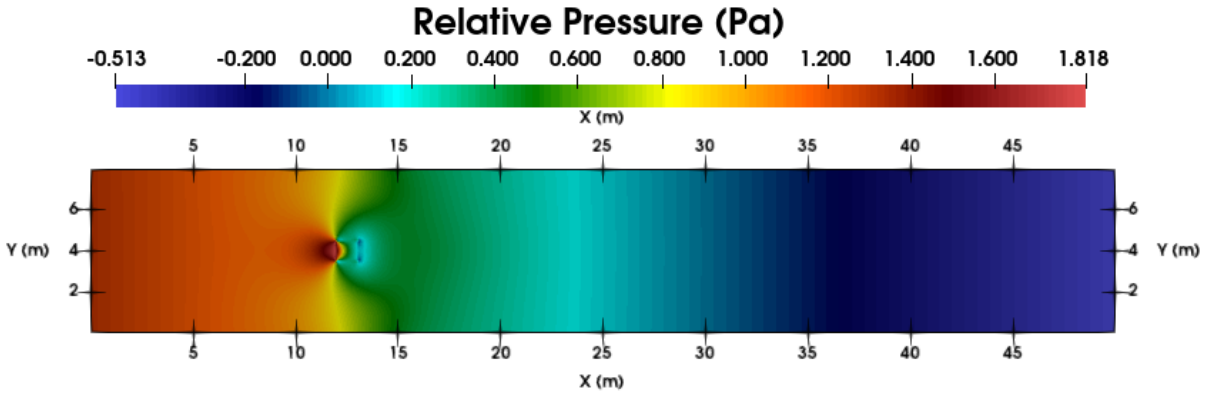

Figure 3.59: Square Cylinder Pressure field Reynolds 5

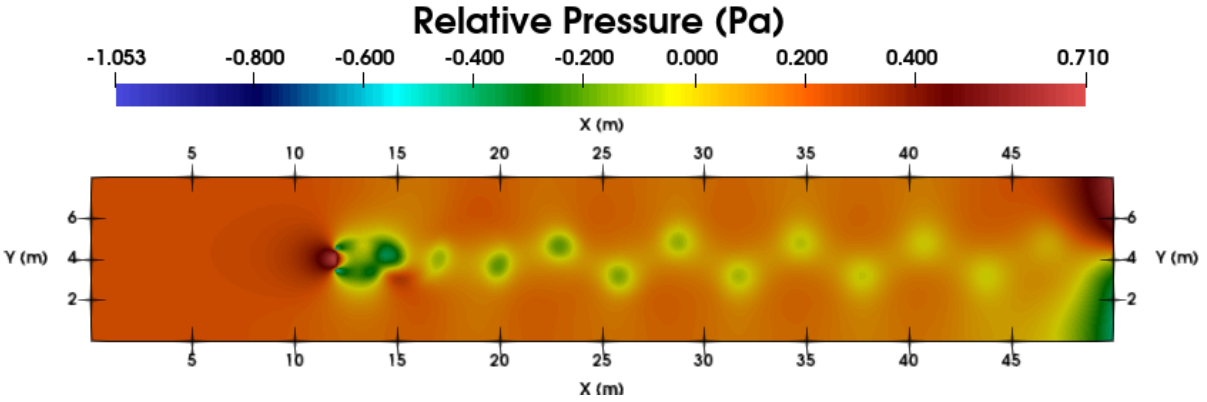

Figure 3.60: Square Cylinder Pressure field Reynolds 200

As there can be seen in both images 3.59 and 3.60, there is a pressure loss right at the upper and lower sides of the cylinder. The theoretical basis of this phenomena has already been explained.

Due to the presence of the cylinder, the channel cross section reduces. And,since the fluid is considered to be incompressible, its velocity must increase.

This acceleration on the fluid makes the relative pressure to decay (Bernouilli's Principle, equation 3.77). This phenomena doesn't only happen in laminar regime or in this case. It is widely and deeply studied problem in fluid mechanics.

However, this pressure loss isn't constant for every flow condition. As there can be seen in figures 3.59 and 3.60, the lower the Reynolds is, the higher the loss.

Finally, looking at image 3.60, there can be observed the vortexes generated by the pressure difference inside and outside these. The pressure field perturbation at the outlet of the channel in figure 3.60 takes place due to boundary conditions. However, this doesn't affect the validity of the results.

Although velocity, streamlines and pressure fields results have been presented and explained in a detailed way, there are several different related parameters or phenomena that will be explained next up in the verification process. To save space, there has been only chosen to present the

images obtained from Reynolds 5 and 200 simulations. However, in the verification process there has been selected to shown the results from every simulation carried out.

This verification data of the obtained results for the simulation case of Square Cylinder have been extracted from a trustworthy scientific source [28].

There will be compared up to 5 different variables results obtained. These are the Recirculation Length, the drag and lift coefficient mean and oscillation values (only mean drag) and the Strouhal number of the system.

Recirculation Length.

Due to the presence of the square cylinder and the flow around it, there is a low relative pressure area right behind this one. This makes the flow close to it to go that zone due to the pressure gradient. Therefore, there is an area in which fluid's velocity is opposite to the main flow.

And it isn't until a certain distance behind the cylinder that the velocity returns to have the same direction as the main flow. This distance is known as "Recirculation length". In order to give a better insight of this physical phenomena, it is presented in figure 3.61 mentioned area Streamlines field in Reynolds 50 case.

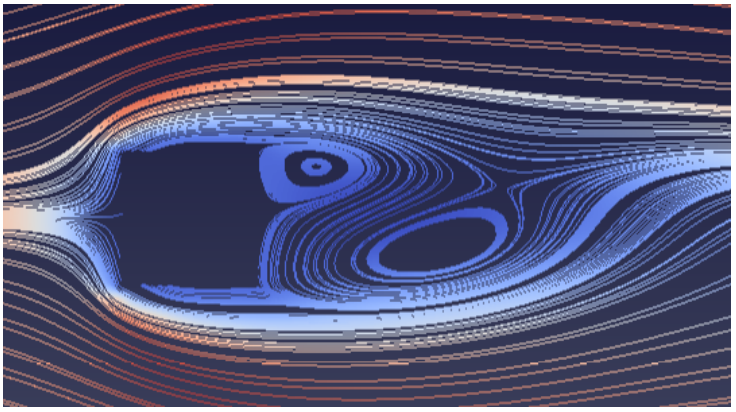

Figure 3.61: Square Cylinder Reynolds 50 Streamlines field behind the cylinder

As there can be seen in figure 3.61, the flow changes its direction because of the pressure gradient due to the presence of the cylinder. Recirculation Length grows as the Reynolds number does due to the fact that it depends enormously on the dominance of the inertial forces over viscosity. However, once the system begins to oscillate, there is no reason to use this parameter as a measure variable because it continuously changes with the oscillations.

Next up in figure 3.62 is presented the comparison of the Recirculation Length results with the ones from the mentioned scientific source.

In figure 3.62, there can be seen what has been mentioned before. The higher the Reynolds is, the higher the Recirculating Length is. A higher Reynolds makes the pressure behind the cylinder to be lower and so it is harder for the deviated flow to come back to its initial direction.

In what comes to the accuracy of the obtained results, the following statement can be made.

Despite the fact that, at higher Reynolds number, there is a slightly difference between both results, these can be considered as acceptable. It can be clearly observed, the similar mathemat-

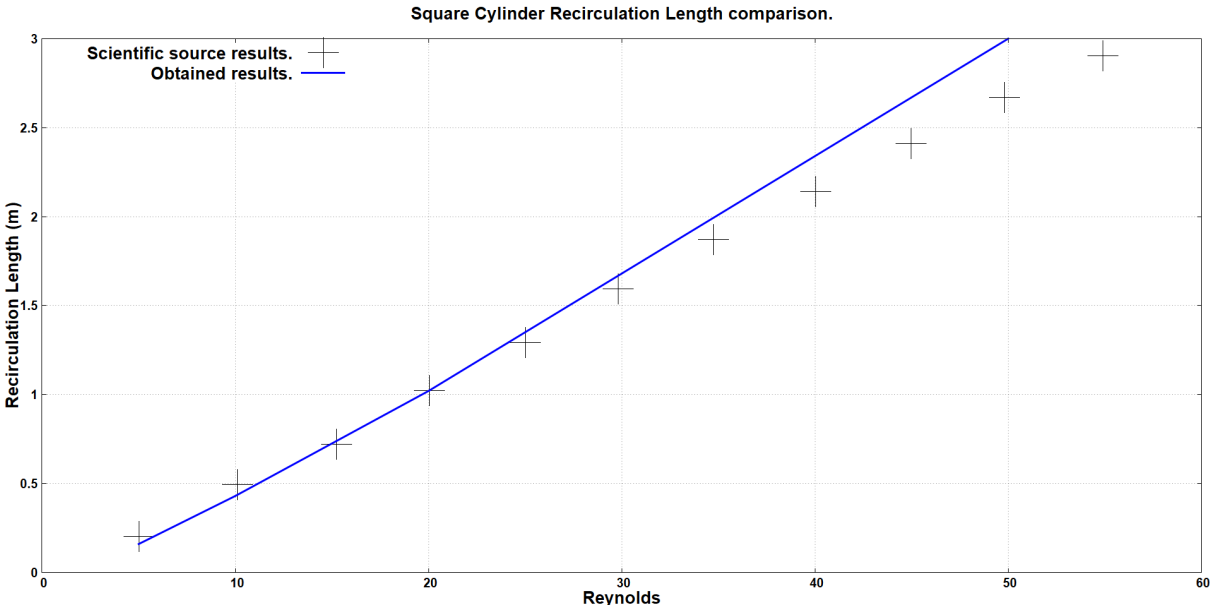

Figure 3.62: Recirculation Length results comparison

ical tendency on both cases. Moreover, none of the results have a relative error above 10% or 15%, so they can be considered as correct from an engineering point of view.

Drag and Lift Coefficients.

As it has been mentioned, due to the presence of the cylinder inside the flow, there is a drag force on the same direction as the first of these. And, since there is only flow in the horizontal direction, there is lift coefficient due to forces on the vertical axis.

However, this changes when system begins to oscillate. Drag coefficient begins to swing around a certain Reynolds dependant value, and lift ceases being null.

In every fluids mechanics or aerodynamics problem, the drag and lift coefficients are computed as follows.

$$C_D = \frac{D_F}{\frac{1}{2}\rho \overline{U}^2 L_{Ref}} \tag{3.82}$$

$$C_L = \frac{L_F}{\frac{1}{2}\rho \overline{U}^2 L_{Ref}} \tag{3.83}$$

As the reader may think, the reference length and velocity must be the same as the ones chosen for the case simulations.

$$C_D = \frac{D_F}{\frac{1}{2}\rho (\frac{U_{max}}{\sqrt{2.0}})^2 D} \tag{3.84}$$

$$C_L = \frac{L_F}{\frac{1}{2}\rho (\frac{U_{max}}{\sqrt{2.0}})^2 D} \tag{3.85}$$

The only unknown parameters are the drag and lift forces, D_F and L_F respectively.

In order to calculate them, it is necessary to take into account the pressure difference between both sides of the cylinder and the viscous stresses on its surface.

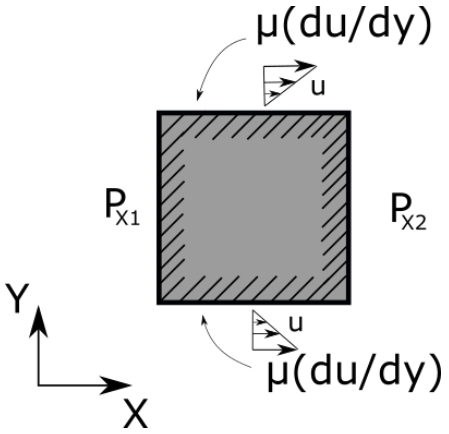

Figure 3.63: Drag coefficient calculation scheme

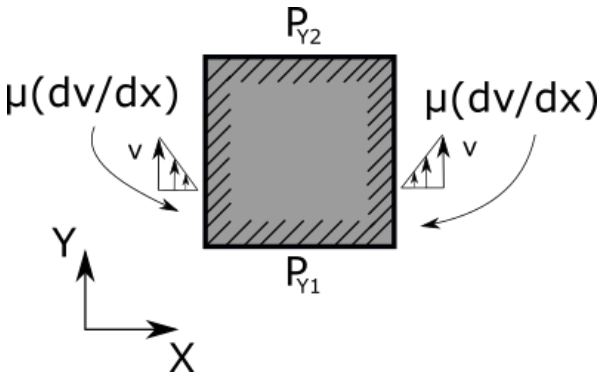

Figure 3.64: Drag coefficient calculation scheme

Since the obtained pressure and velocity results are discrete, it is necessary to do a sweep on every control volume at cylinder's face for each case.

$$D_F = \sum_f \left[P_{X1i} \cdot \Delta S_{X1} - P_{X2i} \cdot \Delta S_{X2} + \mu \frac{\partial u_{1i}}{\partial y} \Delta S_{Y1} + \mu \frac{\partial u_{2i}}{\partial y} \Delta S_{Y2} \right] \tag{3.86}$$

$$L_F = \sum_f \left[P_{Y1i} \cdot \Delta S_{Y1} - P_{Y2i} \cdot \Delta S_{Y2} + \mu \frac{\partial v_{1i}}{\partial x} \Delta S_{X1} + \mu \frac{\partial v_{2i}}{\partial x} \Delta S_{X2} \right] \tag{3.87}$$

Once the coefficients calculation processes have been explained, it is presented the obtained results for them in the simulations.

First, in table 3.11, it is presented the Drag Coefficient comparison.

Table 3.11: Square Cylinder Drag Coefficient results comparison

Reynolds	Mean Drag Results	Breuer M. Results	Relative Error (%)
1	23.58	24.2	2.56
5	5.62	5.75	2.26
10	3.65	3.60	1,39
20	2.41	2.40	0.42
50	1.64	1.60	2.50
70	1.44	1.43	0.70
100	1.35	1.35	0.00
150	1.29	1.32	2.27
175	1.34	1.33	0.75
200	1.36	1.34	1.50

For Reynolds numbers equal or above 70, the shown Drag Coefficient is its mean value.

As there can be seen in table 3.11, drag coefficient has a strong dependence on the viscous effects of the flow. At Reynolds 1, it has an huge value in comparison to the rest of simulations.

At this flow regime, the viscosity plays an important role on the drag force calculation, representing a great part of it. However, the higher the Reynolds is, the lower C_D. This happens due to the following reasons.

First, although the pressure difference between the frontal and back face of the cylinder is higher as Reynolds increases, its contribution to the drag represents a little part of the total force. In addition to that, as there has been seen, the higher Reynolds, the lower dynamics viscosity. Despite the fact that velocity gradient at the walls are higher as Reynolds increase, μ plays a huge role on the total drag force due to viscosity stress, and so the global contribution is reduced.

In what comes to the accuracy of the obtained results, there can be clearly seen in table 3.11 that they can be firmly considered as acceptable from an engineering point o view. It is almost impossible to get exactly the same values, there are too many factors like numeric scheme chosen, nodal density or distribution or even the resolution method.

In the following tables 3.12 and 3.13, there are presented the drag and lift coefficients oscillation value and the comparison with the reference selected.

Table 3.12: Square Cylinder Drag Coefficient variation comparison

Reynolds	$(C_{Dmax} - C_{Dmin})$ Results	Breuer M. Results	Relative Error (%)
70	0.0011	0.001	10.00
100	0.0091	0.01	9.00
150	0.0274	0.03	8.67
175	0.045	0.040	11.85
200	0.069	0.07	1.43

Table 3.13: Square Cylinder Lift Coefficient variation comparison

Reynolds	$(C_{Lmax} - C_{Lmin})$ Results	Breuer M. Results	Relative Error (%)
70	0.230	0.26	11.53
100	0.383	0.391	2.05
150	0.573	0.62	7.58
175	0.87	0.87	0.46
200	1.224	1.20	2.00

Additionally, it is presented the temporal evolution of the drag and lift coefficient respectively for Reynolds 200 simulation.

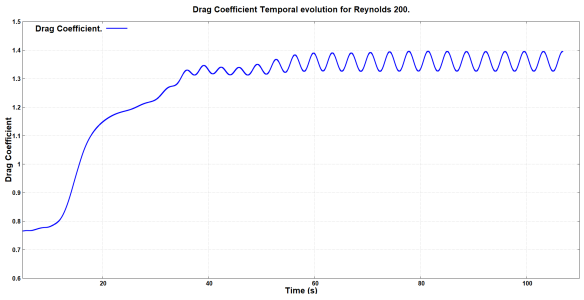

Figure 3.65: Drag coefficient temporal evolution for Reynolds 200

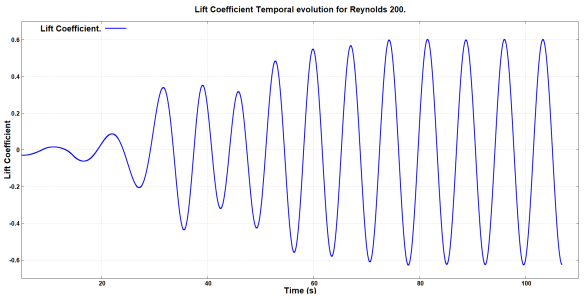

Figure 3.66: Lift coefficient temporal evolution for Reynolds 200

As there can be seen in figures 3.65 and 3.66, the drag and the lift coefficients begin to vary until they arrive to a periodic oscillating state.

Depending on the simulation parameters, specially, Reynolds number, the system may take longer or not to achieve this state. However, as in case of the steady LID Driven Cavity and Differentially Heated, the system always arrive to it.

As it was expected, the drag coefficient oscillates around a certain value. However, since the lift coefficient is a secondary effect of the oscillations, its value swings around 0. In case of computing the mean value, it may give something different to 0, but very close to it due to numerical inaccuracies and not enough resolution.

Additionally, as there can be observed in tables 3.12 and 3.13, the higher Reynolds, the higher oscillation amplitude. This makes sense due to the fact that, as Reynolds increases, so does the size of the vortexes generated. However, these have different effects on each coefficient.

Looking at table 3.12, there can be clearly stated that these oscillations doesn't affect so much to the drag coefficient. This phenomena can be explained by looking at how it is computed.

Observing equation (3.86) and scheme 3.63, there can be seen that the only variation that the oscillations produce consists on the change in the pressure field behind the cylinder. As it has been said, this has a little contribution to the overall coefficient value, so the local temporal value of the coefficient is slightly modified.

On the other side, as there can be seen in table 3.13, the lift coefficient is severely affected by the oscillations. Again, looking at how it is calculated (equation (3.87) and figure 3.64) there can be seen that the oscillations modify the velocity profile behind the cylinder and so the force due to viscous stresses.

In terms of results accuracy, there are several important things to mention.

First of them is that, these kind of parameters are not easy to calculate or to get the most accurate value. As in every simulation, there are many factors that may vary slightly the solution obtained such as numeric scheme selected, total number of nodes, etc..

Nevertheless, although relative errors for the coefficient variations may seem too large in comparison with other calculated parameters in this project, they can be considered as acceptable. It is true, that some of them, like Reynolds 70 to 150, could be more accurate.

This happens because, when doing that simulations, the total amount of nodes were reduced without compromising the validity of the results. A great reduction of them was achieved, however, this affected slightly to the results. The perfect example of this is Reynolds 200 simulation. In this case, there were no extreme mesh optimisation to reduce the total nodes number. Therefore, great results in every parameter where achieved.

However, none of these results has a relative error above 15%. This means they can be considered as correct from a Computational Fluid Dynamics point of view.

Strouhal number.

Last result to be verified in the Strouhal number. As it is already explained in section 2.3, this parameter is a non-dimensional number related to the frequency of any system.

$$St = \frac{f \cdot L_{Ref}}{U_{Ref}}$$

In this case, it is related to the temporal frequency of the oscillations. As for other non-dimensional numbers in Square Cylinder case, the reference length and velocity are cylinder's side value and mean inlet speed respectively.

$$St = \frac{f \cdot D\sqrt{2.0}}{\overline{U}} \tag{3.88}$$

Next up, in table 3.14 it is presented the comparison for the obtained Strouhal number results in the simulations.

Table 3.14: Square Cylinder Strouhal number comparison

Reynolds	Obtained Results	Source Results	Relative Error (%)
70	0.128	0.126	1.59
100	0.136	0.138	1.45
150	0,160	0.143	11.88
175	0.144	0.140	2.85
200	0.137	0.134	2.75

Looking at table 3.14, there are some conclusions that can be extracted. First, as there can be seen, the frequency of the oscillations is not severely affected by the Reynolds number variation. It reaches a maximum near Reynolds 150, but then it decays again.

From the accuracy point of view, there can be stated that, apart from Reynolds 150 results, the rest have a more than negligible relative error. Moreover, the highest of these are below the mentioned 15%. Therefore, all of the obtained results for the Strouhal number are considered to be correct.

Chapter 4

Turbulent Regime.

4.1 Theoretical framework.

Almost all fluid flows of our daily life are heavily dominated by turbulence. From the flow around a car, aircraft boundary layers, the air of a room, or even our blood. Mainly every flow witnessed every day is turbulent.

This flow regime can be easily described in only one word, chaos. It is a form of fluid transport in which velocities fluctuate randomly, disrupting the orderly and parallel fluid layers from laminar regime. In this case, transverse flows appear due to the randomness of the fluid resulting in chaotic velocity fields like the one presented in figure 4.1.

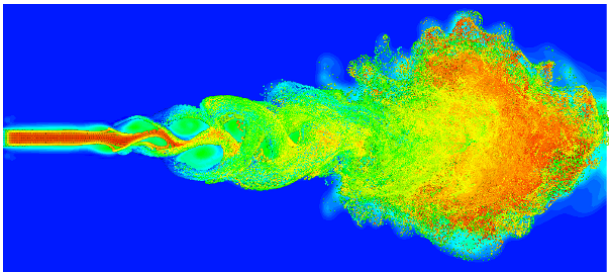

Figure 4.1: CFD Simulation of the development of turbulent flow in a jet. Extracted from [11]

As there can be seen in the image, the flow inlet can be still considered as laminar. However, it goes through a transition during a small distance and the it becomes turbulent rapidly. There is no fluid pattern or any kind of order. The flow variables are randomly fluctuating.

Turbulent flow are characterised by been heavily irregular, highly unsteady, difficult to predict and chaotic.

In addition to that, turbulence usually occurs at high Reynolds numbers. For instance, in boundary layer, the mentioned laminar to turbulent transition takes place at Reynolds 500000 approximately.

Other important aspect of turbulent flow is that it is always tri-dimensional and unsteady. However, depending on the equations treatment and problem's geometry, it can be considered as bi-dimensional. This is going to be crucial for the development of turbulent regime part of this project.

From a theoretical point of view, turbulence remains still as one of science biggest problems. Even nowadays, turbulent flows require a great amount of resources and knowledge to be able

to study it.

In Computational Fluid Dynamics this doesn't change. Most of engineering and scientific inventions related to fluid mechanics are heavily dependant on turbulent flows. Because of this, there has been a great focus in this area and how to carry out this kind of simulations.

During decades, many different techniques, algorithms or even theories have been developed in order to be able to predict the behaviour of these flows. Turbulence modelling is a branch of knowledge that has been developed for almost half century. Nowadays, even with the exponential increase in computational power, there are still many difficulties to do that.

In this project there will be presented the implementation of one of these different turbulence modelling techniques, RANS (Reynolds Averaged Navier-Stokes).

In addition to that, due to the computational resources available, there are several hypothesis that must be assumed for the turbulent flow simulation. These are presented next up, in section 4.1.1.

4.1.1 Hypothesis and simplifications made

As in the case of the laminar regime simulations, in this part of the project there are some theoretical and numerical assumptions. These are presented and described next up in the present section.

Continuous flow distribution

As in the laminar regime, continuous flow distribution assumption is one of the basis of the simulations of turbulent regime flows.

Axisymmetrical flow.

As it is exposed in the laminar regime hypothesis section (section 3.1.1), the flow was considered to be bi-dimensional.

In this case, the assumption made about this is similar. In the turbulent regime part of the project, all the simulations have what's known as axisymmetric geometry.

The easiest case to think about is a pipe. It has a central axis and complete symmetry with respect to this. So, in order to reduce the computational power required, it has been decided to remove the azimuthal (angular) flow direction. This can make the fluid to be considered as bi-dimensional in a roughly way.

To learn more about the implementation of this decision, go to section 4.5.1).

Compressible flow

One of the main characteristics of the laminar regime simulations carried out was the fluid's incompressibility.

However, since one of the main characteristics chosen for the flow is that this is supersonic, it is absolutely impossible to consider it as incompressible.

Usually, in fluid mechanics, the limit to consider a fluid compressible or incompressible ranges near Mach 0.3. Supersonic flow Mach number is always higher or equal to 1.0. Therefore, considering it as incompressible would be an unacceptable mistake.

Newtonian fluid

As in the laminar regime studies, the simulation fluid is considered to be Newtonian for the turbulent part of the project as well.

Temperature dependant fluid viscosity.

Due to the characteristics of the flow and the simulations to carry out in this part of the project, there has been selected set fluid's viscosity as temperature dependant.

The fact that flow is compressible and supersonic makes impossible to set a fixed fluid's viscosity. There are huge temperature and pressure changes in the flow that affects severely this physical property.

Due to this aspect, there has been chosen to use the Sutherland's viscosity law. This was proposed by the Scottish scientist William Sutherland.

He came with the idea of defining the dynamic viscosity of a fluid depending on its temperature and certain fluid's physical properties. There are different mathematical expressions of the viscosity as a function of temperature. For this project, the following one is used.

$$\frac{\mu(T)}{\mu_{Ref}} = \left(\frac{T}{T_{Ref}}\right)^{n} \tag{4.1}$$

Constant heat capacity ratio.

Since the effects of temperature and pressure changes are almost negligible, heat capacity ratio can be considered as constant. This parameter is defined as follows.

$$\lambda = \frac{C_P}{C_V} \tag{4.2}$$

Constant specific heat coefficient.

Due to the decision in the previous hypothesis, the constant volume heat capacity (C_v) can be considered as constant.

This makes the code implementation a little bit easier. In this case, it is possible to assume the following.

$$\partial e = C_v \cdot \partial T \tag{4.3}$$

In addition to that, since the value is fixed, there is no need for spending computational resources on its calculation.

Ideal gas.

It is considered that the simulation gas is ideal. Although this is no 100% accurate, it simplifies enormously the numerical implementation. Moreover, many scientific publications of compressible flows use the same hypothesis.

This hypothesis allows to compute the pressure using the following mathematical expression.

$$P = \rho \cdot R \cdot T \tag{4.4}$$

4.1.2 Turbulent regime Navier - Stokes equations.

In this section are presented the Navier-Stokes Mass, Momentum and Energy equations with the hypothesis and assumptions previously mentioned.

- **Mass conservation equation.**

$$\frac{\partial \rho}{\partial t} + \nabla \cdot (\rho \mathbf{u}) = 0 \tag{4.5}$$

- **Momentum conservation equation.**

$$\frac{\partial \rho \mathbf{u}}{\partial t} + \nabla \cdot (\rho \mathbf{u}\mathbf{u}) = -\nabla p + \nabla \cdot \tau \tag{4.6}$$

  X axis.

$$\frac{\partial \rho u}{\partial t} + \nabla \cdot (\rho u u) = -\frac{\partial p}{\partial x} + \nabla \cdot \tau | u \tag{4.7}$$

  R axis.

$$\frac{\partial \rho v}{\partial t} + \nabla \cdot (\rho v v) = -\frac{\partial p}{\partial r} + \nabla \cdot \tau | r \tag{4.8}$$

  Since the flux has been considered as axisymmetric in X-R plane, there is no need for considering azimuthal axis equations anymore.

- **Energy conservation equation.**

$$\frac{\partial \rho e}{\partial t} + \nabla \cdot (\rho \mathbf{u} e) = -p \cdot \nabla \mathbf{u} + \nabla q + \tau : \nabla \mathbf{u} \tag{4.9}$$

To see the mathematical development of terms $\nabla \cdot \tau | u$, $\nabla \cdot \tau | r$ and $\tau : \nabla \mathbf{u}$ from the axial and radial momentum and energy equations, go to appendix G in Annex document of this project.

4.2 Turbulence modelling

As there has been seen in the previous section (section 4.1), turbulence represent an enormous challenge from a theoretical and numerical point of view. The difficulty of the physical phenomena involved is way beyond from the laminar regime.

In addition to that, the computational power required to simulate this flow regime grows exponentially as the turbulence increase. The total number of nodes needed for the simulation of turbulent regime is considered to grow at a rate of $Re^{2.25}$.

Unfortunately, even today, with the enormous increase in computational power, it is impossible to do certain turbulent regime studies. Because of this, researchers ad engineers have developed during decades many ways to modelling turbulence and the phenomena involved.

The most common methods of turbulence modelling are DNS (Direct Numerical Simulation), LES (Large Eddy Simulation) and RANS (Reynolds Averaged Navier-Stokes equations).

First of them, DNS, consists on using the same numerical methods as in laminar regime increasing the mesh up to the simulation requirements.

On the one hand, it is the easiest way to simulate turbulence. No modifications for the equations or the resolution are needed. However, on the other hand, these kind of simulations require a huge computational power. Nowadays, it is absolutely impossible to carry out these type of studies in a personal computer. It is necessary an enormous cluster of hundreds or even thousands of CPUs. And still, it isn't enough to simulate industrial applications cases.

By comparison, LES (Large Eddy Simulation) doesn't require the same amount of resources as DNS. As the reader may sense from its name, this method consists on the simulation of the large scales of the flow and the modelling of the smaller ones. This reduces dramatically the computational power required. However, it increases the implementation difficulty.

In this project there has been chosen to apply RANS modelling basis due to the physical characteristics of the study case. Next up is presented this turbulence modelling method in a much more detailed way.

4.2.1 Reynolds Averaged Navier Stokes Equations (RANS).

As its name already indicates, RANS turbulence modelling theory is based on averaging values. Turbulent flow is considered to be fluctuating. Therefore, RANS equations average these fluctuating variables by splitting them in two terms (equation (4.10)).

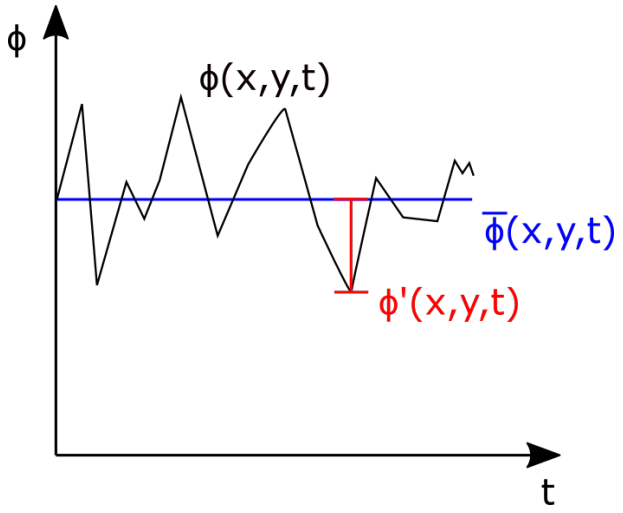

Figure 4.2: RANS averaging scheme

$$\phi(x,y,t) = \overline{\phi}(x,y,t) + \phi'(x,y,t) \tag{4.10}$$

The fluctuating, spatial and time dependant variable $\phi(x,y,t)$ is divided into its averaged $\overline{\phi}(x,y,t)$ and its fluctuation $\phi'(x,y,t)$ values .

Then, in order to obtained the RANS equations, it is necessary to average them. To do that, the following averaging mathematical expression is applied (equation (4.11)).

$$\overline{\phi}(x,y,t) = \frac{1}{\Delta t} \cdot \int_t^{t+\Delta t} \phi(x,y,t)dt \tag{4.11}$$

In case of averaging the average part of the variable, this stays as before (equation (**??**)).

$$\frac{1}{\Delta t} \cdot \int_t^{t+\Delta t} \overline{\phi}(x,y,t)dt = \overline{\phi}(x,y,t) \tag{4.12}$$

However, the average of a fluctuation value is always 0 (equation (4.13)). This can be clearly seen in figure 4.2.

$$\frac{1}{\Delta t} \cdot \int_t^{t+\Delta t} \phi'(x,y,t)dt = 0 \tag{4.13}$$

Applying these mathematical conversions and rules to the original Navier-Stokes equations lead to the Reynolds Averaged Navier-Stokes equations. However, since simulation flow is compressible, it is necessary to make a few changes in this.

First, the RANS equations must be called FANS (Favre averaged Navier-Stokes). For compressible flows Favre averaging is used to simplify the mathematical development. Nevertheless, from the point of view of the equations, both are the same. The two averaging methods arrive to the same results at the end.

Favre averaging is based on the following statement.

$$\overline{\rho\phi} = \overline{\rho \cdot (\widetilde{\phi} + \phi'')} = \overline{\rho \cdot \widetilde{\phi}} + \overline{\rho \cdot \phi''}$$

$$\overline{\rho \cdot \widetilde{\phi}} = \overline{\rho}\widetilde{\phi} = \cancel{\overline{\rho}} \cdot \frac{\overline{\rho \cdot \widetilde{\phi}}}{\cancel{\overline{\rho}}} = \overline{\rho \cdot \phi}$$

$$\overline{\rho \cdot \phi} = \overline{\rho \cdot \widetilde{\phi}} + \overline{\rho \cdot \phi''} = \overline{\rho \cdot \phi} + \overline{\rho \cdot \phi''} \longrightarrow \boxed{\overline{\rho \cdot \phi''} = 0} \tag{4.14}$$

It is based on density weighted averaging. This eases a lot the mathematical development for compressible flows.

To give a better insight of Favre averaging method, it is presented the mathematical development of Mass Conservation equation next up.

Mass Conservation Equation.

$$\frac{\partial \rho}{\partial t} + \nabla \cdot (\rho \mathbf{u}) = 0 \tag{4.15}$$

To ease the understanding, each term development is shown.

$$\overline{\frac{\partial \rho}{\partial t}} = \frac{\partial \overline{\rho}}{\partial} \tag{4.16}$$

$$\overline{\nabla \cdot (\rho \mathbf{u})} = \nabla \cdot (\overline{\rho \cdot (\widetilde{\mathbf{u}} + \mathbf{u}'')}) = \nabla \cdot (\overline{\rho \cdot \widetilde{\mathbf{u}}} + \overbrace{\overline{\rho \cdot \mathbf{u}''}}^{0}) = \nabla \cdot (\overline{\rho} \cdot \widetilde{\mathbf{u}}) \tag{4.17}$$

Adding obtained terms lead to the following Reynolds Averaged Navier-Stokes Mass Conservation equation (equation (4.18)).

$$\frac{\partial \overline{\rho}}{\partial t} + \nabla \cdot (\overline{\rho} \cdot \widetilde{\mathbf{u}}) = 0 \tag{4.18}$$

As there can be seen, the obtained equation is equal to the initial one. In the implementation, the averaging is already taken into account in this equation, there is no need to make any changes on it.

However, this doesn't happen in the Momentum and Energy Conservation equations.

Averaging these leads to the following expressions for each of them respectively (equations (4.19), (4.20) and (4.21)). To see the mathematical development of these equations, go to appendix E in Annex document of this project.

$$\frac{\partial (\overline{\rho} \cdot \widetilde{u})}{\partial t} + \nabla \cdot (\overline{\rho} \widetilde{\mathbf{u}} \widetilde{u}) = -\frac{\partial \overline{P}}{\partial x} + \nabla \cdot (\widetilde{\tau|_x}) + \nabla \cdot \underbrace{(\overline{\tau''|_x} - \overline{\rho \mathbf{u}'' u''})}_{New\ \ Terms} \tag{4.19}$$

$$\frac{\partial(\overline{\rho}\cdot\widetilde{v})}{\partial t}+\nabla\cdot(\overline{\rho}\widetilde{\mathbf{u}}\widetilde{v})=-\frac{\partial\overline{P}}{\partial y}+\nabla\cdot(\widetilde{\tau|_y})+\nabla\cdot\underbrace{(\overline{\tau''|_y}-\overline{\rho\mathbf{u}''y''})}_{New\ \ Terms} \tag{4.20}$$

$$\frac{\partial\overline{\rho}\widetilde{e}}{\partial t}+\nabla\cdot(\overline{\rho}\widetilde{\mathbf{u}}\widetilde{e})=-\overline{p}\cdot\nabla\cdot(\widetilde{\mathbf{u}})-\nabla\widetilde{q}+\widetilde{\tau}:\nabla(\widetilde{\mathbf{u}})\underbrace{-\nabla\cdot(\overline{\rho\mathbf{u}''e''})}_{New\ \ Term} \tag{4.21}$$

For further information about Favre averaging go to [29].

As there can be seen, the equations are equal, except for 2 additional terms on each of them.

In order to solve the momentum equation, it is needed to add the effect these terms have on the overall contributions to the velocities. To do that, they need to be modelled.

The mathematical development of the process is way beyond project's scope. Therefore, it will be mentioned only the modification in the simulation code.

Usually, the kinematic or dynamic viscosity of the fluid is computed depending on the Reynolds number, on the temperature, on the fluid properties, etc...

Nevertheless, what is done in RANS modelling to take into account the effects of the new terms of the equations is adding a new turbulent viscosity.

$$\mu_{New}=\mu+\mu_t \tag{4.22}$$

This new viscosity μ_{New} substitutes the former viscosity in the Momentum Conservation equation and for instance, in the time step value calculation. Instead of working with the fluid's base viscosity, turbulent one is added.

The question now is, how to compute this new turbulent viscosity. To do that, researchers and engineers have developed turbulence models.

These take the fluid conditions and compute the turbulent viscosity. There are many types of RANS turbulence models. Linear eddy viscosity models, non-linear eddy viscosity models, Reynolds stress based viscosity models, etc...

However, the most commons RANS models are the one-equation and two-equation models.

For this project, the RANS model selected for the turbulent regime simulations is the Spalart-Allmaras turbulence model, which will be presented next up in a more detailed way.

Spalart-Allmaras turbulence model.

The Spalart-Allmaras model is a RANS one equation model designed specifically for aerospace applications.

It was first developed and presented by Phillipe Spalart and S. R Allmaras in 1994 in their paper "A one-equation turbulence model for aerodynamic flows while working at Boeing.

This model solves a transport equation for the kinematic turbulent viscosity $(\widetilde{\nu})$, also known as "Spalart-Allmaras variable".

Next up is presented the transport equation proposed by the authors in 1994.

$$\frac{\partial \widetilde{\nu}}{\partial t} + \nabla \cdot (\widetilde{\nu}\mathbf{u}) = C_{b1}\widetilde{S}\widetilde{\nu} + \frac{1}{\sigma}\left[\nabla((\nu + \widetilde{\nu}) \cdot \nabla\widetilde{\nu}) + C_{b2}\nabla\widetilde{\nu} \cdot \nabla\widetilde{\nu}\right] - C_{w1}f_w\left(\frac{\widetilde{\nu}}{d}\right)^2 \tag{4.23}$$

In addition to the transport equation shown before, there are several parameters or variables that need to be calculated on every step of the simulation.

$$\mu_t = \widetilde{\nu} \cdot \rho \cdot f_{v1} \tag{4.24}$$

$$f_{v1} = \frac{X^3}{X^3 + C_{v1}^3} \tag{4.25}$$

$$X = \frac{\widetilde{\nu}}{\nu} \tag{4.26}$$

$$f_w = g \cdot \left[\frac{1 + C_{w3}^6}{g^6 + C_{w3}^6}\right]^{1/6} \tag{4.27}$$

$$g = r + C_{w2} \cdot (r^6 - r) \tag{4.28}$$

$$r = min\left(\frac{\widetilde{\nu}}{\widetilde{S} \cdot K_{VK}^2 \cdot d^2}, 10.0\right) \tag{4.29}$$

$$\widetilde{S} = S + \frac{\widetilde{\nu}}{K_{VK}^2 \cdot d^2} \cdot f_{v2} \tag{4.30}$$

$$f_{v2} = 1.0 - \frac{X}{1.0 + X \cdot f_{v1}} \tag{4.31}$$

$$S = \sqrt{2.0 \cdot \omega \cdot \omega} \tag{4.32}$$

$$\omega = \frac{1}{2} \cdot \left(\frac{\partial u}{\partial y} - \frac{\partial v}{\partial x}\right) \tag{4.33}$$

$$C_{w1} = \frac{C_{b1}}{K_{VK}^2} + \frac{(1.0 + C_{b2})}{\sigma} \tag{4.34}$$

Next up in table 4.1 are presented the values of all constants needed to solve the model.

Table 4.1: Spalart-Allmaras turbulence model constants values. Extracted from [12]

Constant	Value
σ	2/3
C_{b1}	0.1355
C_{b2}	0.6220
K_{VK}	0.4100
C_{w2}	0.3000
C_{w3}	2.0000
C_{v1}	7.1000

As it has been said, Spalart and Allmaras presented in 1994 the transport equation for the eddy turbulent viscosity, equation (4.23). However, this expression is only valid for incompressible

flows. In case of compressible regime studies, it is necessary to modify slightly the equation as follows.

$$\frac{\partial \rho \widetilde{\nu}}{\partial t} + \nabla \cdot (\rho \widetilde{\nu} \mathbf{u}) = C_{b1} \widetilde{S} \rho \widetilde{\nu} + \frac{1}{\sigma} [\nabla((\mu + \rho \widetilde{\nu}) \cdot \nabla \widetilde{\nu}) + C_{b2} \nabla \widetilde{\nu} \cdot \nabla \widetilde{\nu}] - C_{w1} \rho f_w \left(\frac{\widetilde{\nu}}{d} \right)^2 \quad (4.35)$$

This is the transport equation for the eddy turbulent viscosity that is going to be implemented for the simulation.

In order to give a better insight of the turbulence model, next up, each term of the previous equation will be explained in a more detailed way.

- **Eddy turbulent viscosity change rate ($\frac{\partial \rho \widetilde{\nu}}{\partial t}$).**

  As in Mass, Momentum and Energy Conservation equations, this term represents the rate of change of the eddy turbulent viscosity inside the control volume studied.

- **Eddy turbulent viscosity flow into the volume ($\nabla \cdot (\rho \widetilde{\nu} \mathbf{u})$).**

  It represents the eddy turbulent viscosity flowing through the bounding surfaces of the chosen control volume in and out of it because of the fluid's velocity.

- **Eddy turbulent viscosity generation term ($\mathbf{C}_{b1} \widetilde{S} \rho \widetilde{\nu}$).**

  This term represents the flow turbulence generation due to velocity gradients (shears) in the flow field.

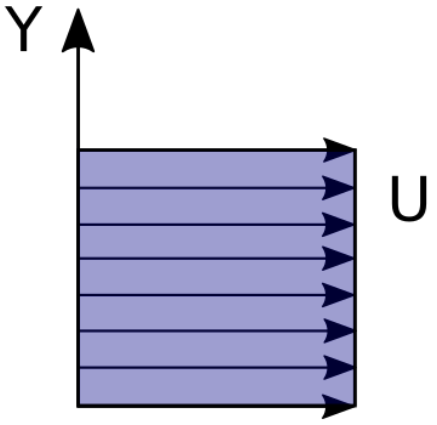

Figure 4.3: Constant velocity profile scheme

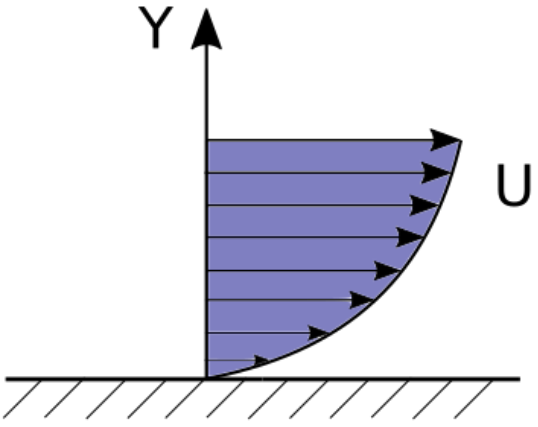

Figure 4.4: Variable velocity profile scheme

Figures 4.3 and 4.4 are presented to give a better understanding of this phenomena.

The viscosity generation of the model depends mainly on this term. And its value relies directly on the velocity gradient, as it can be seen in equations (4.30), (4.32) and (4.33). For instance, in figure 4.3, the turbulent velocity generation would be null, while on the

second scheme (figure 4.4), there is a clear and significant velocity gradient on the Y direction, and so it is taken into account to produce turbulent viscosity.

The term considers speed variations in the horizontal and vertical axis (in case of being 3D, it would also do for the other direction) and generates a directly proportional quantity of turbulent viscosity.

- **Diffusion of turbulence term** $(\frac{1}{\sigma}[\nabla((\mu+\rho\widetilde{\nu})\cdot\nabla\widetilde{\nu})+C_{b2}\nabla\widetilde{\nu}\cdot\nabla\widetilde{\nu}])$**.**

  As in many physical variables transport equations, there is a diffusion term which allows these properties to spread out from region in which there are high concentrations of them to lower ones. This is the case of the present term.

  In addition to what has been mentioned, this expression can be splited in two. The first term, $\frac{1}{\sigma}\nabla((\mu+\rho\widetilde{\nu})\cdot\nabla\widetilde{\nu})$ is known as the linear term. Comparing it with other diffusion terms from other equations such as Momentum Conservation equation (section 2.2.4), there can be seen that both have a common structure.

  However, the second term is non-linear, also known as source term. It was added by the model authors to control and get a more accurate spread of wakes in turbulent regions where diffusion dominates in front of other phenomena.

- **Destruction of turbulence term** $(-C_{w1}\rho f_w\left(\frac{\widetilde{\nu}}{d}\right)^2)$**.**

  As it can be observed for the $"-"$ sign, this term makes the generated viscosity to decrease.

  When approaching walls in the geometry, the turbulence begins to reduce until being null right at the solid surface. This term represents this decrease. As it can be seen in its equation, the closer it is from the wall (d), the higher it is and so the reduction in total viscosity.

Since the release of Spalart-Allmaras turbulence model, it has suffered a lot of changes.

For instance, due to the fact that it was originally conceived for aerospace applications, a very wide field of knowledge, there have been many additions and modifications on its transport equation (adding or changing terms), on the constants of the model, etc..

However, in this project there will be implemented and applied the equations and constants presented before.

For further information about the Spalart-Allmaras turbulence model and its modifications for compressible flows go to [30], [31] and [32].

4.3 Symmetry-preserving discretization for compressible flows.

Although been able to simulate compressible flows gives countless possibilities and studies to be carried out, it also increases the difficulty enormously.

When simulating these kind of flows, people tend to use dissipative convective schemes (Upwind scheme for example) to make the simulation more stable [33]. However, this isn't so accurate from a mathematical point of view. The convective scheme should not dissipate energy.

Therefore, it is a better option to use kinetic energy preserving schemes. This is the case of Rozema [34].

In the publication, he proposes the idea of a new non-dissipative stable scheme for compressible flows. The modifications are made to the convective term of each Navier-Stokes equations. Next up are presented the mathematical development of each of them.

Original Mass Conservation equation.

$$\frac{\partial \rho}{\partial t} + \nabla \cdot (\rho \mathbf{u}) = 0 \tag{4.36}$$

Original Momentum Conservation equation.

$$\frac{\partial \rho \mathbf{u}}{\partial t} + \nabla \cdot (\rho \mathbf{u}\mathbf{u}) = -\nabla p + \nabla \cdot \tau \tag{4.37}$$

Original Energy Conservation equation.

$$\frac{\partial \rho e}{\partial t} + \nabla \cdot (\rho \mathbf{u} e) = -p \cdot \nabla \cdot u + \nabla q + \tau : \nabla u \tag{4.38}$$

As it can be seen in the previous equations, these are defined by the following variables.

$$\overrightarrow{g} = (\rho, \quad \rho \mathbf{u}, \quad \rho e)$$

However, the change that Rozema proposes in his paper consists on modifying these variables into the following.

$$\overrightarrow{h} = (\sqrt{\rho}, \quad \frac{\sqrt{\rho}\mathbf{u}}{\sqrt{2}}, \quad \sqrt{\rho e})$$

To maintain the mathematical equality between both ways to write the equations, the author puts forward the following modification for the convective term.

$$-\nabla \cdot (\mathbf{u}\phi) = -\frac{1}{2}\mathbf{u} \cdot \nabla \phi - \frac{1}{2}\nabla \cdot (\mathbf{u}\phi) \tag{4.39}$$

$$-\nabla \cdot (\mathbf{u}\phi) = c(\mathbf{u})\phi \tag{4.40}$$

For an structured and collocated mesh, the convective operator has this form. (See [paper Rozema] for the complete development).

$$(c(\mathbf{u})\phi)_k = \frac{1}{2}\phi_k \cdot \frac{1}{\Omega_k}\sum_f A_f\ \mathbf{u_f}\cdot\mathbf{n_f} - \frac{1}{\Omega_k}\sum_f A_f\ \mathbf{u_f}\cdot\mathbf{n_f}\ \frac{1}{2}(\phi_k + \phi_{nb(f)}) \tag{4.41}$$

Operating on the previous equation leads to the following expression for the convective term.

$$(c(\mathbf{u})\phi)_k = -\frac{1}{\Omega_k}\sum_f \frac{1}{2}A_f\ \mathbf{u_f}\cdot\mathbf{n_f}\ \phi_{nb(f)} \tag{4.42}$$

Modified Mass Conservation equation.

First, it is necessary to change the main variable of the equation ρ.

$$\frac{\partial\rho}{\partial t} = \frac{\partial(\sqrt{\rho}\cdot\sqrt{\rho})}{\partial t} \tag{4.43}$$

Now, applying the chain rule leads to the following.

$$\frac{\partial(\sqrt{\rho}\cdot\sqrt{\rho})}{\partial t} = \frac{\partial\sqrt{\rho}}{\partial t}\cdot\sqrt{\rho} + \sqrt{\rho}\cdot\frac{\partial\sqrt{\rho}}{\partial t} = 2\cdot\sqrt{\rho}\cdot\frac{\partial\sqrt{\rho}}{\partial t} \tag{4.44}$$

Since Mass Conservation equation only has the convective term as part of it, the modified equation states as presented next up.

$$\frac{\partial\rho}{\partial t} = 2\cdot\sqrt{\rho}\cdot\frac{\partial\sqrt{\rho}}{\partial t} = 2\cdot\sqrt{\rho_k}\cdot\left[-\frac{1}{\Omega_k}\sum_f \frac{1}{2}A_f\ \mathbf{u_f}\cdot\mathbf{n_f}\ \rho_{nb(f)}\right] \tag{4.45}$$

Finally, the new Mass Conservation equation states as the following.

$$\frac{\partial\rho}{\partial t} = -\frac{1}{\Omega_k}\sum_f A_f\ \mathbf{u_f}\cdot\mathbf{n_f}\ \sqrt{\rho_k}\sqrt{\rho_{nb(f)}} \tag{4.46}$$

Modified Momentum Conservation equation.

As in the previous case, it is necessary to change the variable and after that, applying the chain rule to the partial derivative.

$$\frac{\partial\rho\mathbf{u}}{\partial t} = \sqrt{2}\cdot\frac{\partial(\sqrt{\rho}\cdot\frac{\sqrt{\rho}\mathbf{u}}{\sqrt{2}})}{\partial t} \tag{4.47}$$

$$\sqrt{2}\cdot\frac{\partial(\sqrt{\rho}\cdot\frac{\sqrt{\rho}\mathbf{u}}{\sqrt{2}})}{\partial t} = \underbrace{\sqrt{2}\cdot\frac{\partial(\sqrt{\rho})}{\partial t}\cdot\frac{\sqrt{\rho}\mathbf{u}}{\sqrt{2}}}_{Term\ 1} + \underbrace{\sqrt{2}\cdot\sqrt{\rho}\cdot\frac{\partial(\frac{\sqrt{\rho}\mathbf{u}}{\sqrt{2}})}{\partial t}}_{Term\ 2} \tag{4.48}$$

Term 1.

$$\sqrt{2}\cdot\frac{\partial(\sqrt{\rho})}{\partial t}\cdot\frac{\sqrt{\rho}\mathbf{u}}{\sqrt{2}} = \sqrt{2}\cdot\left[-\frac{1}{\Omega_k}\sum_f\frac{1}{2}A_f\ \mathbf{u_f}\cdot\mathbf{n_f}\ \sqrt{\rho_{nb(f)}}\right]\cdot\frac{\sqrt{\rho_k}\mathbf{u_k}}{\sqrt{2}} \tag{4.49}$$
$$= -\frac{1}{\Omega_k}\sum_f\frac{1}{2}A_f\ \mathbf{u_f}\cdot\mathbf{n_f}\sqrt{\rho_{nb(f)}}\cdot\sqrt{\rho_k}\mathbf{u_k}$$

Term 2.

$$\sqrt{2}\cdot\sqrt{\rho}\cdot\frac{\partial(\frac{\sqrt{\rho}\mathbf{u}}{\sqrt{2}})}{\partial t} = \sqrt{2}\cdot\sqrt{\rho_k}\cdot\left[-\frac{1}{\Omega_k}\sum_f\frac{1}{2}A_f\ \mathbf{u_f}\cdot\mathbf{n_f}\ \frac{\sqrt{\rho_{nb(f)}}\mathbf{u_{nb(f)}}}{\sqrt{2}}-\frac{\nabla p}{\sqrt{2}\cdot\sqrt{\rho_k}}+\frac{\nabla\cdot\tau}{\sqrt{2}\cdot\sqrt{\rho_k}}\right] \tag{4.50}$$
$$= -\frac{1}{\Omega_k}\sum_f\frac{1}{2}A_f\ \mathbf{u_f}\cdot\mathbf{n_f}\ \sqrt{\rho_{nb(f)}}\cdot\sqrt{\rho_k}\cdot\mathbf{u_{nb(f)}}-\nabla p+\nabla\cdot\tau$$

Adding both terms leads to the following Momentum Conservation modified equation.

$$\frac{\partial\rho\mathbf{u}}{\partial t} = -\frac{1}{\Omega_k}\sum_f\frac{1}{2}A_f\ \mathbf{u_f}\cdot\mathbf{n_f}\ \sqrt{\rho_{nb(f)}}\cdot\sqrt{\rho_k}\cdot\frac{1}{2}\left(\mathbf{u_k}+\mathbf{u_{nb(f)}}\right)-\nabla p+\nabla\cdot\tau \tag{4.51}$$

Modified Energy Conservation equation.

In case of the Energy equation, the process is similar to the previous ones. First, it is needed to change the main variable and apply the chain rule to it.

$$\frac{\partial(\rho e)}{\partial t} = \frac{\partial(\sqrt{\rho e}\cdot\sqrt{\rho e})}{\partial t} \tag{4.52}$$

$$\frac{\partial(\sqrt{\rho e}\sqrt{\rho e})}{\partial t} = \frac{\partial(\sqrt{\rho e})}{\partial t}\cdot\sqrt{\rho e}+\sqrt{\rho e}\cdot\frac{\partial(\sqrt{\rho e})}{\partial t} = 2\cdot\sqrt{\rho e}\cdot\frac{\partial(\sqrt{\rho e})}{\partial t} \tag{4.53}$$

$$\frac{\partial(\rho e)}{\partial t} = 2\cdot\sqrt{\rho_k e_k}\cdot\left[-\frac{1}{\Omega_k}\sum_f\frac{1}{2}A_f\ \mathbf{u_f}\cdot\mathbf{n_f}\cdot\sqrt{\rho_{nb(f)}e_{nb(f)}}-\frac{p\cdot\nabla\mathbf{u}}{2\cdot\sqrt{\rho_k e_k}}+\frac{\tau:\nabla\mathbf{u}}{2\cdot\sqrt{\rho_k e_k}}-\frac{\nabla q}{2\cdot\sqrt{\rho_k e_k}}\right] \tag{4.54}$$

Finally, the modified Energy Conservation equation has the following expression.

$$\frac{\partial(\rho e)}{\partial t} = -\frac{1}{\Omega_k}\sum_f A_f\ \mathbf{u_f}\cdot\mathbf{n_f}\cdot\sqrt{\rho_{nb(f)}e_{nb(f)}}\ \sqrt{\rho_k e_k}-p\cdot\nabla\mathbf{u}+\tau:\nabla\mathbf{u}-\nabla q \tag{4.55}$$

As it can be seen in all of the equations developed previously, mathematically, the expressions are the same. However, this modifications ensure a symmetry-preserving discretization. For more details about this, see [paper Rozema].

4.4 Problem studied.

In order to give a better insight and ease the understanding of the simulation case and its numerical aspects for the turbulent regime study, it is presented next up in this section.

The codes developed for the study of the turbulence regime and the turbulence model methods are programmed in order to solve axisymmetric geometries.

As the reader may sense from its name, an axisymmetric geometry is the one that has complete symmetry on its central axis. The easiest case of this is a pipe (figure 4.5).

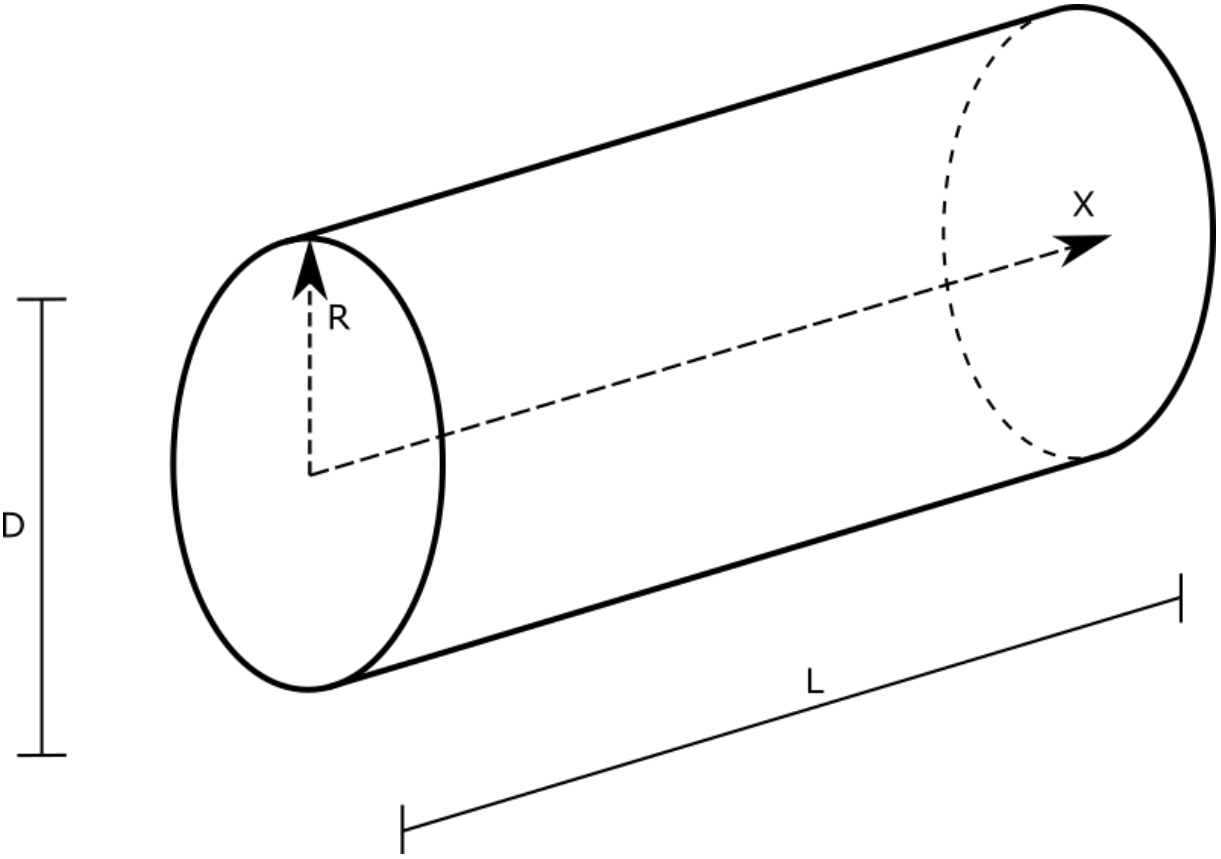

Figure 4.5: Pipe simulation case 3D scheme

The mesher of the codes are capable of creating a grid for endless axisymmetric geometries. It just need the mathematical expression of the radius as a function of the axial coordinate.

In this case, there has been selected as simulation case of study a constant radius pipe.

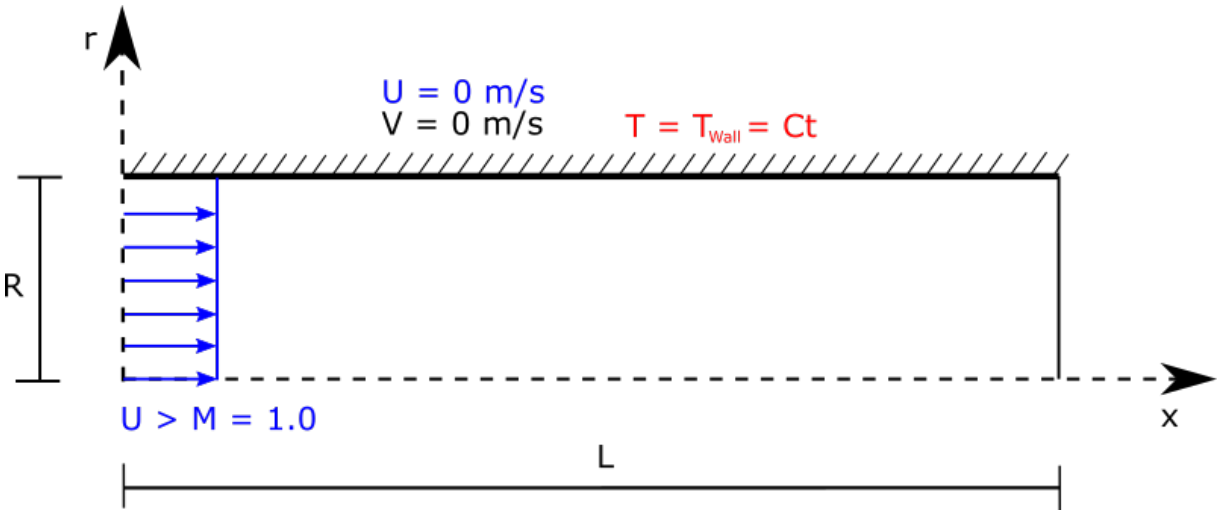

Figure 4.6: Turbulent regime pipe case scheme

As there can be seen in the scheme in image 4.6, the solid wall of the pipe has a non-slip condition for the flow, both axial (U) and radial (V) velocities are null.

Since the study case is said to be turbulent and supersonic, the inlet must have a velocity higher than the speed of sound (M $>$ 1.0). The imposed profile profile is constant, as it can be seen in figure 4.6. However, due to the non-slip condition, this quickly disappears into one with more parabolic tendency.

Although it may seem as a simple study case, it has a lot features and physical phenomena involved that is presented and deeply explained in turbulent regime results section (4.6).

4.5 Numerical framework.

In the present section there will be exposed all the turbulent regime studies numerical implementations. This comprises the spatial discretization of the axisymmetric cases, the modified Navier-Stokes compressible equations discretizations alongside the numerical implementation of the Spalart-Allmaras turbulence model and the time integration and resolution processes.

Since there are many aspects and features of turbulent regime numerical framework that are already present of the laminar one, there are many explanations that will be referred to that part of the thesis.

4.5.1 Spatial discretization.

As in every Computational Fluid Dynamics study, one of the crucial aspects is the mesh creation. Like in the laminar regime section, the fundamental basis for the grid development and equation's resolution is Finite Volume Method. However, there are important and significant differences between both meshes design.

The main modification may be the axisymmetricity. All the cases, that this turbulent regime project's codes are designed for, have a symmetric geometry with a central axis, for instance, a pipe.

As it is mentioned in the laminar regime part of the thesis, accurate simulation results can also be achieved despite using bi-dimensional condition, and so it happens in turbulent flow.

When simulating a case with that axisymmetric geometry, the main variation of the physical properties involved takes place at the axial and radial directions. And, when averaging the equations, the mean value of each variable in the azimuthal direction is null. Therefore, it would be a waste of computational resources and time to simulate flow behaviour in all axial, radial and azimuthal axis.

To avoid this to happen there has been chosen to develop an axisymmetric mesh. Its basis are similar to the grid design presented for the laminar regime cases.

However, the fact that the geometry has a mentioned central axis makes it a little bit different in terms of volume and surfaces computation.

Next up, in figure 4.7, it is presented the scheme of a control volume in a tri-dimensional mesh for a pipe.

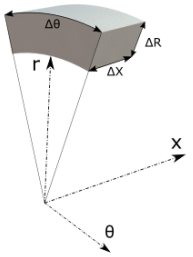

Figure 4.7: Tri-dimensional mesh control volume representation

As there can be seen in the representation (figure 4.7), apart from the axial and radial limits, there is an azimuthal division. This, although it is the most accurate way to mesh the geometry, isn't necessary at all. It increases dramatically the computational power required alongside the programming difficulty. Nevertheless, as it has been mentioned, obtained results doesn't differ severely from an axisymmetric option.

What has been made in this project to avoid this waste of resources is to remove the azimuthal axis from the meshing (figure 4.8).

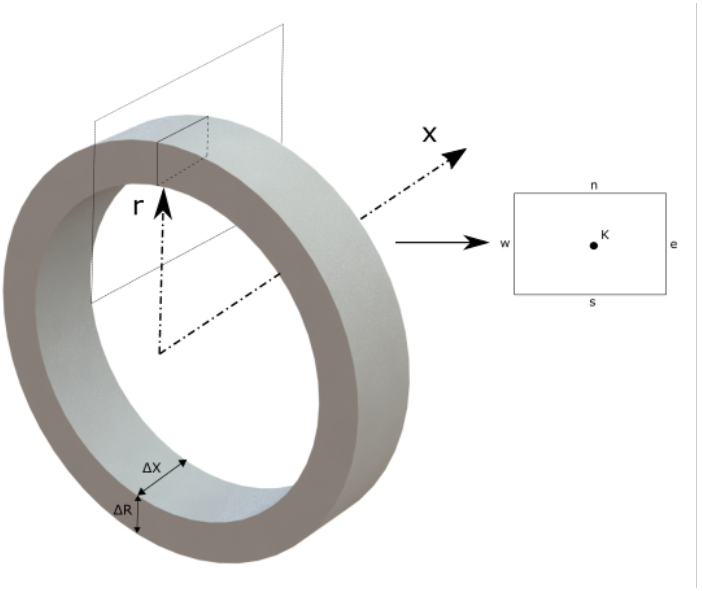

Figure 4.8: Axisymmetric mesh control volume representation

As there can be seen in the previous scheme, the geometry meshing is based on circular crowns.

Each control volume in figure 4.9 has actually that tri-dimensional shape. The complete geometry are formed by all of these placed together in the right positions.

On the one hand, it reduces significantly the amount of resources and eases the programming difficulty in terms of equations' resolution. However, it increases the meshing one. In this case, the surfaces and the volumes must be computed as revolution geometric entities, instead of just operating with node's coordinates.

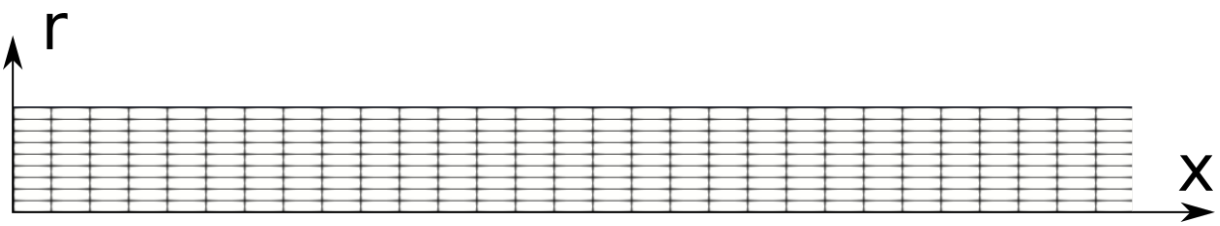

Figure 4.9: Spatial discretization of constant radius axisymmetric pipe

As it has been mentioned before in section 4.3, the chosen grid is an structured orthogonal/non-orthogonal collocated mesh (section 3.2.1 for more information).

This collocated mesh reduces the total number of grids from 3 to 1. It places all the main physical properties (density, velocity, pressure...) at the control volume's centred node.

Since it was already implemented in the laminar regime mesher code, in case of turbulent simulations, there has been chosen to use the same grid spacing type to take advantage of its strengths. It is a perfect way to divide the geometry alongside its numerous possibilities of different mesh distributions (section 3.2.1).

Previously, there has been mentioned the fact that the chosen grid is an structured orthogonal/non-orthogonal mesh. This is another new feature from turbulent regime codes in front of laminar ones.

Since one of the aims o this project coding is to make it generic in order to be able to simulate as many cases as possible, there has been added the possibility to create an orthogonal and non-orthogonal mesh depending on the case needs.

Instead of setting an arbitrary geometry on the codes' inputs, the program is designed to introduce an axial length and a user-defined mathematical expression that gives the local radius as a function of the axial coordinate. This, although it increases a little the coding difficulty, it allows to mesh a lot more different geometries.

Imagine a geometry with a constant radius, in that case, the resultant grid would be orthogonal, all the nodes would have the same shape despite size changes due to nodal distribution. However, if the simulation geometry has a variable radius, there will be some parts of the mesh in which certain volumes would have to represent this radius change. In that case, these won't have the same shape as in constant radius parts of the geometry.

Once this mathematical equation is completed, it is only needed to decide the type of nodal distribution (section 3.2.1) and the program meshes it completely. This simply addition allows to simulate countless geometries with no need for a huge readjustment of the codes' mesher.

And, since there can be many different cases with different geometries and nodal spacing needs, it is also necessary to implement again different mathematical distributions for control volumes (regular, hyperbolic tangent, etc..).

For instance, in case of simulating a constant radius pipe, a good choice for the axial and radial nodal distribution could be regular and hyperbolic tangent or sine respectively.

In the first direction there are only a flow inlet and outlet, there is no need for a special node distribution due to flow conditions. However, on the radial axis there is a solid wall on the upper part (the pipe wall) with non-slip boundary condition. And, as it was explained in section 3.2.1, it is a good choice to place a higher number of nodes near it, and a great way to do that is choosing of the mentioned nodal distributions.

4.5.2 Modified compressible Navier Stokes equations discretization.

In this section is exposed the numerical discretization of the compressible Navier-Stokes modified equations presented before. These have been developed following the basis of Finite Volume Method applied to the spatial discretization shown in section 4.5.1.

Since this is an axisymmetric study, there will be only presented the discretization of the necessary expressions to do the simulations [35]. Azimuthal axis equations won't be exposed or explained.

Divergence Theorem.

Before presenting all the discretization for the equations, it is necessary to explain one of the important mathematical laws these discretizations are based in.

As the reader can observe in sections 4.2.1 and 4.3, to solve the equations it is needed to compute many gradients and divergences. To do that, as its name suggests, Divergence Theorem is going to be used. However, the fact of working on cylindrical coordinates makes it a little bit different from Cartesian systems.

As it is already explained at the beginning of in section 3.2.4, in FVM, the Divergence or Stokes' theorem states the following.

$$(\nabla \cdot \Phi) = \frac{1}{\Omega} \sum_f A_f \Phi_f \mathbf{n} \tag{4.56}$$

In a bi-dimensional, regular grid, with Cartesian coordinate system, the operation $(\nabla \cdot \Phi)$ represents the sum of the variable derivatives in the both axis.

$$(\nabla \cdot \Phi) = \frac{\partial \Phi}{\partial x} + \frac{\partial \Phi}{\partial y} \tag{4.57}$$

This happens because, in mentioned grid system, parallel surfaces are equal (West-East, North-South).

Nevertheless, this isn't true in a regular grid with cylindrical coordinate system. North surface has a higher radius than South one, and so a bigger surface.

This fact modifies a little bit previous equation.

$$(\nabla \cdot \Phi) = \frac{\partial \Phi}{\partial x} + \frac{\partial \Phi}{\partial r} + \frac{\Phi}{r} \tag{4.58}$$

The difference between the surfaces makes an additional $\frac{\Phi}{r}$ term to appear. However, this term is bonded with the radial gradient.

For instance, to compute the axial gradient of a variable Φ, Divergence theorem can be applied without any changes.

$$\frac{\partial \Phi}{\partial x} = \frac{1}{\Omega} \sum_f A_f \Phi_f n x_f \tag{4.59}$$

Nevertheless, in case of calculating the gradient in the radial direction is where this modification appears [36].

$$\frac{\partial \Phi}{\partial r} = \frac{1}{\Omega} [\sum_f A_f \Phi_f n r_f] - \frac{\Phi}{r} \tag{4.60}$$

Before continuing to the discretized equations, it is necessary to mentioned a little feature added to the turbulent regime codes.

Since one of the objectives of these project is to develop programs able simulate many different axisymmetric geometry cases, one of the aims must be to make it as generic as possible. Due to that decision, the equations' discretization for the turbulent regime are all implemented with a new feature in terms of surface's normals calculation, which, at the same time, eases the programming difficulty.

The terms nx_f and nr_f on the previous equations (4.59) and (4.60) are the two components of the surfaces normal vectors (**n**). These are computed as the cosinus and sinus of its angle plus the angle between face normal and horizontal/vertical axis.

In order to give a better insight of this, it is presented in figure 4.10 a simplified scheme of it.

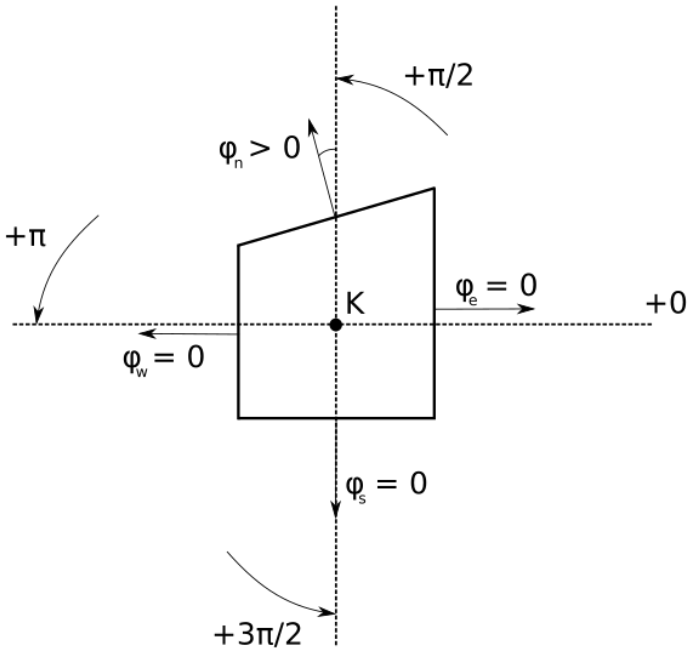

Figure 4.10: Surfaces' normal vectors scheme

For instance, the normal vector components for the North surface of the scheme are the following.

$$\mathbf{n} = (nx, \quad ny) = (cos(\frac{\pi}{2} + \varphi_n), \quad sin(\frac{\pi}{2} + \varphi_n))$$

- **Discretization of the Mass Conservation equation.**

  The discretization is the Mass Conservation equation doesn't represent a great challenge in comparison to the others, and so the computational power required for it. However, it is because of solving this, simulating compressible regime that equations change dramatically from the ones discretized in the laminar case.

$$\frac{\partial \rho}{\partial t} = \underbrace{\underbrace{-\frac{1}{\Omega_k}\sum_f A_f \, \mathbf{u_f} \cdot \mathbf{n_f} \, \sqrt{\rho_k}\sqrt{\rho_{nb(f)}}}_{Convective \;\; Term \;\; (c(\mathbf{u})\rho)_k}}_{F(\rho)}$$

  Convective term.

$$
\begin{aligned}
(c(\mathbf{u})\rho)_k \;=\; & -\frac{1}{\Omega_K}\cdot\Bigg[A_w\cdot\sqrt{\rho_K}\cdot\sqrt{\rho_W}\,[u_w\cdot cos(\pi+\varphi_w)+v_w\cdot sin(\pi+\varphi_w)] \\
& +A_e\cdot\sqrt{\rho_K}\cdot\sqrt{\rho_E}\,[u_e\cdot cos(\varphi_e)+v_e\cdot sin(\varphi_e)] \\
& +A_s\cdot\sqrt{\rho_K}\cdot\sqrt{\rho_S}\left[u_s\cdot cos(\frac{3\pi}{2}+\varphi_s)+v_s\cdot sin(\frac{3\pi}{2}+\varphi_s)\right] \\
& +A_n\cdot\sqrt{\rho_K}\cdot\sqrt{\rho_N}\left[u_n\cdot cos(\frac{\pi}{2}+\varphi_n)+v_n\cdot sin(\frac{\pi}{2}+\varphi_n)\right]\Bigg]
\end{aligned}
\tag{4.61}
$$

- **Discretization of the Axial Momentum Conservation equation.**

  As in the previous case, the discretized equation has already been developed before. However, this time, it has other terms apart from the convective.

$$
\frac{\partial\rho u}{\partial t}=\underbrace{\underbrace{-\frac{1}{\Omega_k}\sum_f\frac{1}{2}A_f\,\mathbf{u_f}\cdot\mathbf{n_f}\,\sqrt{\rho_{nb(f)}}\cdot\sqrt{\rho_k}\cdot\frac{1}{2}\,(u_k+u_{nb(f)})}_{Convective\ \ Term\ \ (c(\mathbf{u})u)_k}-\underbrace{\frac{\partial p}{\partial x}}_{Pressure\ \ gradient}+\underbrace{\nabla\cdot\tau|_u}_{Diffusive\ \ Term}}_{F(u)}
$$

  Convective term.

$$
\begin{aligned}
(c(\mathbf{u})u)_k \;=\; & -\frac{1}{\Omega_K}\cdot\Bigg[A_w\sqrt{\rho_K}\sqrt{\rho_W}\,[u_w\cdot cos(\pi+\varphi_w)+v_w\cdot sin(\pi+\varphi_w)]\cdot\frac{1}{2}(u_K+u_W) \\
& +A_e\sqrt{\rho_K}\sqrt{\rho_E}\,[u_e\cdot cos(\varphi_e)+v_e\cdot sin(\varphi_e)]\cdot\frac{1}{2}(u_K+u_E) \\
& +A_s\sqrt{\rho_K}\sqrt{\rho_S}\left[u_s\cdot cos(\frac{3\pi}{2}+\varphi_s)+v_s\cdot sin(\frac{3\pi}{2}+\varphi_s)\right]\cdot\frac{1}{2}(u_K+u_S) \\
& +A_n\sqrt{\rho_K}\sqrt{\rho_N}\left[u_n\cdot cos(\frac{\pi}{2}+\varphi_n)+v_n\cdot sin(\frac{\pi}{2}+\varphi_n)\right]\cdot\frac{1}{2}(u_K+u_N)\Bigg]
\end{aligned}
\tag{4.62}
$$

  Pressure gradient.

  In this case, the discretized term is the pressure gradient on the axial direction. Therefore, as it has been explained at the beginning of the section, it isn't necessary to subtract the additional term due to cylindrical coordinate system.

$$
\begin{aligned}
\frac{\partial p}{\partial x} \;=\; & \frac{1}{\Omega_K}\cdot\Bigg[A_w\cdot P_w\cdot cos(\pi+\varphi_w)+A_e\cdot P_e\cdot cos(\varphi_e) \\
& +A_s\cdot P_s\cdot cos(\frac{3\pi}{2}+\varphi_s)+A_n\cdot P_n\cdot cos(\frac{\pi}{2}+\varphi_n)\Bigg]
\end{aligned}
\tag{4.63}
$$

Viscous stress.

To see the mathematical development of this term of the momentum equation go to appendix G in Annex document of this project. Additionally, the numerical discretization of all stress term (τ) can be found in appendix H of the same document.

$$\nabla \cdot \tau|_u = \frac{\partial \tau_{xx}}{\partial x} + \underbrace{\frac{\partial \tau_{xr}}{\partial r} + \frac{\tau_{xr}}{\tau_{xr}}}_{\nabla \cdot \tau_{xr}}$$

$$\begin{aligned} \nabla \cdot \tau|_u \;=\; & \frac{1}{\Omega_K} \cdot \Big[A_w \cdot [\tau_{xx}|_w \cdot cos(\pi + \varphi_w) + \tau_{xr}|_w \cdot sin(\pi + \varphi_w)] \\ & + A_e \cdot [\tau_{xx}|_e \cdot cos(\varphi_e) + \tau_{xr}|_e \cdot sin(\varphi_e)] \\ & + A_s \cdot [\tau_{xx}|_s \cdot cos(\frac{3\pi}{2} + \varphi_s) + \tau_{xr}|_s \cdot sin(\frac{3\pi}{2} \varphi_s)] \\ & + A_n \cdot [\tau_{xx}|_n \cdot cos(\frac{3\pi}{2} + \varphi_n) + \tau_{xr}|_n \cdot sin(\frac{3\pi}{2} \varphi_n)] \Big] \end{aligned} \tag{4.64}$$

- **Discretization of the Radial Momentum Conservation equation.**

$$\frac{\partial \rho v}{\partial t} = \underbrace{\underbrace{-\frac{1}{\Omega_k} \sum_f \frac{1}{2} A_f \, \mathbf{u_f} \cdot \mathbf{n_f} \, \sqrt{\rho_{nb(f)}} \cdot \sqrt{\rho_k} \cdot \frac{1}{2} \, (v_k + v_{nb(f)})}_{Convective \;\; Term \;\; (c(\mathbf{u})v)_k} - \underbrace{\frac{\partial p}{\partial r}}_{Pressure \;\; gradient} + \underbrace{\nabla \cdot \tau|_r}_{Diffusive \;\; Term}}_{F(v)} \tag{4.65}$$

Convective term.

$$\begin{aligned} (c(\mathbf{u})v)_k \;=\; & -\frac{1}{\Omega_K} \cdot \Big[A_w \sqrt{\rho_K} \sqrt{\rho_W} \, [u_w \cdot cos(\pi + \varphi_w) + v_w \cdot sin(\pi + \varphi_w)] \cdot \frac{1}{2} (v_K + v_W) \\ & + A_e \sqrt{\rho_K} \sqrt{\rho_E} \, [u_e \cdot cos(\varphi_e) + v_e \cdot sin(\varphi_e)] \cdot \frac{1}{2} (v_K + v_E) \\ & + A_s \sqrt{\rho_K} \sqrt{\rho_S} \left[u_s \cdot cos(\frac{3\pi}{2} + \varphi_s) + v_s \cdot sin(\frac{3\pi}{2} + \varphi_s) \right] \cdot \frac{1}{2} (v_K + v_S) \\ & + A_n \sqrt{\rho_K} \sqrt{\rho_N} \left[u_n \cdot cos(\frac{\pi}{2} + \varphi_n) + v_n \cdot sin(\frac{\pi}{2} + \varphi_n) \right] \cdot \frac{1}{2} (v_K + v_N) \Big] \end{aligned} \tag{4.66}$$

Pressure gradient.

Here, in this term discretization, there can be seen a perfect example of the application of the mentioned modification for the Divergence theorem in cylindrical coordinates.

$$\frac{\partial p}{\partial r} = \frac{1}{\Omega_K}\cdot\Big[A_w\cdot P_w\cdot sin(\pi+\varphi_w)+A_e\cdot P_e\cdot sin(\varphi_e) \\ +A_s\cdot P_s\cdot sin(\frac{3\pi}{2}+\varphi_s)+A_n\cdot P_n\cdot sin(\frac{\pi}{2}+\varphi_n)\Big]-\frac{P_K}{R_K} \tag{4.67}$$

Viscous stress.

As in case of the axial momentum conservation, the mathematical development of the viscous stress term can be found in appendix G in Annex document of this project.

$$\nabla\cdot\tau|_r = \frac{\partial\tau_{rx}}{\partial x}+\underbrace{\frac{\partial\tau_{rr}}{\partial r}+\frac{\tau_{rr}}{\tau_{xr}}}_{\nabla\cdot\tau_{xr}}-\frac{\tau_{\theta\theta}}{r}$$

$$\nabla\cdot\tau|_r = \frac{1}{\Omega_K}\cdot\Big[A_w\cdot[\tau_{rx}|_w\cdot cos(\pi+\varphi_w)+\tau_{rr}|_w\cdot sin(\pi+\varphi_w)] \\ +A_e\cdot[\tau_{rx}|_e\cdot cos(\varphi_e)+\tau_{rr}|_e\cdot sin(\varphi_e)] \\ +A_s\cdot[\tau_{rx}|_s\cdot cos(\frac{3\pi}{2}+\varphi_s)+\tau_{rr}|_s\cdot sin(\frac{3\pi}{2}\varphi_s)] \\ +A_n\cdot[\tau_{rx}|_n\cdot cos(\frac{3\pi}{2}+\varphi_n)+\tau_{rr}|_n\cdot sin(\frac{3\pi}{2}\varphi_n)]\Big]-\frac{\tau_{\theta\theta}|_K}{R_K} \tag{4.68}$$

- **Discretization of the Energy Conservation equation.**

$$\frac{\partial\rho e}{\partial t} = \underbrace{\underbrace{-\frac{1}{\Omega_k}\sum_f\frac{1}{2}A_f\,\mathbf{u_f}\cdot\mathbf{n_f}\sqrt{\rho_{nb(f)e_{nb(f)}}}\cdot\sqrt{\rho_k e_k}}_{Convective\ \ Term\ \ (c(\mathbf{u})e)_k}-\underbrace{p\dot{\nabla}\mathbf{u}}_{Pressure\ \ dissipation}-\underbrace{\nabla q}_{Thermal\ \ conduction}+\underbrace{\tau:\nabla\mathbf{u}}_{Viscous\ \ dissipation}}_{F(e)} \tag{4.69}$$

Convective term.

$$(c(\mathbf{u})e)_k = -\frac{1}{\Omega_K}\cdot\Big[A_w\cdot\sqrt{\rho_K e_K}\cdot\sqrt{\rho_W e_W}\,[u_w\cdot cos(\pi+\varphi_w)+v_w\cdot sin(\pi+\varphi_w)] \\ +A_e\cdot\sqrt{\rho_K e_K}\cdot\sqrt{\rho_E e_E}\,[u_e\cdot cos(\varphi_e)+v_e\cdot sin(\varphi_e)] \\ +A_s\cdot\sqrt{\rho_K e_K}\cdot\sqrt{\rho_S e_S}\Big[u_s\cdot cos(\frac{3\pi}{2}+\varphi_s)+v_s\cdot sin(\frac{3\pi}{2}+\varphi_s)\Big] \\ +A_n\cdot\sqrt{\rho_K e_K}\cdot\sqrt{\rho_N e_N}\Big[u_n\cdot cos(\frac{\pi}{2}+\varphi_n)+v_n\cdot sin(\frac{\pi}{2}+\varphi_n)\Big]\Big] \tag{4.70}$$

Pressure dissipation term.

$$
\begin{aligned}
p\cdot(\nabla\cdot\mathbf{u}) \;=\; & P_K\cdot\frac{1}{\Omega_K}\cdot\Big[A_w\cdot[u_w\cdot cos(\pi+\varphi_w)+v_w\cdot sin(\pi+\varphi_w)] \\
& +A_e\cdot[u_e\cdot cos(\varphi_e)+v_e\cdot sin(\varphi_e)] \\
& +A_s\cdot[u_s\cdot cos(\frac{3\pi}{2}+\varphi_s)+v_s\cdot sin(\frac{3\pi}{2}+\varphi_s)] \\
& +A_n\cdot[u_n\cdot cos(\frac{\pi}{2}+\varphi_n)+v_n\cdot sin(\frac{\pi}{2}+\varphi_n)]\Big]
\end{aligned}
\tag{4.71}
$$

Thermal conduction.

$$
\begin{aligned}
\nabla\cdot q \;=\; & \frac{1}{\Omega_K}\cdot\Big[A_w\cdot K_w\cdot\frac{T_K-T_W}{d_{KW}}\cdot cos(\pi+\varphi_w)+A_e\cdot K_e\cdot\frac{T_E-T_K}{d_{KE}}\cdot cos(\varphi_e) \\
& +A_s\cdot K_s\cdot\frac{T_K-T_S}{d_{KS}}\cdot sin(\frac{3\pi}{2}+\varphi_s)+A_n\cdot K_n\cdot\frac{T_N-T_K}{d_{KN}}\cdot sin(\frac{\pi}{2}+\varphi_n)\Big]
\end{aligned}
\tag{4.72}
$$

Viscous energy dissipation.

The mathematical development of this term of the Energy Conservation equation and the strain stress terms (τ) numerical discretization are presented in appendixes G and H of the Annex document of this project respectively.

$$
\tau:\nabla\mathbf{u}=\tau_{rr}\cdot\frac{\partial v}{\partial r}+\tau_{rz}\cdot\frac{\partial v}{\partial x}+\tau_{\theta\theta}\cdot\frac{v}{r}+\tau_{zr}\cdot\frac{\partial u}{\partial r}+\tau_{zz}\cdot\frac{\partial u}{\partial x}
$$

$$
\begin{aligned}
\tau : \nabla \mathbf{u} \quad = \quad & \tau_{rr}|_K \cdot \left\{ \frac{1}{\Omega_K} \cdot \left[A_w \cdot v_w \cdot sin(\pi + \varphi_w) + A_e \cdot v_e \cdot sin(\varphi_e) \right.\right. \\
& \left.\left. + A_s \cdot v_s \cdot sin(\frac{3\pi}{2} + \varphi_s) + A_n \cdot v_n \cdot sin(\frac{\pi}{2} + \varphi_n) \right] - \frac{v_K}{R_K} \right\} \\
& + \tau_{rz}|_K \cdot \left\{ \frac{1}{\Omega_K} \cdot \left[A_w \cdot v_w \cdot cos(\pi + \varphi_w) + A_e \cdot v_e \cdot cos(\varphi_e) \right.\right. \\
& \left.\left. + A_s \cdot v_s \cdot cos(\frac{3\pi}{2} + \varphi_s) + A_n \cdot v_n \cdot cos(\frac{\pi}{2} + \varphi_n) \right] \right\} \\
& + \tau_{\theta\theta}|_K \cdot \frac{v_K}{R_K} \\
& + \tau_{zr}|_K \cdot \left\{ \frac{1}{\Omega_K} \cdot \left[A_w \cdot u_w \cdot sin(\pi + \varphi_w) + A_e \cdot u_e \cdot sin(\varphi_e) \right.\right. \\
& \left.\left. + A_s \cdot u_s \cdot sin(\frac{3\pi}{2} + \varphi_s) + A_n \cdot u_n \cdot sin(\frac{\pi}{2} + \varphi_n) \right] - \frac{u_K}{R_K} \right\} \\
& + \tau_{zz}|_K \cdot \left\{ \frac{1}{\Omega_K} \cdot \left[A_w \cdot u_w \cdot cos(\pi + \varphi_w) + A_e \cdot u_e \cdot cos(\varphi_e) \right.\right. \\
& \left.\left. + A_s \cdot u_s \cdot cos(\frac{3\pi}{2} + \varphi_s) + A_n \cdot u_n \cdot cos(\frac{\pi}{2} + \varphi_n) \right] \right\}
\end{aligned} \tag{4.73}
$$

- **Discretization of the Pressure equation.**

  Following the same mathematical expression shown for ideal gases in section 4.1.1 allows to obtained pressure's discretization.

$$P_K = \rho_K \cdot R \cdot T_K \tag{4.74}$$

4.5.3 Spalart-Allmaras RANS turbulence model implementation.

To make it easier for the reader, next up will be presented again the Spalart-Allmaras transport equation.

$$
\frac{\partial \rho \widetilde{\nu}}{\partial t} + \underbrace{\nabla \cdot (\rho \widetilde{\nu} \mathbf{u})}_{Convective\ \ Term} = \underbrace{C_{b1} \widetilde{S} \rho \widetilde{\nu}}_{Production\ \ Term} + \underbrace{\frac{1}{\sigma} \nabla((\mu + \rho \widetilde{\nu}) \cdot \nabla \widetilde{\nu})}_{Diffusive\ \ linear\ \ Term} \underbrace{+ \frac{C_{b2}}{\sigma} \nabla \widetilde{\nu} \cdot \nabla \widetilde{\nu}}_{Diffusive\ \ non-linear\ \ Term} \underbrace{- C_{w1} \rho f_w \left(\frac{\widetilde{\nu}}{d} \right)^2}_{Destruction\ \ Term}
$$

In this section will only be presented the numerical Finite Volume Method discretization for the Spalart-Allmaras transport equation terms. In order to see the discretization of the rest of the different parameters needed go to appendix F in Annex document of this project.

- **Discretization of the convective term.**

  Unlike the modified Mass, Momentum and Energy conservation equations shown in section 4.3, the discretization of the convective term is equal to the one explained in the laminar regime part of this thesis (section 3.2.4). The only minor difference between them is that, in first case, the coordinate system was Cartesian, while this time it is cylindrical. However, this only affects in small aspects like control volume surfaces difference between lower and upper limits.

  Applying the Finite Volume Method basis and Stokes theorem leads to the following numerical expression of the equation.

$$\begin{aligned}\nabla\cdot(\rho\widetilde{\nu}\mathbf{u}) \;=\; & \frac{1}{\Omega_K}\cdot\Big[A_w\cdot\rho_w\cdot\widetilde{\nu_w}\cdot(u_w\cdot cos(\pi+\varphi_w)+v_w\cdot sin(\pi+\varphi_w)) \\ & +A_e\cdot\rho_e\cdot\widetilde{\nu}_e\cdot(u_e\cdot cos(\varphi_e)+v_e\cdot sin(\varphi_e)) \\ & +A_s\cdot\rho_s\cdot\widetilde{\nu}_s\cdot(u_s\cdot cos(\frac{3\pi}{2}+\varphi_s)+v_s\cdot sin(\frac{3\pi}{2}+\varphi_s)) \\ & +A_n\cdot\rho_n\cdot\widetilde{\nu}_n\cdot(u_n\cdot cos(\frac{\pi}{2}+\varphi_n)+v_n\cdot sin(\frac{\pi}{2}+\varphi_n))\Big]\end{aligned} \tag{4.75}$$

- **Discretization of the production term.**

  As it can be seen in its equation, production term doesn't represent a great challenge from the point of view of the discretization. There is Nabla operators (∇) such as divergence or gradient.

  The only difficulty may be the computation of extra parameters like $\widetilde{S}$.

$$C_{b1}\widetilde{S}\rho\widetilde{\nu} = C_{b1}\cdot\widetilde{S_K}\cdot\rho_K\cdot\widetilde{\nu_K} \tag{4.76}$$

- **Discretization of the diffusive linear term.**

  The discretization of this term is similar to the one exposed for the diffusive term in Momentum and Energy conservation equations in laminar regime (section 3.2.4).

  The only minor difference may be again, the switch from Cartesian to cylindrical coordinate system in terms of control volume surfaces.

  Once again, applying the Finite Volume Method discretization basis and Stokes theorem for the Divergence operator leads to the following discretized equation.

$$\frac{1}{\sigma}\nabla((\mu+\rho\widetilde{\nu})\cdot\nabla\widetilde{\nu}) = \frac{1}{\Omega_K}\cdot\left[A_w\cdot(\mu_w+\rho_w\widetilde{\nu_w})\cdot\frac{\widetilde{\nu_K}-\widetilde{\nu_W}}{d_{KW}}\cdot cos(\pi+\varphi_w)\right. \quad (4.77)$$
$$+A_e\cdot(\mu_e+\rho_e\widetilde{\nu}_e)\cdot\frac{\widetilde{\nu_E}-\widetilde{\nu_K}}{d_{KE}}\cdot cos(\varphi_e)$$
$$+A_s\cdot(\mu_s+\rho_s\widetilde{\nu}_s)\cdot\frac{\widetilde{\nu_K}-\widetilde{\nu_S}}{d_{KS}}\cdot sin(\frac{3\pi}{2}+\varphi_s)$$
$$\left.+A_n\cdot(\mu_n+\rho_n\widetilde{\nu}_n)\cdot\frac{\widetilde{\nu_N}-\widetilde{\nu_K}}{d_{KN}}\cdot sin(\frac{\pi}{2}+\varphi_n)\right]$$

- **Discretization of the diffusive non-linear term.**

  This term of the Spalart-Allmaras transport equation has a certain peculiarity. Until now, in order to simplify the equations, every gradient has been expressed as an scalar value which depends only on the two node variables involved.

  However, the gradient operator is actually a vector with 1, 2 or 3 components depending if the study is uni, bi or tri-dimensional.

$$\nabla\phi = \left(\frac{\partial\phi}{\partial x},\ \frac{\partial\phi}{\partial y},\ \frac{\partial\phi}{\partial z}\right) \quad (4.78)$$

  So, mathematically, the operation $\nabla\phi\cdot\nabla\phi$ is a scalar product between both vectors. This leads to the following result (for bi-dimensional cylindrical coordinates).

$$\nabla\phi\cdot\nabla\phi = \frac{\partial\phi}{\partial x}\cdot\frac{\partial\phi}{\partial x}+\frac{\partial\phi}{\partial r}\cdot\frac{\partial\phi}{\partial r} = \left(\frac{\partial\phi}{\partial x}\right)^2+\left(\frac{\partial\phi}{\partial r}\right)^2 \quad (4.79)$$

  It also needs to be mentioned that, in this case, the gradients are referred to the control volume, not its faces. This means, it is necessary to apply the already explained Divergence-Gradient mathematical relationship for the radial direction gradients.

$$\begin{aligned}\frac{C_{b2}}{\sigma}\nabla\widetilde{\nu}\cdot\nabla\widetilde{\nu} &= Cb2\cdot\left\{\left[\frac{1}{\Omega_K}\cdot[A_w\cdot\widetilde{\nu_w}\cdot cos(\pi+\varphi_w)\right.\right. \\ &+A_e\cdot\widetilde{\nu}_e\cdot cos(\varphi_e) \\ &+A_s\cdot\widetilde{\nu}_s\cdot cos(\frac{3\pi}{2}+\varphi_s) \\ &\left.+A_n\cdot\widetilde{\nu}_n\cdot cos(\frac{\pi}{2}+\varphi_n)]\right]^2 \\ &+\left[\frac{1}{\Omega_K}\cdot[A_w\cdot\widetilde{\nu_w}\cdot sin(\pi+\varphi_w)\right. \\ &+A_e\cdot\widetilde{\nu}_e\cdot sin(\varphi_e) \\ &+A_s\cdot\widetilde{\nu}_s\cdot sin(\frac{3\pi}{2}+\varphi_s) \\ &\left.\left.+A_n\cdot\widetilde{\nu}_n\cdot sin(\frac{\pi}{2}+\varphi_n)]-\frac{\widetilde{\nu_K}}{R_K}\right]^2\right\}\end{aligned} \tag{4.80}$$

- **Discretization of the destruction term.**

  As in the case of the production term, the discretization of the destruction one is very straight and easy in comparison with other ones like the previous one.

  Again, the only aspect to take into account is that is is necessary to compute certain secondary parameters before calculating this term.

$$-C_{w1}\rho f_w\left(\frac{\widetilde{\nu}}{d}\right)^2=-C_{w1}\cdot\rho\cdot f_{w_K}\left(\frac{\widetilde{\nu_K}}{d_K}\right)^2 \tag{4.81}$$

Once all this terms have been determined separately, it is necessary to add them all.

$$F(\widetilde{\nu})=-\nabla\cdot(\rho\widetilde{\nu}\mathbf{u})+C_{b1}\widetilde{S}\rho\widetilde{\nu}+\frac{1}{\sigma}[\nabla((\mu+\rho\widetilde{\nu})\cdot\nabla\widetilde{\nu})+C_{b2}\nabla\widetilde{\nu}\cdot\nabla\widetilde{\nu}]-C_{w1}\rho f_w\left(\frac{\widetilde{\nu}}{d}\right)^2 \tag{4.82}$$

Then, $\widetilde{\nu}^{n+1}$ is determined as a function of $\widetilde{\nu}^n$, $\widetilde{\nu}^{n-1}$, $F(\widetilde{\nu})^{n-1}$ and $F(\widetilde{\nu})^n$. (Explained in a more detailed way in the next section).

Now, it is only needed to compute the following parameters.

$$X^{n+1}=\frac{\widetilde{\nu}^{n+1}}{\nu^{n+1}}\longrightarrow f_{v1}^{n+1}=\frac{(X^{n+1})^3}{(X^{n+1})^3+C_{v1}^3} \tag{4.83}$$

And finally, it is possible to determine the turbulent dynamic viscosity that will be added to the normal viscosity.

$$\mu_t^{n+1} = \widetilde{\nu}^{n+1} \cdot \rho^{n+1} \cdot f_{v1}^{n+1} \tag{4.84}$$

4.5.4 Time integration.

The time integration method used for the turbulent regime study doesn't differ so much from the one of the laminar regime apart from certain changes.

The main similarity between both processes is that, as in the laminar case, in the turbulent study an explicit time integration method is used (section 3.2.3).

However, this time, instead of using a fixed Adam-Bashforth method, it has been chosen to implement a slightly change [37].

$$\phi^{n+1} = \frac{2 \cdot \beta_{Time} \cdot \phi^n - (\beta_{Time} - 0.50) \cdot \phi^{n-1}}{\beta_{Time} + 0.50} + \Delta t \cdot [(1 + \beta_{Time}) \cdot F(\phi)^n - \beta_{Time} \cdot F(\phi)^{n-1}] \tag{4.85}$$

Thanks to this tiny change in the time integration, it is possible to select the weight that each time step may have on the future value of the property.

Next up is presented the time integration expressions for the main physical properties of the simulation.

Density.

$$\rho^{n+1} = \frac{2 \cdot \beta_{Time} \cdot \rho^n - (\beta_{Time} - 0.50) \cdot \rho^{n-1}}{\beta_{Time} + 0.50} + \Delta t \cdot \left[(1 + \beta_{Time}) \cdot F(\rho)^n - \beta_{Time} \cdot F(\rho)^{n-1}\right] \tag{4.86}$$

Axial velocity.

$$u^{n+1} = \frac{2 \cdot \beta_{Time} \cdot u^n - (\beta_{Time} - 0.50) \cdot u^{n-1}}{\beta_{Time} + 0.50} + \Delta t \cdot \left[(1 + \beta_{Time}) \cdot \frac{F(u)^n}{\rho^n} - \beta_{Time} \cdot \frac{F(u)^{n-1}}{\rho^{n-1}}\right] \tag{4.87}$$

Radial velocity.

$$v^{n+1} = \frac{2 \cdot \beta_{Time} \cdot v^n - (\beta_{Time} - 0.50) \cdot v^{n-1}}{\beta_{Time} + 0.50} + \Delta t \cdot \left[(1 + \beta_{Time}) \cdot \frac{F(v)^n}{\rho^n} - \beta_{Time} \cdot \frac{F(v)^{n-1}}{\rho^{n-1}}\right] \tag{4.88}$$

Internal energy.

$$e^{n+1} = \frac{2 \cdot \beta_{Time} \cdot e^n - (\beta_{Time} - 0.50) \cdot e^{n-1}}{\beta_{Time} + 0.50} + \Delta t \cdot \left[(1 + \beta_{Time}) \cdot \frac{F(e)^n}{\rho^n} - \beta_{Time} \cdot \frac{F(e)^{n-1}}{\rho^{n-1}}\right] \tag{4.89}$$

Turbulent viscosity.

$$\widetilde{\nu}^{n+1} = \frac{2 \cdot \beta_{Time} \cdot \widetilde{\nu}^n - (\beta_{Time} - 0.50) \cdot \widetilde{\nu}^{n-1}}{\beta_{Time} + 0.50} + \Delta t \cdot \left[(1 + \beta_{Time}) \cdot \frac{F(\widetilde{\nu})^n}{\rho^n} - \beta_{Time} \cdot \frac{F(\widetilde{\nu})^{n-1}}{\rho^{n-1}}\right] \tag{4.90}$$

As there can be seen in time integration equations (4.87), (4.88), (4.89) and (4.90), the time step contributions $F(u)$, $F(v)$, etc.. are divided by the density.

This is because of the variable on the time change rate on the left side of the equation. In these expressions, the overall contributions are referred to the values $\rho\phi$, and so this must be taken into account when operating.

Finally, the other modification on the time integration method for the turbulent regime consists on a little addition to the already shown Courant-Friedrichs-Lewy condition (CFL, section 3.2.3).

As it is explained there, the Δt of each simulation step isn't arbitrary, it is computed following a certain criteria.

This is related with the diffusion of velocity, temperature and the convection (advection) of velocity. And it is, this last term, the CFL convection criteria which is slightly changed because of compressible flow.

While studying incompressible flow, the mathematical equations make perturbations in the field to transport themselves at infinite speed. To give a better insight of this imagine a that at a certain time step a great perturbation takes place at the middle of the flow. Then, right at the next step, this perturbation effects will be noticed by every control volume of the geometry (its effects may vary with the distance).

However, one thing that makes compressible flow much harder to simulate is the fact that, a perturbation on the flow moves through this one at sound speed.

Among other aspects, the increasing difficulty in the compressible flow simulations comes due to the following fact. If the simulation diverges at a certain control volume at present time step, it won't be until many time steps in the future that it will be possible to notice that the simulation has gone wrong. Unfortunately, this makes necessary to repeat the simulation again having wasted many computational time worthless.

Turning back to the CFL condition modification, this consists on adding the sound speed to the spread out velocity in the convection term.

$$\Delta t_c = min\left(0.35\frac{\Delta x}{|u+c|}\ ,\ 0.35\frac{\Delta y}{|v+c|}\right) \tag{4.91}$$

In order to compute the value of the speed of sound, the following expression is used.

$$c = \sqrt{\gamma \cdot R \cdot T} \tag{4.92}$$

4.5.5 Simulation algorithm.

Unlike in the laminar regime section, in this case there is no Poisson's equation that needs an special solver. Instead of that, in order to compute the physical fluid properties of the next step o the simulation, it is only necessary to apply the time integration process described in the previous section (section 4.5.4).

However, in the turbulent compressible regime it is necessary to solve the Spalart-Allmaras turbulence model and the Mass Conservation equations additionally. Therefore, there are some changes in the simulation algorithm from the one presented in section 3.2.6.

The complete turbulent regime smiluation algorithm is presented in figure 4.11. Nevertheless, only the non already explained steps are exposed after it.

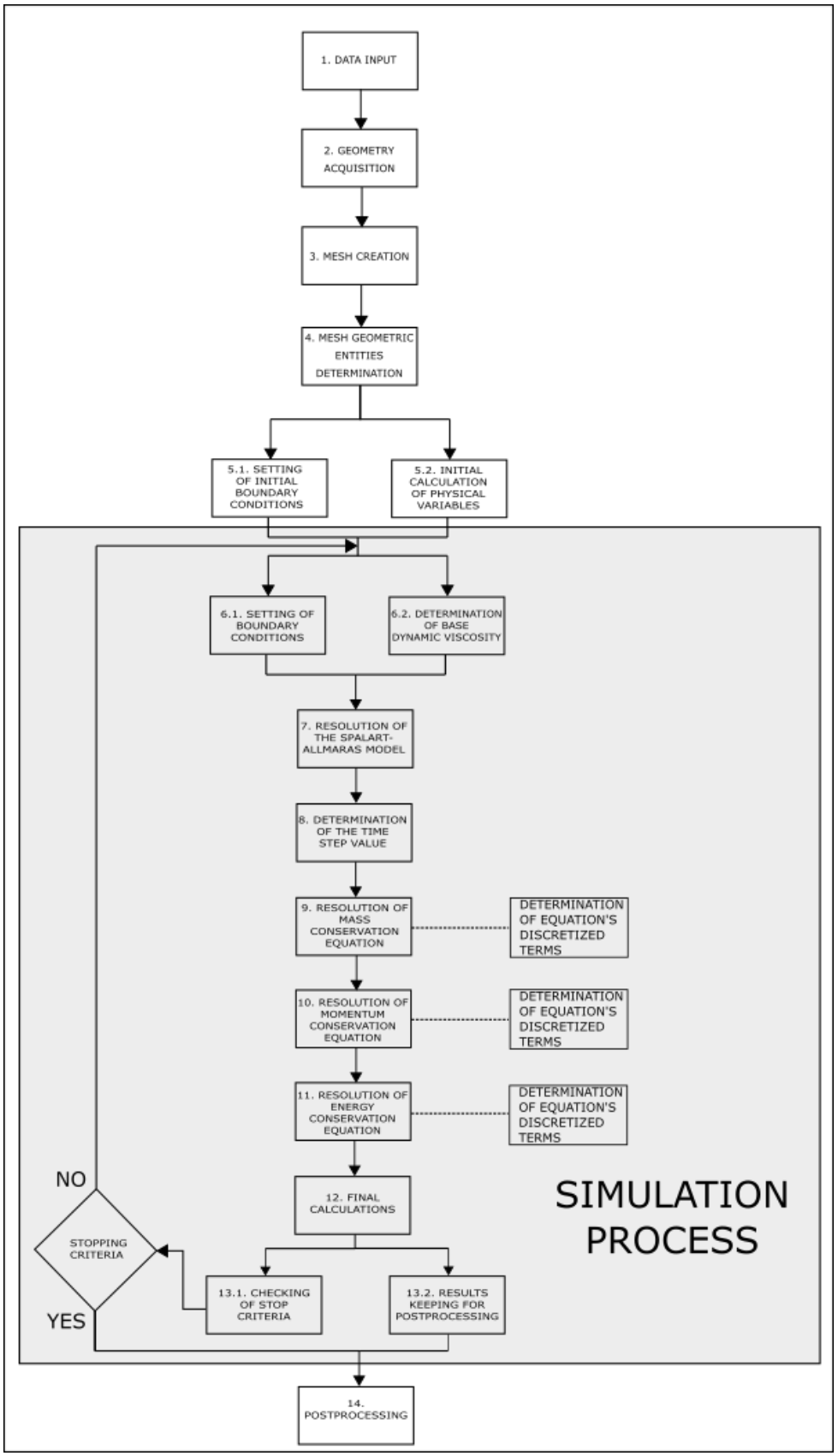

Figure 4.11: Turbulent regime simulation algorithm

- **2. Geometry acquisition.**

  As it has already been explained, one of the aims of the code is to be as generic as possible. It is capable of meshing and simulating many different axisymmetric geometries. But first, it is necessary to obtained the mathematical equation of these.

- **5.2 Initial calculation of physical variables.**

  At the beginning of each simulation, it is necessary to compute some physical data like heat capacities, or certain boundary conditions, etc..

- **6.2 Determination of base dynamic viscosity.**

  At the beginning of each time step, it is important to compute the base dynamic viscosity (due to problem's boundary conditions), needed to solve the turbulence model.

- **7. Resolution of the Spalart-Allmaras model.**

  In order to solve the Navier-Stokes equations, kinematic turbulent viscosity from Spalart-Allmaras model must be determined.

- **9. Resolution of Mass Conservation Equation.**

  It it the first of the 3 Navier-Stokes equations that need to be solved. In order to do that, it is necessary to compute each of its discretized terms (section 4.5.2).

- **10. Resolution of Momentum Conservation Equation.**

  Again, it is one of the Navier-Stokes discretized equations that need to be solved. To do that, all its discretized terms must be determined first (section 4.5.2).

- **11. Resolution of Energy Conservation Equation.**

  Last of the Navier-Stokes equations that is necessary to solve. Again, it is necessary first to calculate its discretized terms (section 4.5.2).

4.6 Simulation of turbulent compressible pipe flow.

In this section are presented the obtained results in the simulations of the turbulent supersonic compressible pipe. As there has already been done in the laminar regime results sections, there will also be presented the verification and an extensive explanation of the physical phenomena involved in the problem.

The turbulent supersonic pipe case has already been briefly presented previously, in section 4.4. As its name already indicates, it consists on a constant radius pipe in which there is a supersonic flow at its inlet.

The trustworthy scientific publication used in the comparisons can be found in [38]. In order to be able to compare the obtained results with the source mentioned, there has been necessary to add some features to the case. These are exposed next up.

First of them, and probably, the most significant one is the Reynolds number selection. In case of the laminar regime LID Driven Cavity and Square Cylinder, this parameter is calculated or set depending on several variables but not temperature. In turbulent compressible flows, temperature plays a huge role, and it is impossible to define the flow conditions without it.

In the problem case, the solid wall of the pipe is set to have a constant temperature (T_{Wall}) in all of its length. This define the speed of sound in all of the geometry.

$$c = \sqrt{\gamma \cdot R \cdot T_{Wall}} \tag{4.93}$$

The other two parameters that define the sonic speed γ and R are set to simulate air.

$$\gamma = 1.40 \qquad\qquad R = 286.90 \ J/Kg \cdot K \tag{4.94}$$

Since these have been set as the air characteristics values, so must the Prandtl number of the simulation. As in the LID Differentially Heated problem, in this case it is set to 0.71.

Reynolds number is defined by fluid's viscosity too. As there has been exposed in section 4.1.1, in the turbulent regime study the viscosity has been set to be temperature dependant.

The mathematical expression selected from the Sutherland law is the following.

$$\frac{\mu(T)}{\mu_{Ref}} = \left(\frac{T}{T_{Ref}}\right)^n \tag{4.95}$$

For the problem, there has been set the reference values of the equation (4.95) for an ambient temperature of 25ºC. The data for the reference dynamic viscosity at that temperature can be found in [39]. In addition to that, the reference sets the value of the n as 0.7, and so it is done in the project.

In what comes to the reference length of the problem, this has been set as the pipe radius.

Once these parameters have been defined, it is possible to calculate or set the Reynolds number. However, in this case there will be used what's known as *bulk Reynolds*. This is a Reynolds

number based on the averaging of the flow variables. It doesn't have any relation with the averaging processes shown in previous sections for RANS turbulence modelling. It is also used in DNS simulations.

This bulk Reynolds have the following expression.

$$Re_m = \frac{\overline{\rho_m} \cdot \overline{u_m} \cdot L_{Ref}}{\mu_w} \tag{4.96}$$

It is presented the definition of the Mach number for the problem too.

$$M_m = \frac{\overline{u_m}}{\sqrt{\gamma R T_{Wall}}} \tag{4.97}$$

Once the previously mentioned variables have been calculated, it is possible to define the flow characteristics at the inlet by using the equations (4.96) and (4.97).

By setting the mean Mach number at the entrance M_m, it is possible to compute the mean velocity $\overline{u_m}$ there. Then, it is possible to compute the dynamic viscosity at the wall by applying the mathematical formula presented before (4.95).

Finally, defining a bulk Reynolds number, the value of the density at the inlet can be imposed.

All the flow variables at the inlet have been completely defined.

4.6.1 Obtained results and verification

First of all, as in the laminar regime study cases, it is presented the simulation parameters in table 4.2.

Table 4.2: Turbulent compressible supersonic pipe simulation parameters

Simulation	**DNS**	**RANS**
L_{Ref} (m)	1.0	1.0
Pipe Length (m)	25.0	25.0
T_{Wall} (K)	298.15	298.15
Re_m	3181.0	3181.0
M_m	1.30	1.30
X Direction Nodes	250	120
R Direction Nodes	120	90
X Nodal Distribution	Regular	Regular
R Nodal Distribution	Hyp. Tan	Regular
Hyp. Tan. Stretching	1.0	-
Stop Criteria	-	1,00E-06

As it is shown in previous table, there have been made 2 different simulations. One solving the already explained RANS Spalart-Allmaras turbulence model, and the other one by just carrying

out a DNS simulation. This allows to compare the results obtained in both of them and see the advantages and disadvantages of each type of approach.

Verification.

The verification of the turbulent regime study case simulation is based on the comparison of several parameters and flow profiles with the ones present in [38]. In the publication, the authors carry out a DNS simulation of a turbulent compressible supersonic pipe with a tri-dimensional approach.

The parameters of the comparison are the friction Reynolds and Mach numbers.

As the reader may sense from the names, these are related to the friction of the pipe flow with its solid wall.

The viscosity of the fluid alongside with the non-slip condition at the solid wall leads to a non-null friction in this area.

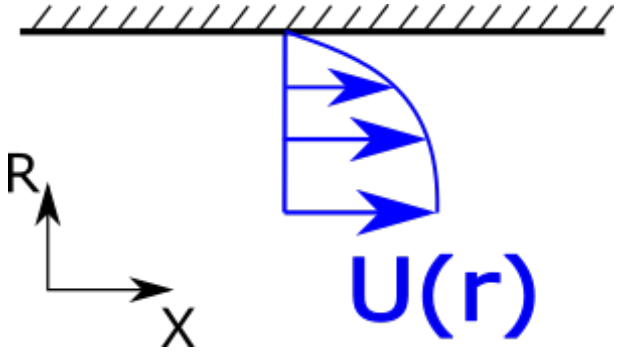

Figure 4.12: Flow profile at the wall scheme

Calculating the velocity gradient right at the wall gives the wall shear stress, which is the base of the two verification parameters previously mentioned, friction Reynolds and Mach numbers.

$$\tau_W = \mu \cdot \frac{\partial u}{\partial r} \tag{4.98}$$

Since all the data is discrete, there are several tiny modifications to make to equation (4.98).

The way to compute the velocity gradient is to take the difference between the wall node and the closest to it. This leads to a linear gradient. In order to avoid this simlification and obtained more accurate results, it is possible to develop a wall shear model. However, this is way beyond the project scope for this section.

Nevertheless, the nodal resolution at the wall is set to be enough accurate to get an acceptable results of this calculation.

In order to being able to describe with the parameters the flow at the pipe, no discrete individual data can be taken. The mean value must be computed $\overline{\tau_W}$. To obtain this, an spatial integration of the discrete values must be done.

Then, another variable should be computed based on the previous one, the friction velocity u_τ.

$$u_\tau = \sqrt{\frac{\overline{\tau_W}}{\overline{\rho_W}}} \tag{4.99}$$

In this case, it is also necessary to compute the mean value of the density at the wall by doing again an spatial integration of this variable.

Once the friction velocity has been determined, it is possible to compute the friction Reynolds and Mach numbers (equations (4.100) and (4.101) respectively).

$$Re_\tau = \frac{\overline{\rho_W} \cdot u_\tau \cdot L_{Ref}}{\mu_W} \tag{4.100}$$

$$M_\tau = \frac{u_\tau}{\sqrt{\gamma \cdot R \cdot T_{Wall}}} \tag{4.101}$$

Next up, in table 4.3, are presented the comparison between the obtained results and the ones from the scientific paper of the previous parameters. In addition, it is shown the values of the bulk Reynolds and Mach numbers at the calculation section of the friction parameters.

Table 4.3: Reynolds and Mach numbers obtained comparison

Parameter	Re_τ	M_τ	Re_m	M_m
Source DNS	245.000	0.077	3181.000	1.300
Obtained DNS	237.334	0.087	3182.918	1.359
Ob. DNS Relative Error (%)	3.129	12.987	0.060	4.538
Obtained RANS	238.144	0.088	3180.987	1.358
Ob. RANS Relative Error (%)	2.798	14.286	0.001	4.462

There are several aspects to comment about the results presented in table 4.3.

First, it must be mentioned that, in what comes to the friction Reynolds, the results obtained are a little lower than the one from the scientific paper. However, the relative error in both cases is lower than a 5%, which shows that they can be considered as correct.

On the other hand, the friction Mach numbers have a higher relative error than Reynolds ones. As it has been mentioned, there is a strong dependence of this value from the way to compute the velocity gradient at the wall and the resolution of the mesh close to it. Nevertheless, none of them has a relative error higher than 15% approximately. They are close to it, but the results can still be considered as acceptable from an engineering point of view.

In addition, there must be mentioned that the results from the source and the codes developed are likely to differ in a certain way. In the scientific publication, the authors use many different and more complex numerical techniques and methods, which, although are aimed to solve the same equations, the final results may differ from one project to another.

Finally, it is presented the bulk Reynolds and Mach numbers comparison. As it has been said, the inlet conditions are controlled by this same parameters. However, it is always important to verify if the imposed conditions are still present where the additional data is been computed.

In other words, the friction parameters depend strongly in the bulk ones. Therefore, it is crucial to verify that where the first ones are been calculated, there are still the flow conditions initially imposed.

The other variables used for the verification of the turbulent regime case are the temperatures and density radial non-dimensionalized profiles of the flow. These are presented in figures 4.13 and 4.14 respectively.

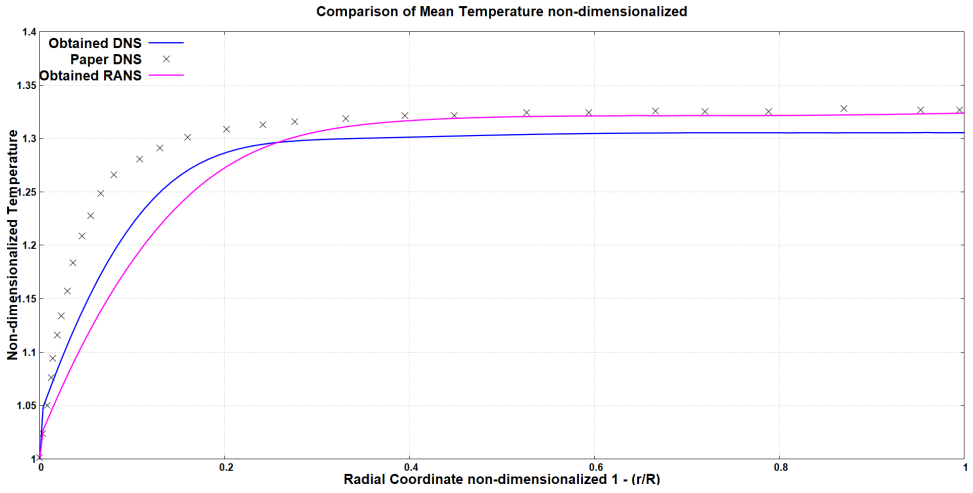

Figure 4.13: Temperature non-dimensional profiles comparison

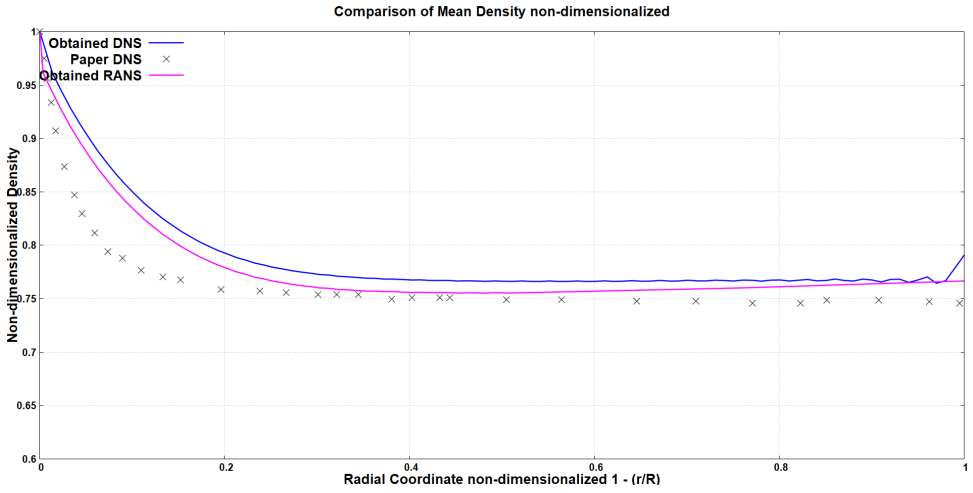

Figure 4.14: Density non-dimensional profiles comparison

In order to be able to compare the temperature and density profiles, the authors present in the publication the non-dimensionalized values. The reference parameters chosen are the wall's temperature (T_{Wall}) and the density at the same location (ρ_W), both previously set or calculated.

$$T^*(r) = \frac{T(r)}{T_{Wall}} \qquad \rho^*(r) = \frac{\rho(r)}{\rho_W} \tag{4.102}$$

As there can be seen in both figures, obtained DNS and RANS temperature and density profiles have very similar results. This has been already seen in table 4.3. The friction parameters results for both of these simulations match almost perfectly.

However, looking at figures 4.13 and 4.14, there can be seen that the obtained results are not exactly the same as the ones from the scientific publication. As it has been previously mentioned, the authors use different numerical techniques and methods that make the results to differ. In addition to the temporal integration of the results, which is completely different and extremely complex in comparison with the one done for the DNS in this project. In case of the RANS model simulation, it is not needed since it already provides the averaged values.

Nevertheless, it may look like a great difference in both cases. However, when analysing it numerically, this difference gets smaller in comparison. The average relative error is less than 5%. But, in addition to that, it is only needed to look at the enormous similarity between the profiles tendencies to consider the results obtained as acceptable.

Results

Next up the results obtained for the RANS simulation are presented. As it is specified in the simulation parameters (table 4.2), the total length of the pipe has been set to 25 m. However, since the relevant part of the study is where there is a fully developed flow, only the last half of the pipe is presented.

Temperatures field.

In figure 4.15 is presented the temperatures field obtained in the simulation.

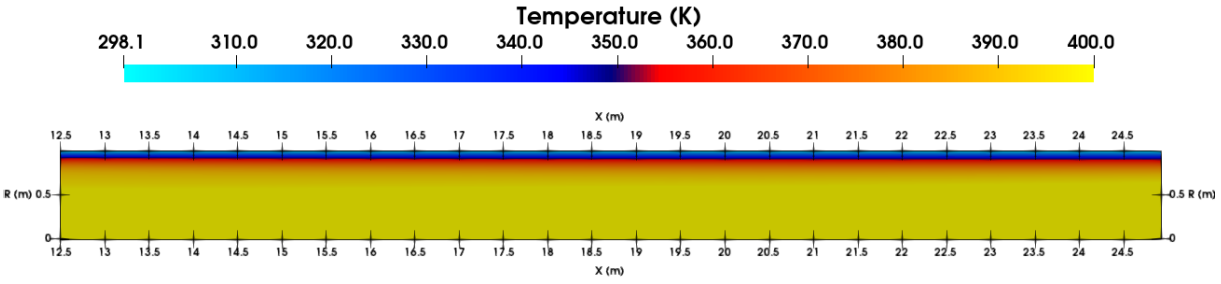

Figure 4.15: Turbulent supersonic compressible pipe temperatures field

As there can be seen in figure 4.15, most of the pipe flow temperature profile is close to 390 to 400 K. This can be also found in figure 4.13. The wall's temperature has been set to 298.15 K (25ºC). Therefore, a 1.30 non-dimensional value of this lead to the present temperatures field.

In addition to that, it is important to mention the huge temperature gradient that takes place near the wall. In figure 4.13 this can be seen by the quickly increase in the plot value. But, the best way to see it is looking at figure 4.15, where there can be seen an enormous change from 298.15 K to almost 400 K in less than 20 cm.

Velocities field.

In figure 4.16 is presented the non-dimensional velocities field obtained for the simulation of the turbulent supersonic compressible pipe.

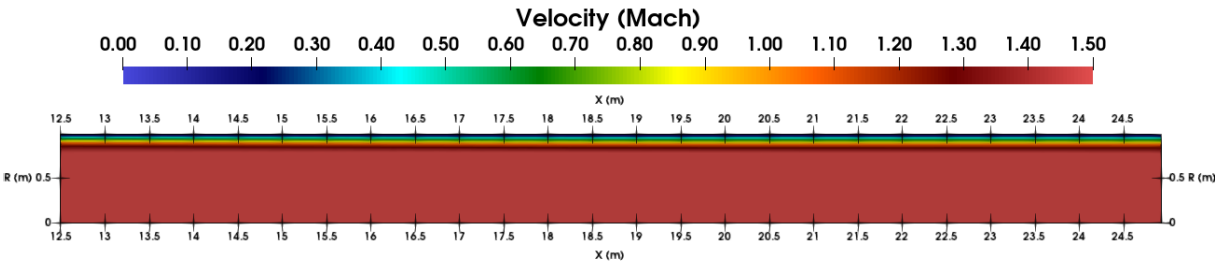

Figure 4.16: Turbulent supersonic compressible pipe Velocity Magnitude field

There are several aspects to mention about the non-dimensionalized velocities field in figure 4.16.

First of them concerns concerns the choice of present the velocity results as a function of Mach number. While studying or simulating supersonic flow, the velocities reached by the flow are usually too high to work and use them to compare.

Instead of that, it is much more practical and useful to show these results with the Mach number. When presenting the capabilities of a supersonic aircraft, Mach number is used to mention its velocity, not m/s or Km/h.

The other important aspect that must be remarked is the cross-sectional velocity profile. As it has been mentioned before, non-slip condition is imposed at the pipe wall. Therefore, a velocity gradient is generated due to this restriction. However, in this case, the resulting gradient is extremely larger than any shown in the laminar regime section.

To give the reader an idea about its magnitude, in this case are presented the velocity profile and the non-dimensionalized velocity profile of the cross-section of the pipe in figures 4.17 and 4.18 respectively.

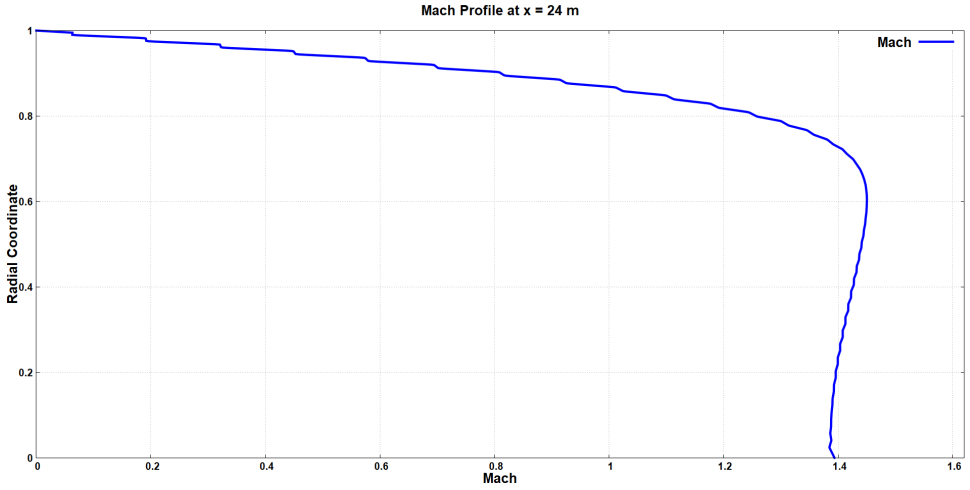

Figure 4.17: Turbulent supersonic compressible pipe non-dimensional Horizontal Velocity profile at x = 24 m

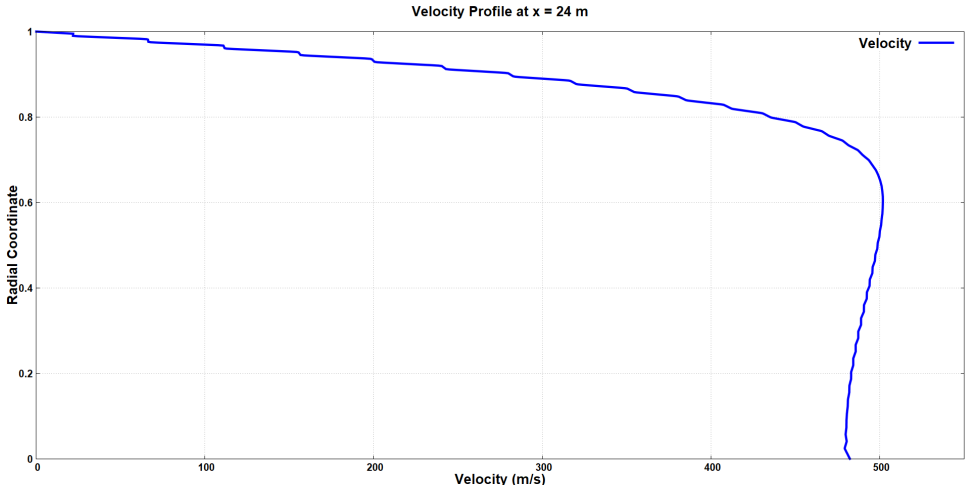

Figure 4.18: Turbulent supersonic compressible pipe Horizontal Velocity profile at x = 24 m

As there can be seen in both figures, the velocity gradient at the wall is much higher than anyone shown in the project before. It reaches 100 m/s in just less than 5 cm from the wall approximately. This is one of the main difficulties when calculating variables at the wall like the ones presented before, friction Reynolds and Mach numbers. The gradients are so high that a great resolution is needed. Otherwise, nonsense results could be obtained.

In addition to that, there must be mentioned the huge velocities present at the pipe. For instant, the highest one of figure 4.17 is larger than 500 m/s, which is more than 1800 Km/h, twice the cruise speed of a commercial aircraft.

Pressure field.

In figure 4.19 is presented the pressure field for the simulation of the turbulent supersonic compressible pipe.

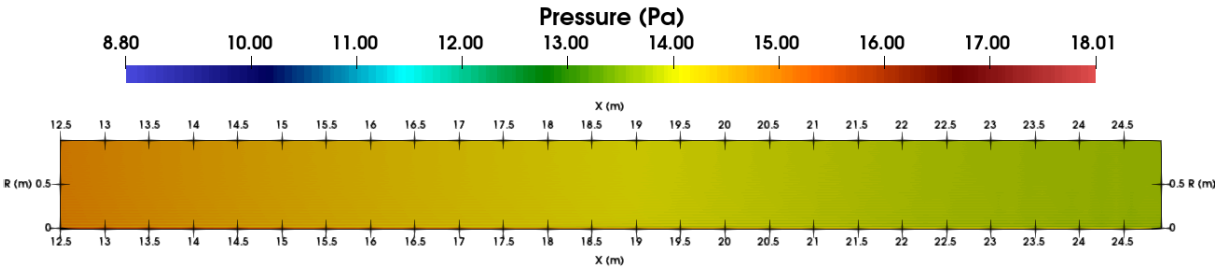

Figure 4.19: Turbulent supersonic compressible pipe pressure field

As there can be seen in figure 4.19, there is a tiny pressure drop in the axial direction. However, the flow velocities (shown previously) are so high that this pressure gradient can be considered as negligible.

In addition to that, looking at image 4.19, there can be observed the almost null change in pressure in the radial direction. This is mainly because the radial velocity is close to zero, and so its gradients.

Density field.

In figure 4.20 is presented density field obtained in the simulation.

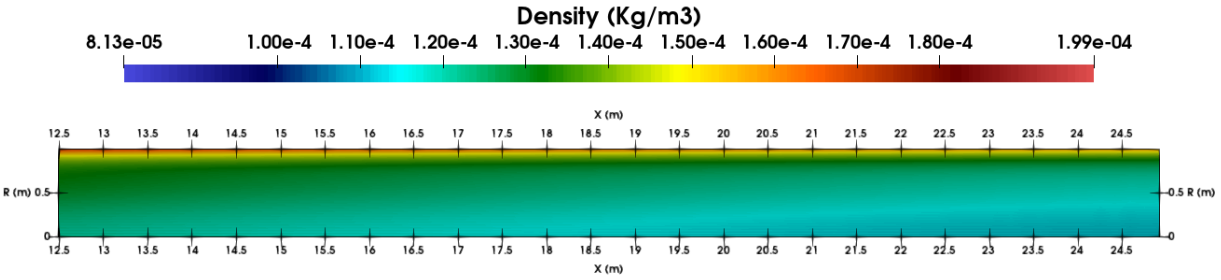

Figure 4.20: Turbulent supersonic compressible pipe density field

Looking at figure 4.20 there can be seen the same radial density profile as the one shown previously in the verification. The fluid's density close to the wall is much higher than near the central axis. This happens because of the flow velocities.

Near the wall, flow's speed is much lower than at the centre due to non-slip condition at the wall. And so the density increases in this area.

Chapter 5

Environmental impact of the project

Once every project is almost finished, it is essential to look back and carry out an environmental study of it. Not only to see if it has been a success in this aspect, but to know if it is possible to improve the results in this area.

Because of that, next up is presented an exhaustive study of the environmental impact of the present project. This will be divided into the work tasks exposed in the budget section.

5.1 Documentation and investigation.

Most of the information and learning of the theoretical basis of the project have come from trustworthy Internet sources and scientific publications. The environmental impact of this part of the project has been smaller in comparison with other tasks.

First, in what comes to energy use during this part, it must be mentioned that most of the time natural light was used, instead of artificial. Additionally, in order to save energy, the computers used have been off when these weren't needed.

However, one aspect that clearly can be improved is the paper sheets usage. Due to the enormous amount of information that should be gathered to fulfil project's requirement, there has been necessary to buy a pack of these. Unfortunately, these weren't recycled sheets.

So, the main aspect that should be improved for next projects in this tasks is the usage of least possible paper sheets and if possible recycled ones.

5.2 Coding and debugging.

This section of the project is probably the one with the highest environmental impact. For this part, it is necessary at least to use one computer at a time, if not the two available.

Coding takes a lot of time. This kind of Computational Fluid Dynamics projects needs an enormous programming effort. The student has to develop every feature of the code. For instance, all of the present project combined have more than 7 thousand lines of coding.

This is a huge computer power consumption which is quite difficulty to reduce. A lot of programming experience is necessary. And even with it, there will be needed to add the debugging time to the energy usage.

However, there has been tried to minimise this consumption by using only one computer at a time when it was possible. Unfortunately, there were many situations in which this was really difficult.

5.3 Verification of the results.

This section is probably the one with the smallest environmental impact of the whole project. The flow simulations have been carried out as part of this task. These obviously represent the highest energy usage per hour of all tasks. The computer were at maximum power. However, these didn't take as much time as others. The reduction in total hours is quite significant in comparison with any of the rest.

In addition to that, it must be mentioned that one of the aims of every computational code developed is to be as efficient as possible. This, obviously, improve with the coding experience.

5.4 Project's memory development.

Since the project's memory has been written using an online text service, the only environmental impact of this task comprises the power consumption of the computer and the artificial light used.

First, it must be mentioned again that, when it was possible, only one computer was used at a time, in order to save energy. In addition to that, artificial light consumption was reduced as much as possible.

Finally, to be able to cut down even more the impact, there has been decided not to print the memory thesis or any of its attached documents.

In conclusion, there has been obviously several points in which the environmental impact could be severely reduced. However, this project has taken a lot of time and power resources, which are likely to be cut down in future developments with better equipment and much more experience.

Chapter 6

Conclusions and future work.

Next up are presented the conclusions extracted from the development of the present project, its implications and the future work.

6.1 General conclusions.

The main conclusion that can be extracted from an overall view of the whole project is the complete fulfilment of its scope. The aim was to study the computational resolution of the Navier-Stokes conservation equations and the application to different cases.

First of all, it is important to mention the difficulty and all the hard work needed for the development of this kind of studies. It is not only needed to coding and carry out the simulations. It is necessary to find the information about the physical phenomena involved, learn algorithms and programming techniques, coding and debugging, which takes a lot of time, and validating the results using trustworthy scientific sources.

In what comes to the development of the laminar regime scopes of the project there are several conclusions that can be extracted.

First of them comprises the learning of the physical phenomena and the flow characteristics. In addition to that, there must be noticed the success in the computational implementation of the resolution algorithms. As it has been shown, these add an extra difficulty to the project, since it is necessary to develop all of them.

There were many simulation difficulties. It was necessary much code debugging time.

However, that extra time added to the project development has been completely worthy. The results obtained for the laminar regime study cases, LID Driven Cavity, LID Differentially Heated and Square Cylinder are more than acceptable. As there has been shown, all of these match greatly with the referencesç authors selected for the comparison.

Nevertheless, there is one aspect in the laminar regime part of the project that can be clearly improved, the code efficiency. These codes were the first ones to be programmed by the student in the CFD area. Therefore, these can be improved severely in the aspect of efficiency.

Additionally, there are many different conclusions to extract from the turbulent regime section of the project.

First of them is the enormous increase in difficulty in comparison with the laminar regime. Not only because turbulent flow has a much more complicated theoretical basis behind, but also due to the simulation of compressible fluid.

As there has been shown, it is needed to modify the Navier-Stokes equations to avoid getting instabilities in the simulations. In addition to that, in order to be able to simulate the proposed case, there has been needed the implementation of the Spalart-Allmaras turbulence model.

This added even extra difficulties due to the following reasons.

First of them, it was necessary to learn and understand all the theoretical basis of RANS turbulence models and the equations averaging.

In addition to that, the numerical implementation of the Spalart-Allmaras model made compulsory to learn again, the theoretical basis behind, which wasn't easy at all.

But, furthermore, the addition of the compressible flow hypothesis to the simulations made the implementation even more complicated. Originally, the model was developed for incompressible fluids, as it can be seen in the authors paper from 1994 [30]. Therefore, it is difficult even today to find trustworthy information about the compressible form of the model. There are several differences in the equations from one application case to another.

However, in spite of all the difficulties previously mentioned, the obtained results for this section of the project can be considered as acceptable. It is true that there are some parameters such as the friction Mach number which have almost a relative error of 15%. Nevertheless, there must be taken into account the great difficulty in its calculation due to the flow conditions simulated (supersonic velocities) and the nodal resolution near the wall.

Therefore, for the present project, these results can be considered as highly acceptable. However, they can be improved with more experience in turbulence modelling and CFD simulation.

It is because of all aforementioned that in what comes to the fulfilment of the project scopes, these can be considered as a clear success. Not only there has been developed several complex studies for each of the flow regimes in CFD. But also, the results obtained can be considered a success too.

6.2 Future work.

This project has provided a great background in Computational Fluid Dynamics. All the different theoretical basis learnt, the algorithms implemented and the kind of studies developed give the student amazing possibilities for further work.

Therefore, it would be a waste of learning time and possibilities to stop at this point. Next up are presented the future lines of research for the project.

6.2.1 Short term.

Due to the situation brought by the Covid-19 outbreak, the turbulent regime part of the project has been severely reduced. Therefore, the first tasks to be developed aim completely to this part of the project. Initially, there were several study cases related to rocket nozzle. However, there hasn't been possible to complete them all.

Therefore, the first line of research is to be able to simulate these cases and if possible, to add more geometry simulation features to the codes.

6.2.2 Mid term.

For the mid-term lines of research, the aim is to implement others RANS turbulence models such as $k-\omega$ or $k-\varepsilon$ and compare them with the Spalart-Allmaras. This would give a more global vision of the RANS turbulence modelling and allow to compare the results obtained with each of them, in order to select which are better for each application.

As there can be seen, the future work is completely related to the computational resolution of turbulent regime flows and its application to the simulation of rocket nozzles mainly.

The global aim is to create a "tool" to simulate, analyse and improve the performance of the geometries of rocket nozzles. It is a huge and far aim for just a graduate student. However, the background acquired with this project is a great way to begin the path with.

Bibliography

[1] Josip Basic. Turbulent history of fluid mechanics (brief essay). (January), 2016. doi: 10.13140/RG.2.1.3487.8485.

[2] Bachelor/Master Thesis in Computational Fluid Dynamics (CFD), . URL https://www.termoflow.com/jobs/detail/bachelor-master-thesis-in-computational-fluid-dynamics-cfd-1. Retrieved 25-3-2020.

[3] Computational Fluid Dynamics Software Saves Time, Cuts Costs — 2018-03-07 — Assembly Magazine, . URL https://www.assemblymag.com/articles/94178-computational-fluid-dynamics-software-saves-time-cuts-costs. Retrieved 25-3-2020.

[4] Computational Fluid Dynamics Optimisation Based On Formula 1 Methods – Swiss Side, . URL https://www.swissside.com/blogs/news/computational-fluid-dynamics-optimisation-based-on-formula-1-methods. Retrieved 25-3-2020.

[5] NASA@SC11 Demo: Space Shuttle Aerodynamics and Debris Simulations, . URL https://www.nas.nasa.gov/SC11/demos/demo20.html. Retrieved 25-3-2020.

[6] Shahil S Charania, Vishal Soni, Kiran C Patel, Jaymin Desai, and Vishal Chauhan. Evaluation of Vertical Kaplan Turbine using CFD. *Proceedings of the Thirty Ninth National Conference on Fluid Mechanics and Fluid Power*, (December):1–10, 2012. doi: 10.13140/2.1.3455.3926.

[7] Characteristics of Laminar Flow & Turbulent Flow — ibidi. URL https://ibidi.com/content/286-the-different-types-of-flow#laminar. Retrieved 26-3-2020.

[8] Niels N. Sørensen, B. Méndez, A. Muñoz, G. Sieros, E. Jost, T. Lutz, G. Papadakis, S. Voutsinas, G. N. Barakos, S. Colonia, D. Baldacchino, C. Baptista, and C. Ferreira. CFD code comparison for 2D airfoil flows. *Journal of Physics: Conference Series*, 753 (8), 2016. ISSN 17426596. doi: 10.1088/1742-6596/753/8/082019.

[9] Hammond Steven; Schreiber Robert. Mapping Unstructured Grid Problems to the Connection Machine. *Research Institute for Advanced Computer Science NASA Ames Research Center*, 1990. doi: 10.1006/rwos.2001.0118.

[10] S. Arias and A. Montlaur. Numerical study and experimental comparison of two-phase flow generation in a T-junction. *AIAA Journal*, 55(5):1565–1574, 2017. ISSN 00011452. doi: 10.2514/1.J055387.

[11] A.D. Elster. Laminar v turbulent - Questions and Answers in MRI, 2018. URL http://mriquestions.com/laminar-v-turbulent.html. Retrieved 5-19-2020.

[12] Spalart-Allmaras model – CFD-Wiki, the free CFD reference, . URL https://www.cfd-online.com/Wiki/Spalart-Allmaras_model. Retrieved 27-4-2020.

[13] Lecture Notes, Fluid Dynamics, and Chiang C Mei. Methods of Describing Fluid Motion. pages 1–3, 2003.

[14] Charles Hirsch. The Basic Equations of Fluid Dynamics. *Numerical Computation of Internal and External Flows*, (3):27–64, 2007. doi: 10.1016/b978-075066594-0/50041-2.

[15] Robin Kravets and Cigdem Sengul. Energy conservation. *Ad Hoc Networks: Technologies and Protocols*, pages 153–195, 2005. doi: 10.1007/0-387-22690-7{_}6.

[16] Cüneyt Sert. Governing Equations of Fluid Flow and Heat Transfer. *ME 582 Finite Element Analysis in Thermofluids*, pages 1–13, 2012.

[17] Richard D. Noble. Natural Convection. *AIChEMI Modular Instruction, Series C: Transport*, 4:20–28, 1983. doi: 10.1017/cbo9780511841606.009.

[18] Forced convection - Energy Education. URL https://energyeducation.ca/encyclopedia/Forced_convection. Retrieved 22-3-2020.

[19] Laminar Flow Fluid Flow Review - Engineers Edge. URL https://www.engineersedge.com/fluid_flow/laminar_flow.htm. Retrieved 26-3-2020.

[20] Boussinesq Approximation Definition, . URL https://www.comsol.com/multiphysics/boussinesq-approximation. Retrieved 26-3-2020.

[21] Boussinesq approximation (buoyancy) - Wikipedia, . URL https://en.wikipedia.org/wiki/Boussinesq_approximation_(buoyancy). Retrieved 26-3-2020.

[22] CTTC - Universitat Politècnica de Catalunya. Fractional Step Method Staggered Meshes. 2014.

[23] CTTC. Introduction to the Fractional Step Method. pages 1–10.

[24] F. X. Trias and O. Lehmkuhl. A self-adaptive strategy for the time integration of navier-stokes equations. *Numerical Heat Transfer, Part B: Fundamentals*, 60(2):116–134, 8 2011. ISSN 10407790. doi: 10.1080/10407790.2011.594398. URL https://upcommons.upc.edu/handle/2117/13309.

[25] U. Ghia, K. N. Ghia, and C. T. Shin. High-Re solutions for incompressible flow using the Navier-Stokes equations and a multigrid method. *Journal of Computational Physics*, 48 (3):387–411, 1982. ISSN 10902716. doi: 10.1016/0021-9991(82)90058-4.

[26] N. C. Markatos and K. A. Pericleous. Laminar and turbulent natural convection in an enclosed cavity. *International Journal of Heat and Mass Transfer*, 27(5):755–772, 1984. ISSN 00179310. doi: 10.1016/0017-9310(84)90145-5.

[27] G. De Vahl Davis. Natural convection of air in a square cavity: A bench mark numerical solution. *International Journal for Numerical Methods in Fluids*, 3(3):249–264, 1983. ISSN 10970363. doi: 10.1002/fld.1650030305.

[28] M. Breuer, J. Bernsdorf, T. Zeiser, and F. Durst. Accurate computations of the laminar flow past a square cylinder based on two different methods: Lattice-Boltzmann and finite-volume. *International Journal of Heat and Fluid Flow*, 21(2):186–196, 2000. ISSN 0142727X. doi: 10.1016/S0142-727X(99)00081-8.

[29] Favre averaged Navier-Stokes equations – CFD-Wiki, the free CFD reference. URL `https://www.cfd-online.com/Wiki/Favre_averaged_Navier-Stokes_equations`. Retrieved 10-5-2020.

[30] P. R. Spalart and S. R. Allmaras. One-equation turbulence model for aerodynamic flows. *Recherche aerospatiale*, (1):5–21, 1994. ISSN 00341223. doi: 10.2514/6.1992-439.

[31] Juan Bautista and Pedro Costa. On the Numerical Compressible Flows.

[32] [CFD] The Spalart-Allmaras Turbulence Model - YouTube, . URL `https://www.youtube.com/watch?v=XivcOEIGFQw`. Retrieved 12-5-2020.

[33] Munshoor Ahmed, M. Rehan Saleem, Saqib Zia, and Shamsul Qamar. Central upwind scheme for a compressible two-phase flow model. *PLoS ONE*, 10(6):e0126273, 6 2015. ISSN 19326203. doi: 10.1371/journal.pone.0126273. URL `https://journals.plos.org/plosone/article?id=10.1371/journal.pone.0126273`.

[34] W. Rozema, J. C. Kok, R. W.C.P. Verstappen, and A. E.P. Veldman. A symmetry-preserving discretisation and regularisation model for compressible flow with application to turbulent channel flow. *Journal of Turbulence*, 15(6):386–410, 2014. ISSN 14685248. doi: 10.1080/14685248.2014.910604.

[35] Basic Mathematical Relations. The Conservation Equations of Fluid Dynamics. *Fluid Dynamics*, 0(4):1–9, 2011.

[36] Del in cylindrical and spherical coordinates - Wikipedia. URL `https://en.wikipedia.org/wiki/Del_in_cylindrical_and_spherical_coordinates#Cylindrical_derivation`. Retrieved 4-5-2020.

[37] F. X. Trias, M. Soria, A. Oliva, and C. D. Pérez-segarra. Direct numerical simulations of two- and three-dimensional turbulent natural convection flows in a differentially heated cavity of aspect ratio 4. *Journal of Fluid Mechanics*, 586:259–293, 2007. ISSN 00221120. doi: 10.1017/S0022112007006908.

[38] Somnath Ghosh, Holger Foysi, and Rainer Friedrich. Compressible turbulent channel and pipe flow: Similarities and differences. *Journal of Fluid Mechanics*, 648:155–181, 2010. ISSN 00221120. doi: 10.1017/S0022112009993004.

[39] Air - Dynamic and Kinematic Viscosity. URL `https://www.engineeringtoolbox.com/air-absolute-kinematic-viscosity-d_601.html`. Retrieved 14-5-2020.